

Copyright © 1993, by the author(s).  
All rights reserved.

Permission to make digital or hard copies of all or part of this work for personal or classroom use is granted without fee provided that copies are not made or distributed for profit or commercial advantage and that copies bear this notice and the full citation on the first page. To copy otherwise, to republish, to post on servers or to redistribute to lists, requires prior specific permission.

**DESIGN OF HIGH DENSITY PLASMA SOURCES  
FOR MATERIALS PROCESSING**

by

Michael A. Lieberman and Richard A. Gottscho

Memorandum No. UCB/ERL M93/3

11 January 1993

**DESIGN OF HIGH DENSITY PLASMA SOURCES  
FOR MATERIALS PROCESSING**

by

Michael A. Lieberman and Richard A. Gottscho

Memorandum No. UCB/ERL M93/3

11 January 1993

**ELECTRONICS RESEARCH LABORATORY**

College of Engineering  
University of California, Berkeley  
94720

TITLE PAGE

**DESIGN OF HIGH DENSITY PLASMA SOURCES  
FOR MATERIALS PROCESSING**

by

Michael A. Lieberman and Richard A. Gottscho

Memorandum No. UCB/ERL M93/3

11 January 1993

**ELECTRONICS RESEARCH LABORATORY**

College of Engineering  
University of California, Berkeley  
94720

## **DESIGN OF HIGH DENSITY PLASMA SOURCES FOR MATERIALS PROCESSING**

**Michael A. Lieberman  
Department of Electrical Engineering and Computer Sciences  
University of California  
Berkeley, CA 94720**

**and**

**Richard A. Gottscho  
AT&T Bell Laboratories  
Murray Hill, NJ 07974**

### **ABSTRACT**

**In this review article, we focus on recent advances in plasma source technology for materials processing applications. The motivation behind new source development is discussed along with the limitations of conventional radio frequency diode systems. Then the fundamental principles underlying electron heating in electron cyclotron resonance, helicon wave, inductively coupled, helical resonator, and surface wave plasmas are discussed with some attention to design issues. The transport of ions to device wafers and its influence on etching anisotropy is discussed for all sources. Similarly, we examine the benefits of using high density sources for minimizing plasma process induced damage and discuss in particular, the effects of plasma uniformity on charging damage.**

## CONTENTS

I. INTRODUCTION . . . . .	1
I.A Capacitively Coupled Radio Frequency Discharge Sources . . . . .	2
I.B Limitations of Capacitively Coupled Radio Frequency Discharges . . . . .	4
I.C Overview of High Efficiency Sources . . . . .	5
II. PRINCIPLES OF LOW PRESSURE, HIGH EFFICIENCY SOURCE DESIGN . . . . .	6
II.A Unified Analysis of Source Operation . . . . .	8
II.A.1 Electron Temperature 8	
II.A.2 Ion Bombarding Energy 9	
II.A.3 Plasma Density and Ion Current Density 10	
II.B Discharge Heating . . . . .	11
III. ELECTRON CYCLOTRON RESONANCE (ECR) DISCHARGES . . . . .	12
III.A Source Configurations . . . . .	12
III.B Electron Heating . . . . .	14
III.C Resonant Wave Absorption . . . . .	15
IV. HELICON DISCHARGES . . . . .	18
IV.A Helicon Configurations . . . . .	18
IV.B Helicon Modes . . . . .	19
IV.C Antenna Coupling . . . . .	21
IV.D Helicon Mode Absorption . . . . .	21
V. INDUCTIVE DISCHARGES . . . . .	23
V.A Inductive Source Configurations . . . . .	23
V.B Power Absorption and Operating Regimes . . . . .	24
V.C Source Operation and Coupling . . . . .	25
V.D Low Density Operation and Source Efficiency . . . . .	26
VI. HELICAL RESONATOR DISCHARGES . . . . .	27
VII. SURFACE WAVE DISCHARGES . . . . .	30
VIII. PLASMA TRANSPORT . . . . .	32
VIII.A The Ion Energy Distribution Function . . . . .	33
VIII.A.1 Ion Transport and Etching Anisotropy 34	
VIII.B Methods for Measuring Ion Energy Distribution Functions . . . . .	35
VIII.C Methods for Measuring Plasma Potentials . . . . .	36
VIII.D Measurements of Energy Distributions and Potentials . . . . .	37
VIII.D.1 Ion Acceleration Outside the Sheath 37	
VIII.D.2 Transverse Ion Energy 38	
VIII.E Ion Energy Control . . . . .	39
VIII.E.1 Plasma Anodization 42	
IX. Device Damage . . . . .	43
IX.A Atomic Displacement Damage . . . . .	43
IX.B Contamination . . . . .	43
IX.C Charging . . . . .	43
IX.C.1 Plasma Uniformity 44	
IX.C.2 Biasing 44	
IX.D Radiation . . . . .	45
X. SUMMARY AND REMAINING QUESTIONS . . . . .	46
XI. SYMBOL DEFINITIONS . . . . .	48
XII. REFERENCES . . . . .	51

[The following text is extremely faint and illegible, appearing to be a list of figure captions.]

## DESIGN OF HIGH DENSITY PLASMA SOURCES FOR MATERIALS PROCESSING

Michael A. Lieberman  
Department of Electrical Engineering and Computer Sciences  
University of California  
Berkeley, CA 94720

and

Richard A. Gottscho  
AT&T Bell Laboratories  
Murray Hill, NJ 07974

### I. INTRODUCTION

The advent of sub-micron electronic device fabrication has brought unprecedented demands for process optimization and control (1,2) which, in turn, have led to improved plasma reactors for the etching and deposition of thin films. As a result, we have witnessed the introduction of a new generation of plasma systems based on electron cyclotron resonance (ECR) heating (3-6). ECR plasma etching of polycrystalline Si, single crystalline Si, silicides, Al, Mo, W, SiO<sub>2</sub>, polymers, and III-V compound semiconductors have all been reported in recent years (7-33). Similarly, ECR plasmas have been used to deposit amorphous Si, silicon nitride, boron carbide, and SiO<sub>2</sub> to name just a few materials (34-40). Applications of ECR plasmas beyond etching and deposition have also been reported and include ion implantation (41-45), surface cleaning (46-59), surface passivation (60), and oxidation (53,61-63). Besides ECR, many other "novel" plasma generation schemes are now being offered to satisfy manufacturers' needs in these materials processing areas. All these schemes purport to offer advantages over conventional approaches such as the capacitively coupled radio frequency discharge now used in many factories for etching and deposition of thin films during integrated circuit manufacturing.

But which scheme is best? What are the key aspects to plasma source design that impact materials processing? And why are the conventional approaches inadequate? While the answers to these questions remain elusive and are the subject of much current research, one can clearly identify commonalities and differences between the novel sources, whose most distinctive characteristic is higher efficiency than their conventional counterparts operated at low pressure. The purpose of this review is to: (1) develop a unified framework from which all "high efficiency" sources may be viewed and compared; (2) outline key elements of source design that affect processing results; and, (3) highlight areas where additional research and development is needed. In so doing, we hope to assist those who use plasma for materials processing to make wise choices in constructing or purchasing sources, to guide vendors of high efficiency sources in choosing designs that can best meet their customers' expectations, and to inspire the research community to focus on problems of technological interest.

Before beginning such a review, several disclaimers must be made. First, the literature on applications, diagnostics, and modeling of high efficiency sources is now so voluminous that we are not able to review or reference every paper. Rather, we have opted for highlighting key results in line with our objectives stated above. Second, we restrict our focus to those aspects of plasma processing that are uniquely affected by the use of high efficiency plasmas. For example, we discuss aspects of source design that affect plasma-induced electrical damage in microelectronic circuits but a comprehensive discussion of damage mechanisms is the subject of its own review and clearly beyond the scope of this work. Third, there are pertinent areas that while important are not yet ready for review. Foremost amongst these is the field of numerical simulation. While impressive results have been reported recently and we will draw on some of these, little has appeared in print and it is premature to review the field. Similarly, the stability of high efficiency sources is a matter of some concern and recent work illustrates that sudden mode changes and bistability may adversely affect materials properties, but too little has been reported and analyzed to make a thorough discussion meaningful. Finally, any review reflects the biases of the authors and this work is no exception. Based on our interests and experience, we focus on applications of plasmas to microelectronics fabrication and, in particular, etching. Heavy emphasis is placed on simple, analytical, unifying theories and

quantitative diagnostic measurements.

Why new sources? In plasma etching, the shrinking dimensions of micro-electronic devices have placed unprecedented demands on process control. Consider critical dimension (CD) control where the width of the transistor gate is specified to better than 10%. For yesterday's CD of 1  $\mu\text{m}$ , this means a linewidth variation of 0.1  $\mu\text{m}$  can be tolerated but by the end of the 20th century when the CD should be only 0.25  $\mu\text{m}$ , variations in CD must be less than 0.025  $\mu\text{m}$ . This requires unprecedented anisotropy in the plasma etching of gate electrodes, contact windows, and metallic interconnections. To achieve such control, we need to increase the anisotropy of ion transport to the device wafer from what it is in the conventional capacitively coupled rf reactor. This means operating plasmas at lower pressures. But, conventional rf sources are inefficient at low pressure so that high powers must be used to achieve the high rates of ionization and dissociation necessary for high throughput, low-cost manufacturing. Unfortunately, excessive power input to a capacitively coupled system leads to high ion bombarding energies that can degrade selectivity in etching and produce electrical damage that reduces device yield. Thus, new sources are needed to operate at lower pressure and higher efficiency.

In conventional rf systems, ion energy and flux are inexorably linked. But, ion energy control is needed in plasma deposition to tailor film properties such as stress, composition, refractive index, crystallinity, and topography. Ion energy control is used in plasma etching to optimize selectivity and minimize atomic displacement damage while meeting linewidth and throughput specifications. Therefore, gaining superior control of ion energy and decoupling it from ion flux control is further motivation for developing new plasma sources and processing systems.

In the remainder of this section, we review briefly the properties of capacitively coupled radio frequency plasmas and elaborate further on the advantages of high efficiency sources. In the following sections, we first discuss the fundamental principles underlying high efficiency plasma source design and, to compare one source with another, use a simple analysis in Sec. II that allows estimation of electron temperature, ion bombardment energy, and plasma density in terms of the gas phase cross sections, gas density, absorbed power, and source dimensions. In this way, we provide an approximate but common framework with which one source can be compared to another. In sections III-VII we discuss in greater detail ECR, helicon, inductive, helical resonator, and surface wave sources, respectively. Emphasis is placed on electron heating and power absorption, since these are the primary differences between one source and another. In section VIII, we turn to the issue of plasma transport and independent control of ion energy and flux. Obtaining such control is largely independent of the electron heating mechanism but depends critically on source design parameters such as the magnetic field and power absorption profiles. We focus our attention in section VIII on measurements of ion energy distributions, mostly in ECR systems since little data are available from other systems. In sections VIII and IX, we relate ion energy and plasma uniformity, dictated by source design, to processing results such as etching anisotropy, atomic displacement damage, and charge-induced damage. In the final section, we highlight remaining issues and the areas where further investigation is needed.

Throughout this paper we strive to be consistent with dimensional analysis despite not using a consistent set of units. Generally, magnetic field is expressed in gauss, distances in m, cm, or mm, and the electron charge in coulombs. Energies are usually given in units of volts, not eV, so the value of  $e$  is explicitly written. Pressures are given in Torr or mTorr. While this does not conform to international convention, it does conform to common usage. We apologize to the purists.

## I.A Capacitively Coupled Radio Frequency Discharge Sources

Capacitively driven rf discharges—so-called rf diodes—are the most common sources used for materials processing. An idealized source in plane parallel geometry, shown in Fig. 1a, consists of a discharge chamber containing two electrodes separated by a spacing  $l$  and driven by an rf power source. The substrates are placed on one electrode, feedstock gases are admitted to flow through the discharge, and effluent gases are removed by the vacuum pump. Coaxial discharge geometries, such as the "hexode" shown in Fig. 1b, are also in widespread use. When operated at low pressure, with the wafer mounted on the powered electrode, and used to remove substrate material, such reactors are commonly called reactive ion etchers (RIE's)—a misnomer, since the etching is generally a chemical process enhanced by energetic ion

bombardment of the substrate, rather than a removal process due to reactive ions. When operated at higher pressure with the wafer mounted on the grounded electrode, such reactors are commonly referred to as plasma etchers. In terms of the physical properties of these systems, this distinction is somewhat arbitrary.

The physical operation of capacitively driven discharges is reasonably well understood. As shown in Fig. 2 for a symmetrically driven discharge operated at frequencies between the ion and electron plasma frequencies, the mobile plasma electrons, responding to the instantaneous electric fields produced by the rf (13.6 MHz) driving voltage, oscillate back-and-forth within the positive space charge cloud of the ions. At 13.6 MHz, the massive ions respond only to the time-averaged electric fields. Oscillation of the electron cloud creates sheath regions near each electrode that contain net positive charge when averaged over an oscillation period; i.e., the positive charge exceeds the negative charge in the system, with the excess appearing within the sheaths. This excess produces a strong time-averaged electric field within each sheath directed from the plasma to the electrode. Ions flowing out of the bulk plasma near the center of the discharge can be accelerated by the sheath fields to high energies as they flow to the substrate, leading to energetic-ion bombardment, which can enhance, inhibit, or otherwise modify surface reactions. Typical ion bombarding energies  $\epsilon_i$  can be as high as  $V_{rf}/2$  for symmetric systems (Fig. 2) and as high as  $V_{rf}$  at the powered electrode for asymmetric systems (Fig. 1), where  $V_{rf}$ , the rf voltage amplitude (peak rf voltage) between the two electrodes might typically vary between 100 V and 1 kV.

We note that positive ions continuously bombard the electrode over an rf cycle. In contrast, electrons are lost to the electrode only when the oscillating cloud closely approaches the electrode. During that time, the instantaneous sheath potential collapses to near-zero, allowing a sufficient number of electrons to escape to balance the ion charge delivered to the electrode. Except for such brief moments, the instantaneous potential of the discharge must always be positive with respect to any *large* electrode and wall surfaces;<sup>1</sup> otherwise the mobile electrons would quickly leak out. Electron confinement is ensured by the presence of positive space charge sheaths near all surfaces.

The separation of the discharge into bulk and sheath regions is an important paradigm that applies to all discharges. The bulk region is quasi-neutral, and both instantaneous and time-averaged fields are low. The bulk plasma dynamics are described by ambipolar diffusion at high pressures and by free-fall ion loss at low pressures. In the positive space charge sheaths, high fields exist, leading to dynamics that are described by various ion space charge sheath laws, including low voltage sheaths (for high density sources) and various high voltage sheath models (for RF diodes), such as collisionless and collisional Child laws and their modifications (66-73). The plasma and sheath models must be joined at their interface. The usual joining condition is to require that the mean ion velocity at the plasma-sheath edge be equal to the ion-sound (Bohm) velocity  $u_B = (e T_e / M)^{1/2}$ , where  $e$  and  $M$  are the charge and mass of the ion and  $T_e$  is the electron temperature in units of volts.

In the second column of Table 1, typical RF diode source and plasma parameters are given. For anisotropic etching, pressures are in the range 10–100 mTorr, power densities are 0.1–1 W/cm<sup>2</sup>, the driving frequency is typically 13.6 MHz, and multiple wafer systems are common. Plasma densities are relatively low,  $\sim 10^{10}$  cm<sup>-3</sup>, and mean electron energies are of order 5 V, corresponding to Maxwellian electron temperatures of order 3 V. However, non-Maxwellian electron distributions (e.g. two-temperature) are also observed, with the bulk electron temperature sometimes much less than 1 V (74,75). Ion acceleration energies (sheath voltages) are high, >200 V, and fractional ionization is low. The degree of dissociation can range widely from less than 0.1% to nearly 100% depending on gas composition and plasma conditions (76,77). For deposition and isotropic etch applications, pressures tend to be higher and frequencies sometimes lower than the commonly used standard of 13.6 MHz. For example, silicon nitride deposition used for chip encapsulation is ordinarily performed at frequencies between 50 and 500 kHz where relatively large ion bombardment energies are used to tailor film stress and stoichiometry (78).

---

1 Exceptions to this rule are also possible in low frequency electronegative and dc discharges. In the former, the build-up of negative ions can reduce the plasma potential below that of large surfaces in contact with the plasma (64). In the latter, the plasma potential can lie between the two electrode potentials if sufficient current is drawn from the plasma (65).

**TABLE 1: TYPICAL PARAMETERS FOR HIGH EFFICIENCY AND CONVENTIONAL RF PLASMA SOURCES**

<i>Parameter</i>	<i>Units</i>	<i>RF Diode</i>	<i>High Density Source</i>
Pressure $p$	mTorr	10 -1000	0.5-50
Power $P$	W	50 -2000	100 -5000
Frequency $f$	MHz	0.05 -13.6	0 -2450
Volume $V$	l	1-10	2-50
Cross Sectional Area $A$	cm <sup>2</sup>	300 -2000	300 -500
Magnetic Field $B$	kG	0	0 -1
Plasma Density $n$	cm <sup>-3</sup>	10 <sup>9</sup> - 10 <sup>11</sup>	10 <sup>10</sup> - 10 <sup>12</sup>
Electron Temperature $T_e$	V	1-5	2-7
Ion Acceleration Energy $\mathcal{E}_i$	V	200 -1000	20 -500
Fractional Ionization $X_{ii}$	—	10 <sup>-6</sup> - 10 <sup>-3</sup>	10 <sup>-4</sup> - 10 <sup>-1</sup>

### **I.B Limitations of Capacitively Coupled Radio Frequency Discharges**

A crucial limiting feature of RF diodes is that the ion bombarding flux  $\Gamma_i = n\mu_B$  and the ion acceleration energy  $\mathcal{E}_i$  can not be varied independently. The situation is analogous to the lack of independent voltage and current control in diode vacuum tubes or semiconductor pn junctions. Hence, for a reasonable (but relatively low) ion flux, as well as a reasonable dissociation of the feedstock gas, sheath voltages at the driven electrode are high. For wafers placed on the driven electrode, this can result in undesirable damage, or loss of linewidth control. Furthermore, the combination of low ion flux and high ion energy leads to a relatively narrow window for many process applications. The low process rates resulting from the limited ion flux in rf diodes often mandates multiwafer or batch processing, with consequent loss of wafer-to-wafer reproducibility. Higher ion and neutral fluxes are generally required for single wafer processing in a clustered tool environment, in which a single wafer is moved by a robot through a series of process chambers. Clustered tools are used to control interface quality and are said to have the potential for significant cost savings in fabricating integrated circuits (79). Finally, low fractional ionization poses a significant problem for processes where the feedstock costs and disposal of effluents are issues.

To meet the linewidth, selectivity and damage control demands for next-generation fabrication, the mean ion bombarding energy, and its energy distribution, should be controllable independently of the ion and neutral fluxes. Some control over ion bombarding energy can be achieved by putting the wafer on the undriven electrode and independently biasing this electrode with a second RF source. Although these so-called rf triode systems are in use, processing rates are still low at low pressures and sputtering contamination is an issue.

Various magnetically enhanced rf diodes and triodes have also been developed to improve performance of the rf reactor. These include, for example, the Applied Materials' AMT-5000 magnetically enhanced reactive ion etcher (MERIE) and the Microelectronics Center of North Carolina's split cathode RF magnetron. In the AMT MERIE, a DC magnetic field of 50 -300 G is applied parallel to the powered electrode, on which the wafer sits. The magnetic field increases the efficiency of power transfer from the source to the plasma and also enhances plasma confinement. This results in a reduced sheath voltage and an increased plasma density when the magnetic field is applied (80,81). However, the plasma generated is strongly nonuniform both radially and azimuthally due to  $E \times B$  drifts, where  $E$  and  $B$  are the local electric and magnetic fields, respectively. To increase process uniformity (at least azimuthally), the magnetic field is rotated in the plane of the wafer at a frequency of 0.5 Hz. While this is an improvement, MERIE systems do not have good uniformity which may limit their applicability to next-generation, sub-micron device fabrication. Indeed, the strongly nonuniform plasma over the wafer can give rise to a lateral dc current that can damage thin gate oxide films (see Sec. IX.C).

## I.C Overview of High Efficiency Sources

The limitations of rf diodes and their magnetically enhanced variants have led to the development of a new generation of low pressure, high efficiency plasma sources. A few examples are shown schematically in Fig. 3, and typical source and plasma parameters are given in Table 1. In addition to high density and low pressure, a common feature is that the rf or microwave power is coupled to the plasma across a dielectric window, rather than by direct connection to an electrode in the plasma, as for an rf diode. This non-capacitive power transfer is key to achieving low voltages across all plasma sheaths at electrode and wall surfaces. DC voltages, and hence ion acceleration energies, are then typically 20 –30 V at all surfaces. To control the ion energy, the electrode on which the wafer is placed can be independently driven by a capacitively coupled rf source. Hence independent control of the ion/radical fluxes (through the source power) and the ion bombarding energy (through the wafer electrode power) is possible. This subject is discussed at greater length in Sec. VIII.

The common features of power transfer across dielectric windows and separate bias supply at the wafer electrode are illustrated in Fig. 3. However, sources differ significantly in the means by which power is coupled to the plasma. For the electron cyclotron resonance (ECR) source shown in Fig. 3a, one or more electromagnet coils surrounding the cylindrical source chamber generate an axially varying dc magnetic field. Microwave power is injected axially through a dielectric window into the source plasma, where it excites a right hand circularly polarized (RHP) wave that propagates to a resonance zone, for cold electrons, at  $\omega = \omega_{ce}$  where the wave is absorbed. Here  $\omega = 2\pi f$  is the applied radian frequency and  $\omega_{ce} = eB/m$  is the electron gyration frequency at resonance. For the typical microwave frequency  $f = 2450$  MHz used, the resonant magnetic field is  $B \approx 875$  G. The plasma streams out of the source into the process chamber in which the wafer is located.

A helicon source is shown in Fig. 3b. A weak (50 –200 G) dc axial magnetic field along with an rf-driven antenna placed near the dielectric cylinder that forms the source chamber allows excitation of a helicon wave within the source plasma. Resonant wave-particle interaction (Landau damping) is believed to transfer the wave energy to the plasma (82-86) (Sec. IV.D). For the helical resonator source shown in Fig. 3c, the external helix and conducting cylinder surrounding the dielectric discharge chamber form a slow wave structure, i.e. supporting an electromagnetic wave with phase velocity much less than the velocity of light. Efficient coupling of the RF power to the plasma is achieved by excitation of a resonant axial mode (Sec. VI). An inductive (or transformer) coupled source is shown in Fig. 3d. Here the plasma acts as a single-turn, lossy conductor that is coupled to a multiturn non-resonant rf coil across the dielectric discharge chamber; rf power is inductively coupled to the plasma by transformer action (Sec. V). In contrast to the ECR and helicon sources, a dc magnetic field is not required for efficient power coupling in the helical resonator or inductive sources.

Figure 3 also illustrates the use of high density sources to feed plasma into a relatively distinct, separate process chamber in which the wafer is located. As shown in the figure, the process chamber can be surrounded by dc multidipole magnetic fields to enhance plasma confinement near the process chamber surfaces, while providing a magnetic field-free plasma environment at the wafer. Such configurations are often called "remote" sources, another misnomer since at low pressures considerable plasma and free radical production occurs within the process chamber near the wafer (See Sec. VIII.D). Hence such sources are not actually remote. For reasons that are discussed further in Secs. II.A.2, VIII.D, and IX.C, the source and process chambers are sometimes combined, or the wafer is placed very near to the source exit. Such configurations are useful for obtaining increased ion and radical fluxes, reducing the spread in ion energy, and improving process uniformity. But, the wafer is exposed to higher levels of damaging radiation as well (Sec. IX).

Although the need for low pressures, high fluxes and controllable ion energies has motivated high density source development, there are many issues that need to be resolved. A critical issue is achieving the required process uniformity over 200 –300 mm wafer diameters. In contrast to the nearly one dimensional geometry of typical RF diodes (two closely spaced parallel electrodes), high density sources are often cylindrical systems with length-to-diameter ratios of order or exceeding unity. Plasma formation and transport in such geometries is inherently radially nonuniform. Another critical issue is efficient power transfer (coupling) across dielectric windows over a wide operating range of plasma parameters. Degradation of and

deposition on the window can also lead to irreproducible source behavior and the need for frequent, costly cleaning cycles (87). Low pressure operation leads to severe pumping requirements for high deposition or etching rates and hence to the need for large, expensive vacuum pumps. Furthermore, plasma and radical concentrations become strongly sensitive to reactor surface conditions, leading to problems of reactor aging and process irreproducibility. Finally, DC magnetic fields are required for some source concepts. These can lead to magnetic field induced process non-uniformities and damage, as seen, for example, in MERIE systems (88).

## II. PRINCIPLES OF LOW PRESSURE, HIGH EFFICIENCY SOURCE DESIGN

For the pressures of interest (see Table 1), the plasma is not in thermal equilibrium, and local ionization models (89), where the ionization rate is a function of the local field and density only, fail. For all sources, the electrical power is coupled most efficiently to plasma electrons. In the bulk plasma, energy is transferred inefficiently from electrons to ions and neutrals by weak collisional processes; for ions, energy can also be coupled by weak ambipolar electric fields. The fraction of energy transferred by elastic collision of an electron with a heavy ion or neutral is  $2m/M \sim 10^{-4}$ , where  $m$  and  $M$  are the electron and heavy particle masses. Hence the electron temperature  $T_e$  much exceeds the ion and neutral temperatures,  $T_i$  and  $T$ , respectively, in the bulk; typically  $T_e \sim 5$  V whereas  $T_i$  and  $T$  are a few times room temperature (90). A more complete discussion of the ion temperature is given in Sec. VIII. However, dissociation and excitation processes can create a subgroup of relatively high energy heavy particles. Also, the ambipolar electric fields accelerate positive ions toward the sheath edge, and typically, the ions in the bulk acquire a directed energy at the sheath edge of order  $T_e/2$ .

At these low pressures, the mean free path for ionizing electrons, with energies of 10–15 V, is typically comparable to the source dimensions. Hence, even if the electric power is deposited in a small volume within an unmagnetized source, the electron-neutral ionization rate  $\nu_{in}$  is expected to be relatively uniform, since the ionization occurs on the distance scale of this mean free path. In magnetized plasmas, on the other hand, the ionization rate may be highly non-uniform as the magnetized electrons have trouble crossing field lines, so ionization along a magnetic flux tube might be uniform but significant radial non-uniformities may persist. In addition, the propagation and absorption of the exciting electromagnetic fields depend on the charge density distribution. The coupling is non-linear and can give rise to sudden mode changes and instabilities. In some instances, the density profile can steer power into regions of higher or lower density and make the plasma more or less uniform, respectively (91, Sec. III.C).

Although the electron energy distribution function (eedf) need not be Maxwellian, recent Thomson scattering results indicate that this can be a good approximation (92) and at least insightful estimates of source operation can be obtained by approximating the eedf to be a Maxwellian, with  $T_e$  and the various electron collisional rates assumed to be uniform within the bulk plasma.

In high density sources, electron-neutral collisional processes are critical not only for particle production (ionization, dissociation) but also for other collisional energy losses (excitation, elastic scattering). Ion-neutral collisions (charge transfer, elastic scattering) are also important in determining plasma transport and ion energy distribution functions (iedf) at the wafer surface. The myriad of collisional processes that can occur in heavy molecular feedstock gas mixtures can obscure the fundamental principles of high density sources. A noble gas, such as argon, is often used as a reference for describing source operation. The relevant (second order) rate constants  $K_{in}$ ,  $K_{exc}$ , and  $K_{el}$  for electron-neutral ionization, excitation, and elastic scattering in argon are given in Fig. 4 as a function of  $T_e$ . The corresponding rates  $\nu$  ( $s^{-1}$ ) are defined by

$$\nu = KN$$

where  $K$  ( $m^3/s$ ) is the rate constant and  $N$  ( $m^{-3}$ ) is the neutral Ar concentration.

In argon, the cross section for resonant charge transfer of  $Ar^+$  on Ar somewhat exceeds that for elastic scattering. The combined ionic momentum transfer cross section  $\sigma_i$  for these two processes is large ( $\sigma_i \approx 10^{-18} m^2$ ) and relatively constant for the ion energies of interest. The corresponding ion-neutral mean free path is

$$\lambda_i = \frac{1}{N \sigma_i} .$$

For the sake of comparing the efficiency of one source with another, it is useful to define the collisional energy  $\mathcal{E}_c$  lost per electron-ion pair created in the system. For single-step, electron-impact ionization,

$$K_{ix} \mathcal{E}_c = K_{ix} \mathcal{E}_{ix} + K_{exc} \mathcal{E}_{exc} + K_{el}(2m/M)(3T_e/2), \quad (2.1)$$

where  $\mathcal{E}_{ix}$ ,  $\mathcal{E}_{exc}$  and  $\mathcal{E}_{el} \approx (3m/M)T_e$  are the energies lost by an electron as a result of ionization, excitation and elastic collisions, respectively. While the last term may appear negligible for large electron temperatures, it is important for  $T_e < 2$  V, where it is dominant. The energy  $\mathcal{E}_c$  is lost when the electron-ion pair is subsequently lost. In a monatomic gas such as Ar, the dominant loss mechanism at low pressure is simply flow to the walls and this loss rate in steady-state must be balanced by the rate of formation, which accounts for the factor  $K_{ix}$  on the left hand side of (2.1). Note that for simplicity we have lumped all excitation channels into one effective level characterized by energy  $\mathcal{E}_{exc}$ . While this is crude, again it offers a simple, rapid means for comparing one source to another. In general, a detailed energy balance including many excited states and multi-step ionization pathways must be considered if quantitative comparisons are to be made. The quantity  $\mathcal{E}_c$ , which within the framework of the assumptions above, is a function of  $T_e$  alone, is shown for Ar in Fig. 5. For the excitation process, a composite cross section is used from Egarter (93), with an excitation energy of 11.97 V. For ionization, the cross section from Peterson and Allen (94) is used. The elastic cross section is from the data in Hayashi (95).

In addition to collisional energy losses, electrons and ions carry kinetic energy to the walls (Sec. VIII). For Maxwellian electrons, the mean kinetic energy lost per electron lost is  $\mathcal{E}_e = 2T_e$ . The mean kinetic energy lost per ion lost is  $\mathcal{E}_i$ , which is mainly due to the dc potential across the sheath (Sec. II.A.2 and VIII). Summing the three contributions yields the total energy lost per ion lost from the system:

$$\mathcal{E}_L = \mathcal{E}_c + 2T_e + \mathcal{E}_i . \quad (2.2)$$

The principle of high density source operation, such as for the cylindrical plasma shown in Fig. 6, can be understood from the overall source power balance, written in terms of  $\mathcal{E}_L$  as

$$P_{abs} = en_s u_B A_{eff} \mathcal{E}_L , \quad (2.3)$$

where  $P_{abs}$  is the power absorbed by the plasma,  $n_s$  is the ion density at the plasma-sheath edge, and  $A_{eff}$  is the effective area for particle loss. The Bohm (ion loss) velocity  $u_B$  is relatively constant for a given ion mass and for the typical limited range of  $T_e$ 's. Hence  $n_s$  can be increased by reducing  $\mathcal{E}_L$ , reducing  $A_{eff}$ , or increasing  $P_{abs}$ . All three strategies are used. First,  $\mathcal{E}_L$  is lowered by reducing sheath voltages from, for example,  $\mathcal{E}_i \approx 360$  V (for RF diodes) to  $\approx 40$  V (for high density sources). For Ar, with  $\mathcal{E}_c + 2T_e \approx 40$  V, this results in a five-fold increase in  $n_s$ . Second, the loss area for a cylindrical unmagnetized source having radius  $R$  and length  $L$  can be effectively reduced from  $2\pi R^2 + 2\pi RL$  to  $2\pi R^2$  if a strong axial magnetic field is applied to inhibit radial particle loss. This reduction in  $A_{eff}$  can be important for certain ECR sources. Third,  $P_{abs}$  can be increased from, say, 500 W for a typical RF diode to 2 kW or more for a high density source, without substantially increasing the ion bombarding energy.

The relation between the density  $n_s$  at the sheath edge and the density  $n_0$  at the plasma center is complex, because the ambipolar transport of ions and electrons spans the regime  $\lambda_i \sim R, L$ , depending on the pressure and the values for  $R$  and  $L$ . Assuming uniform ionization at very low pressures or small reactors,  $\lambda_i \gg R, L$ , the ion transport is collisionless and well described by an ion free-fall profile (96) within the bulk plasma. This profile is relatively flat near the plasma center and dips near the sheath edge, with  $n_s/n_0 \approx 0.50$  for  $R \gg L$  (planar geometry) and  $n_s/n_0 \approx 0.40$  for  $L \gg R$  (infinite cylinder geometry). At higher pressures or larger reactors such that  $\lambda_i \ll R, L$ , transport is diffusive and ambipolar. However, the usual diffusion solution for a constant diffusion coefficient (97), consisting of a  $J_0$  Bessel function variation along  $r$  and a cosine variation along  $z$ , does not describe the profile well, because at these low (but diffusive) pressures, the magnitude of the ion transport velocity  $u_i$  much exceeds the ion thermal velocity

$u_{Ti}$  over most of the bulk plasma. In this regime, the ion transport is mobility limited,

$$u_i = \mu_i E, \quad (2.4)$$

with  $E$  the ambipolar electric field and

$$\mu_i \approx \frac{2e\lambda_i}{\pi M |u_i|} \quad (2.5)$$

the mobility (98). For electrons in near thermal equilibrium,

$$E = -T_e \nabla n/n, \quad (2.6)$$

which leads to the usual Boltzmann equilibrium relating the spatially varying plasma potential  $\Phi$  to the density,

$$n = n_0 e^{\Phi/T_e}. \quad (2.7)$$

Along with particle conservation and the assumption of uniform ionization, (2.4) and (2.7) lead to a non-linear transport equation in the bulk plasma, which has been solved by Godyak (99) in one dimensional planar geometry ( $R \gg L$ ) and by Godyak and Maximov (100) for infinite cylinder geometry ( $L \gg R$ ). The profiles are relatively flat in the center but fall steeply at the sheath edge. The profile has not been determined for a finite cylinder or for the intermediate mean free path regime  $\lambda_i \sim R, L$ . However, joining the collisionless and collisional results leads to the following rough estimates:

$$h_L \equiv \frac{n_{eL}}{n_0} \approx 0.86 \left[ 3 + \frac{L}{2\lambda_i} \right]^{-1/2} \quad (2.8)$$

at the axial sheath edge and

$$h_R \equiv \frac{n_{eR}}{n_0} \approx 0.80 \left[ 4 + \frac{R}{\lambda_i} \right]^{-1/2} \quad (2.9)$$

near the radial sheath edge.

## II.A Unified Analysis of Source Operation

Let us consider a simple high density source model to estimate important plasma parameters and see the way these vary with power, pressure, and source geometry: the electron temperature  $T_e$ , the ion bombarding energy  $\mathcal{E}_i$ , the plasma density  $n_0$ , and the ion current density  $J_i$ . Referring to Fig. 6, we assume a uniform (in the bulk) cylindrical source plasma with Maxwellian electrons absorbing an electrical power  $P_{abs}$  and ionization by single-step electron impact.

*II.A.1 Electron Temperature* We first determine  $T_e$ . Let ion-electron pairs be created in the bulk plasma volume by electron-neutral ionization and lost by flow to the walls. Equating the total volume ionization to the surface particle loss,

$$K_{iz} N n_0 \pi R^2 L = n_0 u_B (2\pi R^2 h_L + 2\pi R L h_R), \quad (2.10)$$

we solve to obtain

$$\frac{K_{iz}(T_e)}{u_B(T_e)} = \frac{1}{N d_{eff}}, \quad (2.11)$$

where

$$d_{eff} = \frac{1}{2} \frac{RL}{Rh_L + Lh_R} \quad (2.12)$$

is an effective plasma size, and the  $T_e$  dependence of  $K_{ix}$  and  $u_B$  is explicitly shown. Given  $N$  and  $d_{eff}$ , we can solve (2.11) for  $T_e$ , obtaining, for argon with  $K_{ix}$  shown in Fig. 4, the result for  $T_e$  shown in Fig. 7. We see that  $T_e$  varies over a narrow range between 2 and 5 volts for typical source pressures and sizes. We also note that the density  $n_0$  cancels out in (2.10) as a result of our single-step ionization assumption. Hence, in this limit,  $T_e$  is determined by particle conservation, i.e. the ratio of the ion creation to the ion loss rate, independent of density, and therefore input power.

*II.A.2 Ion Bombarding Energy* We next discuss  $\mathcal{E}_i$ , which is the sum of the ion energy entering the sheath and the energy gained by the ion as it traverses the sheath. The ion velocity entering the sheath is  $u_B$ , corresponding to a directed energy of  $T_e/2$ . The sheath voltage  $V_s$  (see Fig. 8) can be estimated from particle conservation in the sheath. The wall sheath thickness  $s$  rarely exceeds a few Debye lengths  $\lambda_{De}$ , where  $\lambda_{De} \approx 7430 (T_e/n_e)^{1/2}$  m, with  $T_e$  in volts and  $n_e$  in  $m^{-3}$ . Since the sheath is typically much less than a millimeter thick and is much less than a mean free path for ionization in typical high density sources, the fluxes of both ions and electrons are conserved. The ion and electron fluxes at the wall are

$$\Gamma_i = n_i u_B \quad (2.13)$$

and

$$\Gamma_e = \frac{1}{4} n_e u_e e^{V_s/T_e}, \quad (2.14)$$

where

$$u_e = \left( \frac{8eT_e}{\pi m} \right)^{1/2} \quad (2.15)$$

is the mean electron speed. The Boltzmann factor in (2.14) accounts for the reduction in the electron density at the wall due to the repulsive potential within the sheath. For an insulating wall, the ion and electron fluxes must balance in the steady state. Equating (2.13) to (2.14) yields

$$V_s = \frac{T_e}{2} \ln \left( \frac{M}{2\pi m} \right), \quad (2.16)$$

or  $V_s \approx 4.7 T_e$  for argon. Accounting for the initial ion energy, we obtain  $\mathcal{E}_i \approx 5.2 T_e$ . At a conducting wall, the fluxes need not balance, although the integrated fluxes (particle currents) must balance. However, if the fluxes are not too dissimilar, than (2.16) remains a good estimate due to the logarithmic dependence of  $V_s$  on the ratio of fluxes.

The ion energy  $\mathcal{E}_i$  can significantly exceed  $V_s$  due to several reasons. In some high density sources, the plasma flows from the source chamber into a larger diameter process chamber (see Fig. 3). As the plasma expands into the process chamber, the plasma density drops from  $n_0$  to, say,  $n_p$ . This leads to an additional distributed sheath potential  $V_d$  determined by the Boltzmann relation (2.7),

$$V_d = T_e \ln \frac{n_0}{n_p}, \quad (2.17)$$

which accelerates ions within the process chamber (see Sec. VIII.D). Ions gain the full potential  $V_d$  for sufficiently low pressures,  $\lambda_i \gg L_d$ , where  $L_d$  is the characteristic length over which  $V_d$  occurs, and can gain a fraction  $(-\lambda_i/L_d)V_d$  of this potential for  $\lambda_i < L_d$ . As we shall see in Sec. VIII.D,  $L_d$  can be small

compared to  $\lambda_i$  and characteristic reactor dimensions.

Additional ion bombarding energy can be gained near dielectric windows adjacent to the RF powered conductors that drive the source, or near separately driven RF electrodes embedded in the plasma, such as the wafer holder (Sec VIII.E). In both cases, the mechanism is capacitive coupling of the RF power source to the plasma. Careful design of the coupling structure could be used to minimize or eliminate capacitive coupling from the rf powered conductors across the dielectric window to the plasma, but the design principles are not entirely clear and some enhanced ion bombardment energies can exist in rf driven helicons, helical resonators, and inductively driven sources due to this mechanism. On the other hand, the *desired* ion bombarding energy at an RF powered wafer holder can be strongly enhanced over that obtained from (2.16). Letting  $\bar{V}_{pw}$  be the plasma to wafer holder rf voltage amplitude and  $\bar{V}_{pw}$  be the plasma to wafer holder dc voltage, then we find that  $\epsilon_i \approx 5.2 T_e$  in the low voltage limit  $\bar{V}_{pw} \ll V_s$ , and that  $\epsilon_i \approx \bar{V}_{pw} \approx 0.8 \bar{V}_{pw}$  in the high voltage limit  $\bar{V}_{pw} \gg V_s$  (71). An estimate for  $\epsilon_i$  over the entire range of driving rf voltages is given by Godyak and Sternberg (73). The additional ion energy flux  $en_s u_B \epsilon_i$  striking the wafer holder is supplied by the RF power source driving the holder in the high voltage limit.

The thickness of the sheath in the high voltage limit follows that of a modified ion Child law:

$$en_s u_B \approx 0.8 \epsilon_0 \left( \frac{2e}{M} \right)^{1/2} \frac{\bar{V}_{pw}^{3/2}}{s^2} . \quad (2.18)$$

If  $n_s$ ,  $T_e$  and  $\bar{V}_{pw} \approx 0.8 \bar{V}_{pw}$  are known, then (2.18) determines  $s$ . For typical RF driven wafer holders,  $s$  is a few millimeters (101). This is still small compared to  $\lambda_i$  and the sheath is collisionless.

We see from the above discussion that estimating ion energy is not so simple as it depends on not only electron temperature but also source geometry and the application of bias voltages. This subject is discussed at greater length along with a review of experimental measurements in Sec. VIII.

**II.A.3 Plasma Density and Ion Current Density** Finally, we estimate the plasma density  $n_0$ . Accounting for possibly different values of  $n_s$  at the axial and radial sheath edges (Eqs. 2.8 and 2.9), we solve (2.3) to obtain

$$n_0 = \frac{2P_{abs}}{eu_B A_{eff} \epsilon_L} , \quad (2.19)$$

where

$$A_{eff} \equiv 4\pi R(Rh_L + Lh_R) . \quad (2.20)$$

For a specified  $P_{abs}$ , and  $T_e$  determined from Fig. 7, we obtain  $n_0$  from (2.19). Note that within the assumption of single-step ionization,  $n_0$  is determined by the total power balance in the discharge and is a function of pressure through the dependence of  $h_L$  and  $h_R$  on  $p$  and through the weaker dependence of  $T_e$  on  $p$ .

As an example, let  $R = 0.15$  m,  $L = 0.3$  m,  $N = 3.3 \times 10^{19}$  m<sup>-3</sup> ( $p = 1$  mTorr at 298K), and  $P_{abs} = 800$  W. At 1 mTorr,  $\lambda_i \approx 0.03$  m. Then from (2.8) and (2.9)  $h_L = h_R \approx 0.3$ , from (2.12)  $d_{eff} \approx 0.17$  m, and from Fig. 7,  $T_e \approx 4.1$  V. From Fig. 5,  $\epsilon_c \approx 42$  V. Using (2.2) with  $\epsilon_i \approx 5.2 T_e \approx 21$  V, we find  $\epsilon_L \approx 72$  V. The Bohm velocity is  $u_B \approx 3.1 \times 10^3$  m/s, and  $A_{eff} \approx 0.25$  m<sup>2</sup>. Then (2.19) yields  $n_0 \approx 1.8 \times 10^{17}$  m<sup>-3</sup>, corresponding to a flux at the axial boundary  $\Gamma_{iL} \approx 1.7 \times 10^{20}$  /m<sup>2</sup>-s or an ion current density of  $J_{iL} \approx 2.7$  mA/cm<sup>2</sup>.

If a strong dc magnetic field is applied along the cylinder axis, then particle loss to the circumferential wall is inhibited. In the limit of no radial loss,  $d_{eff} = L/(2h_L) \approx 0.5$  m in (2.11), and we obtain  $T_e \approx 3.3$  V,  $\epsilon_c \approx 46$  V,  $\epsilon_i \approx 17$  V,  $\epsilon_L \approx 70$  V,  $u_B \approx 2.8 \times 10^3$  m/s,  $A_{eff} = 4\pi R^2 h_L \approx 0.085$  m<sup>2</sup>,  $n_0 \approx 5.8 \times 10^{17}$  m<sup>-3</sup>, and  $J_{iL} \approx 7.8$  mA/cm<sup>2</sup>. There is a significant increase in charge density and ion flux due to the magnetic field.

## II.B Discharge Heating

The preceding discussion provides a unified framework for qualitatively understanding rf- and microwave-driven high density sources, at least in argon gas. However, issues such as energy transfer from power source to plasma electrons, coupling across dielectric windows, and ion flux uniformity depend on specific source concepts, geometries, and magnetic configurations. Possible electron heating mechanisms include:

- (a) Secondary electron emission heating
- (b) Stochastic (collisionless) heating
- (c) Ohmic (collisional) heating
- (d) Resonant wave-particle interaction heating

Achieving adequate electron heating is a central issue because, although the heated electrons provide the ionization required to sustain the discharge, they tend to short out the applied heating fields within the bulk plasma. Hence electron heating in high density sources occurs either near the plasma-sheath edge, as in (a)–(c) above, or by generation near the sheath edge of plasma waves that are subsequently absorbed within the bulk, as in (d).

Secondary emission heating is not believed to play a central role in low pressure high density sources because ion bombarding energies are relatively low, and hence the secondary emission is low. A possible exception is at a capacitively driven wafer holder for highly directional etch applications, such as metals, where the sheath voltages are driven to the range 50–150 V. However, the mean free path for a 100 volt electron in a 1 mTorr argon discharge is about 1.5 meters. Hence, these electrons pass only once through the system before being lost, unless the geometry and magnetic configuration are specifically designed to retain them, as in DC- and RF-driven planar magnetron discharges commonly used for sputtering thin films. These discharges are beyond the scope of this review, and the reader is referred to the relevant literature (102-105).

Stochastic electron heating has been found to be a powerful mechanism in low pressure rf diodes. Here electrons impinging on the oscillating sheath edge suffer a change of velocity upon reflection back into the bulk plasma. As the sheath moves into the bulk, the reflected electrons gain energy; as the sheath moves away, the electrons lose energy. However, averaging over an oscillation period, there is a net energy gain. The mechanism is analogous to the energy gained by a ball when hit by a tennis racket and the term stochastic is used to denote the probabilistic nature of the electron collision with the sheath. In a low pressure, high density source, this mechanism acts at capacitively coupled rf powered surfaces such as the wafer holder. For high bias voltages,  $\tilde{V}_{pw} \gg V_s$ , an estimate of the electron heating energy flux is (72,106)

$$S_e \approx 0.48 \frac{m}{2e} \omega^2 \epsilon_0 u_e \tilde{V}_{pw} \quad (2.21)$$

which, when summed along with the ion energy flux  $S_{ion} \approx en_s u_B \epsilon_i$ , gives the bulk (neglecting ohmic heating) of the energy flux (power density) supplied by the rf wafer-bias source. Stochastic heating is important for understanding the dynamics of rf diodes, triodes and MERIE's; there is also some evidence (107) that a similar non-collisional stochastic heating mechanism acts in low pressure high density inductively driven sources. This issue is considered further in a subsequent section (Sec. V.B).

Ohmic heating due to the in-phase components of the rf current density and rf electric field is an important mechanism for rf diodes, especially at high pressures. The time averaged ohmic energy flux is

$$S_{ohm} = \frac{1}{2} \text{Re} (\tilde{J} \cdot \tilde{E}^*) , \quad (2.22)$$

where  $\tilde{J}$  and  $\tilde{E}$  are the complex amplitudes of the rf current density and electric field in the bulk plasma, respectively, Re denotes the real part, and \* denotes complex conjugate. Ohmic heating is also an important energy deposition mechanism in inductive sources, where it occurs in a thin skin near the plasma-sheath edge, as will be seen (Sec. V.B).

While the preceding three mechanisms are central to understanding electron heating in rf diodes, the role of wave-particle interactions in electron heating in high density sources is unique. As will be shown, a number of source concepts, particularly ECR's and helicons, rely on this as the primary heating mechanism.

### III. ELECTRON CYCLOTRON RESONANCE (ECR) DISCHARGES

Microwave generation of plasma has been employed since the invention of high power microwave sources in World War II. At low plasma densities, the high electric fields obtainable in a resonant microwave cavity can break down a low pressure gas and sustain a discharge. For good field penetration in the absence of a magnetic field,  $\omega_{pe} \leq \omega$ , which sets a critical density limit  $n_c \leq \omega^2 \epsilon_0 m / e^2$ , or, in practical units,  $n_c \text{ (m}^{-3}\text{)} \leq 0.012 f^2$ , with  $f$  in Hz. More restrictively, for the high fields required the cavity  $Q$  must be high, further limiting the range of operation (108).

The introduction of a steady magnetic field  $B$ , in which there is a resonance between the applied frequency  $\omega$  and the electron cyclotron frequency  $\omega_{ce} = eB/m$  somewhere within the discharge, allows operation at high density and without a cavity resonance. Because of the cyclotron resonance, the gyrating electrons rotate in phase with the right hand polarized (RHP) wave, seeing a steady electric field over many gyro-orbits. Thus the high field of the cavity resonance, acting over a short time, is replaced by a much lower field, but acting over a much longer time. The net result is to produce sufficient energy gain of the electrons to allow ionization of the background gas. Furthermore, the injection of the microwaves along the magnetic field, with  $\omega_{ce} > \omega$  at the entry into the discharge region, allows wave propagation to the absorption zone  $\omega_{ce} \approx \omega$ , even in a dense plasma with  $\omega_{pe} > \omega$  or  $n_0 > n_c$  (109).

These discharges have low ion bombarding energy, low pressure, and high fractional ionization, compared to conventional rf diodes. Consequently, ECR discharges are seeing increasing usage in the semiconductor industry for etching and deposition processes. For example, Hitachi ECR tools have been used in integrated circuit production since 1985 for 6 inch polysilicon etch processes and since 1988 for 8 inch metal etch processes, with over 500 machines in worldwide use as of the summer of 1992 (110).

#### III.A Source Configurations

Figure 9a shows a typical high profile, i.e.  $L > R$ , ECR system, with the microwave power injected along the magnetic field lines. The power  $P_{\mu w}$  at frequency  $f = \omega/2\pi$  is coupled through a vacuum end-window into a cylindrical metal source chamber, which is often lined with a dielectric to minimize metal contamination resulting from wall sputtering (Sec. IX.B, 87,101,111-113). One or several magnetic field coils are used to generate a nonuniform, axial magnetic field  $B(z)$  within the chamber. The magnetic field strength is chosen to achieve the ECR condition,  $\omega_{ce}(z_{res}) \approx \omega$ , where  $z_{res}$  is the axial resonance position. When a low pressure gas is introduced, the gas breaks down and a discharge forms inside the chamber. The plasma streams or diffuses along the expanding magnetic field lines into a process chamber toward a wafer holder. Energetic ions and free radicals generated within the entire discharge region (source and process chambers, Sec. VIII) impinge on the wafer. A magnetic field coil at the wafer holder is often used to modify the uniformity of the etch or deposition process.

Typical parameters for ECR discharges used for semiconductor materials processing are shown in the last column of Table 1. The electron cyclotron frequency  $f_{ce}$  (MHz)  $\approx 2.8 B$ , with  $B$  in gauss. For  $f_{ce} = f = 2450$  MHz, we obtain a resonant magnetic field  $B_{res} \approx 875$  G. A typical source diameter is 15 cm.

In some cases, there are multiple resonance positions, as shown in Fig. 9b. A uniform profile is never used because of the difficulty of maintaining exact resonance and the possibility of overheating the electrons. The monotonically decreasing profile  $dB/dz < 0$  shown as the solid line in Fig. 9b, with one resonant zone near the window, is often used. The mirror profile shown as the dashed line in Fig. 9b has one resonant zone near the window and two additional zones under the second magnet. This profile can yield higher ionization efficiencies, due to enhanced confinement of hot (superthermal) electrons that are magnetically trapped between the two mirror (high-field) positions. However, the high profile (long length) of the source chamber leads to enhanced radial diffusion at high pressures and consequently may reduce

plasma densities at the wafer holder.

A typical microwave power system is shown in Fig. 10. A DC power supply drives a magnetron source<sup>2</sup> coupled to the discharge by means of a  $TE_{10}$  waveguide transmission system. This consists of a circulator, to divert reflected power to a water-cooled, matched load; a directional coupler, to monitor the transmitted and reflected power; a multi-screw tuner, to match the source to the load through the dielectric window, achieving a condition of low reflected power; and, often, a mode converter, to convert the  $TE_{10}$  linear polarized, rectangular waveguide mode to an appropriate mode in the cylindrical source chamber. The simplest mode converter (Fig. 11a) is from  $TE_{10}$  rectangular to  $TE_{11}$  circular mode. At 2450 MHz, the minimum source chamber diameter for  $TE_{11}$  mode propagation (in vacuum) is 7.18 cm (115). However, the electric field profile and corresponding power flux is peaked on axis and is not azimuthally symmetric for this mode, leading to possible non-axisymmetric processing profiles on the wafer. A common converter to an axisymmetric mode configuration (Fig. 11b) is from  $TE_{10}$  rectangular to  $TM_{01}$  circular mode, having a minimum diameter for mode propagation of 9.38 cm at 2450 MHz. The profile is ring-like, with a vanishing on-axis power flux. The electric field for both modes is linearly polarized, consisting of equal admixtures of RHP and LHP waves. The basic power absorption mechanism is the absorption of the RHP wave on a "magnetic beach", where the wave propagates from higher to lower magnetic field to the resonance  $\omega_{ce}(B) = \omega$ . The fate of the LHP wave is unclear but it is probably slowly, and inefficiently, converted to a RHP wave as the power reflects from surfaces or a critical density layer in the source. A more efficient scheme is to use a microwave polarizer and convert from  $TE_{10}$  rectangular to a  $TE_{11}$  circular mode structure that rotates in the right hand sense at frequency  $\omega$  (116). This yields a time-averaged azimuthally symmetric power profile peaked on axis and having an on-axis electric field that is right hand polarized. Hence, most of the power can be delivered to the plasma in the form of the RHP wave alone.

ECR process tools come in a variety of "flavors". A basic distinction is in coupling the microwave power to the resonance zone. The three categories are (1) traveling wave propagation mainly along  $B_0$  (wavevector  $k \parallel B_0$ ), (2) propagation mainly across  $B_0$  ( $k \perp B_0$ ), and (3) standing wave excitation (mainly cavity coupled). While these distinctions are useful, most ECR sources rely on the "magnetic beach" absorption of the RHP wave. Additionally, the sources are not neatly broken into these categories; e.g., wave propagation is at an angle to  $B_0$ , and absorption can involve standing waves (117).

Various ECR configurations are shown in Fig. 12. A high profile (far from the wafer) source with microwave injection along  $B_0$  is shown in Fig. 12a. The resonance (heating) zone can be ring- or disk-shaped (the latter is shown) and may be as much as 50 cm from the wafer. Expansion of the plasma from the resonance zone to the wafer reduces the ion flux and increases the ion impact energy at the wafer. Hence high profile sources have given way to low profile (close to the wafer) sources shown in Fig. 12b, where the resonance zone may be only 10 - 20 cm from the wafer. Uniformity is controlled at least in part by shaping the axial magnetic field. Uniformity can be further improved and density increased by adding 6-12 linear multidipole permanent magnets around the circumference of the process chamber (118), as shown in Fig. 12c. As a variation, a strong (rare earth) permanent magnet can also replace the source coil (119). Another approach to achieving adequate uniformity and density is to combine the source and process chambers and place the resonance zone close to the wafer, leading to the close-coupled configuration shown in Fig. 12d (31). Uniformity requirements can be met by using a relatively flat, radially uniform resonance zone (120).

The multidipole, distributed ECR system shown in Fig. 12e is powered by microwave injection perpendicular to the strong, permanent magnet, multidipole magnetic fields. Typically, four or more microwave applicators are arranged around the circumference to achieve adequate uniformity (121). Each applicator creates an approximately linear resonance zone near the process chamber wall as shown.

---

<sup>2</sup> Samukawa (114) has recently shown that power fluctuations with magnetron sources can result in unstable operation and broadening of the ion energy distribution functions. Operation with a klystron microwave source helped to avoid these problems.

A microwave cavity source is shown in Fig. 12f. The coaxial feed is tuned using a sliding short on top and a stub tuner from the side (3,5). In earlier, lower density versions, a grid was used below the plasma generation region providing microwave containment while allowing the plasma to diffuse out. The linear resonance zones, similar to those in the DECR (Fig. 12e), are generated by a set of 8–12 strong permanent magnets arranged around the circumference of the source chamber as shown (122).

### III.B Electron Heating

The basic principle of ECR heating is illustrated in Fig. 13. A linearly polarized microwave field launched into the source chamber can be decomposed into the sum of two counter-rotating circularly polarized waves. Assuming a sinusoidal steady state with the incident wave polarized along  $\hat{x}$ ,

$$\mathbf{E}(\mathbf{r}, t) = \text{Re} [\hat{x} E_x(\mathbf{r}) e^{j\omega t}] , \quad (3.1)$$

we have

$$\hat{x}E_x = (\hat{x} - j\hat{y})E_{rhp} + (\hat{x} + j\hat{y})E_{lhp} , \quad (3.2)$$

where  $\hat{x}$  and  $\hat{y}$  are unit vectors along  $x$  and  $y$  and where  $E_{rhp}$  and  $E_{lhp}$  are the amplitudes of the RHP and LHP waves, with  $E_{rhp} = E_{lhp} = E_x/2$ . The electric field vector of the RHP wave rotates in the right hand direction (counter-clockwise around  $\mathbf{B}_0$ ) at frequency  $\omega$  while an electron in a uniform magnetic field  $B_0$  also gyrates counter-clockwise at frequency  $\omega_{ce}$ . Consequently, as shown in Fig. 13a, for  $\omega_{ce} = \omega$ , the force  $-eE$  accelerates the electron along its circular orbit, resulting in a continuous transverse energy gain. In contrast, as shown in Fig. 13b, the LHP wave field produces an oscillating force whose time average is zero, resulting in no energy gain.

To determine the overall heating power, the nonuniformity in the magnetic field profile  $B(z)$  must be considered. For  $\omega_{ce} \neq \omega$ , an electron does not continuously gain energy, but rather its energy oscillates at the difference frequency  $\omega_{ce} - \omega$ . As an electron moving along  $z$  passes through resonance, its energy oscillates as shown in Fig. 13c, leading to an average transverse energy  $W_{ECR}$  gained in one pass. For low power absorption, where the electric field at the resonance zone is known, the heating can be estimated as follows. We expand the magnetic field near resonance as

$$\omega_{ce}(z') = \omega(1 + \alpha z') , \quad (3.3)$$

where  $z' = z - z_{res}$  is the distance from exact resonance,  $\alpha = \partial\omega_{ce}/\partial z'$  is proportional to the gradient in  $B(z)$  near the resonant zone, and we approximate  $z'(t) = u_{res}t$ , where  $u_{res}$  is the parallel speed at resonance. The energy gain can be written in the form  $W_{ECR} = (1/2) m(\Delta u)^2$ , where from Newton's second law  $\Delta u = (e/m)Et_{res}$  and  $t_{res}$  is the effective time in resonance. To estimate  $t_{res}$  we note that an electron passing through the zone coherently gains energy for a time  $t_{res}$  such that

$$|\omega - \omega_{ce}(u_{res}t_{res})| t_{res} \approx 2\pi . \quad (3.4)$$

Inserting (3.3) into (3.4), using the definition for  $z'$  and solving for  $t_{res}$ , we obtain

$$t_{res} = |2\pi/\omega\alpha u_{res}|^{1/2} . \quad (3.5)$$

The effective resonance width (see Fig. 13c) is

$$\Delta z_{res} = u_{res}t_{res} , \quad (3.6)$$

which, for typical ECR parameters, is  $\approx 0.5$  cm. The energy gain per pass is thus

$$W_{ECR} = \frac{\pi e^2 E_{rhp}^2}{m\omega |\alpha u_{res}|} . \quad (3.7)$$

The absorbed power per unit area, or energy flux, is found by integrating (3.7) over the flux of electrons incident on the zone, yielding

$$S_{ECR} = \frac{\pi n e^2 E_{rhp}^2}{m\omega |\alpha|} . \quad (3.8)$$

A more careful derivation of this result, including the effect of non-constant  $u_{res}$  during passage through resonance, is given by Jaeger et al. (123). We see that  $S_{ECR}$  is proportional to the density, the scale length  $\alpha^{-1}$  of the magnetic field variation, and the square of the RHP electric field amplitude at the resonance, and is independent of the axial electron velocity.

### III.C Resonant Wave Absorption

A serious limitation on the result (3.8) is that it assumes the electric field within the resonance zone is constant and known from the input power. That this cannot be true in the case of strong absorption is clear, since the absorbed power cannot exceed the incident power. The resolution of this difficulty lies in the attenuation of the wave in the resonance zone, so that the resonant value of  $E_{rhp}$  is in fact much smaller than the value of the incident  $E_{rhp}$ .

The propagation and absorption of microwave power in ECR sources is an active area of research and is not fully understood. For excitation at an end window (Figs. 12a-d), the waves in a cylindrical magnetized plasma are neither exactly RHP nor propagating exactly along  $B_0$ . The waves are not simple plane waves and the mode structure in a magnetized plasma of finite dimension must be considered. Nevertheless, the essence of the wave coupling, transformation and absorption at the resonance zone can be understood by considering the one dimensional problem of an RHP plane wave propagating strictly along  $B_0$ . For right hand polarization,

$$E_{rhp} = \text{Re} [(\hat{x} - j\hat{y}) E_{rhp}(z) e^{j\omega t}] , \quad (3.9)$$

where  $E_{rhp}$  is the spatially varying electric field amplitude. The wave equation for plane waves propagating along  $B_0$  parallel to  $z$  can be written (124,125)

$$\frac{d^2 E_{rhp}}{dz^2} + k_0^2 \mathcal{K}_r E_{rhp} = 0 , \quad (3.10)$$

where far from resonance such that  $\omega - \omega_{ce} \gg \nu_c$ , the electron-neutral collision frequency,

$$\mathcal{K}_r = 1 - \frac{\omega_{pe}^2(z)}{\omega(\omega - \omega_{ce}(z))} \quad (3.11)$$

is the relative dielectric constant, and  $k_0 = \omega/c$ , with  $c$  the velocity of light.  $\mathcal{K}_r$  varies with  $z$  due to the dependence of  $\omega_{pe}^2$  on the density  $n(z)$  and of  $\omega_{ce}$  on the magnetic field  $B(z)$ . If the variation of  $\mathcal{K}_r$  with  $z$  is weak, then a Wentzel-Kramers-Brillouin (WKB) wave expansion can be made (126),

$$E_{rhp} = E_{rhp0}(z) \exp \left[ -j \int k_r(z') dz' \right] , \quad (3.12)$$

where

$$k_r(z) = k_0 \mathcal{K}_r^{1/2}(z) \quad (3.13)$$

is the spatially varying propagation constant, with  $\lambda_r = 2\pi/k_r$ , the local wavelength. The WKB wave propagates without reflection or absorption for  $\mathcal{K}_r > 0$ , since  $k_r$  is real, and the wave is evanescent for  $\mathcal{K}_r < 0$ , since  $k_r$  is imaginary.

To illustrate the propagation and absorption of a wave traveling into a decreasing magnetic field from a region where  $\omega_{ce} > \omega$ , we let  $\omega_{pe}^2 = \text{const}$  and  $\omega_{ce}$  vary linearly with  $z$  as given in (3.3). Then  $\mathcal{K}_r$  is plotted versus  $\omega_{ce}(z)/\omega$  in Fig. 14a for low density ( $\omega_{pe} < \omega$ ) and in Fig. 14b for high density ( $\omega_{pe} > \omega$ ). The wave travels from right (upstream of the resonance,  $\omega_{ce} > \omega$ ) to left ( $\omega_{ce} < \omega$ ) on this figure. The wave is evanescent downstream of the resonance in the region

$$1 - \frac{\omega_{pe}^2}{\omega^2} < \frac{\omega_{ce}}{\omega} < 1, \quad (3.14)$$

and is propagating otherwise. For  $\omega_{pe} \ll \omega$ , the region of evanescence is thin (in  $z$ ), and the wave can tunnel through this region to propagate again further downstream. As  $\omega_{pe}$  increases toward  $\omega$ , less power can tunnel through. For  $\omega_{pe} > \omega$ , the wave is always evanescent downstream of the resonance.

For WKB wave propagation, the time averaged power per unit area carried by the wave is

$$S_r = \frac{1}{2} Z_0^{-1} \mathcal{K}_r^{1/2} E_{rp0}^2, \quad (3.15)$$

where  $Z_0 = (\mu_0/\epsilon_0)^{1/2} \approx 377$  ohms is the impedance of free space. The WKB solution is valid only when the wavelength variation is small:

$$|d\lambda_r/dz| \ll 2\pi. \quad (3.16)$$

which is clearly invalid near resonance where  $|d\lambda_r/dz| \rightarrow \infty$ , and some or all of the wave power is absorbed there, depending on whether or not significant tunneling occurs.

For constant density and linear magnetic field variation, Budden (125) solved (3.10) to determine the transmitted, reflected, and absorbed power for a wave incident on the resonance zone from the high field side, obtaining

$$P_{abs}/P_{inc} = 1 - e^{-\pi\eta}, \quad (3.17)$$

$$P_{trans}/P_{inc} = e^{-\pi\eta}, \quad (3.18)$$

$$P_{refl}/P_{inc} = 0, \quad (3.19)$$

where

$$\eta = \frac{\omega_{pe}^2}{\omega c |\alpha|}. \quad (3.20)$$

Hence the wave power is either absorbed at the resonance or tunnels through to the other side, with no power reflected. Taking a typical case for which  $\alpha = 0.1 \text{ cm}^{-1}$  and  $k_0 = 0.5 \text{ cm}^{-1}$ , we find that  $\eta > 1$  corresponds to  $\omega_{pe}^2/\omega^2 > 0.2$ . Thus at 2450 MHz we expect most of the incident power will be absorbed for a density  $n_0 > 1.5 \times 10^{10} \text{ cm}^{-3}$ . Since from (2.19) and (2.20) the bulk density scales as  $n_0 \sim P_{abs}$  at low pressures and as  $n_0 \sim p^{1/2} P_{abs}$  at high pressures, we obtain the region of good power absorption sketched in Fig. 15 (112). For parameters well within this region, the incident microwave power is efficiently absorbed over the entire cross section of the resonance zone. For operation outside this region, considerable microwave power can impinge on the wafer.

The minimum  $P_{inc}$  for an ECR discharge to be sustained can similarly be found. Expanding (3.17) in the limit of  $n_0 \rightarrow 0$  yields  $P_{abs} = \pi\eta P_{inc}$ . Substituting this into (2.19), we obtain the minimum value of  $P_{inc}$  to sustain the discharge. At a given pressure, this minimum is found to be a factor of two below the  $\eta = 1$  condition for good power absorption, as illustrated in Fig. 15. We should also note that the discharge cannot be sustained if the pressure drops below some minimum value  $p_{min}$ , because the particle balance equation (2.11) has no solution for  $T_e$ . This limit is also illustrated in Fig. 15.

The size, shape, and location of the resonant zone is set by the magnet coil configuration and the magnet currents. The zone shape and location can also be modified by the Doppler effect for electrons incident on the zone. The actual resonance position is determined by the Doppler-shifted frequency (91)

$$\omega + k_r u_{res} = \omega_{ce}(z_{res}) .$$

At high densities, from (3.13),  $k_r$  can be large near the zone, leading to a large Doppler shift. For example, for  $k_r = 6.3 \text{ cm}^{-1}$  ( $\lambda_r = 1 \text{ cm}$ ), a typical value at the edge of the resonance zone, and  $u_{res} = 10^8 \text{ cm/s}$  (3 volt electron), we obtain  $k_r u_{res}/\omega \approx 0.094$ . Hence the resonant magnetic field is 910 gauss for this electron and not 875 gauss. For  $\alpha = 0.1 \text{ cm}^{-1}$ , this leads to a shift in the zone location of 0.4 cm. By using a coaxial electrostatic probe to sample the microwave field in an ECR and beating that signal against a reference signal from the incident microwaves (Fig. 16), Stevens et al. (91) have recently measured the microwave field amplitude as a function of position in an ECR source and verified that the resonant zone is Doppler shifted, in their case to  $\sim 975 \text{ G}$ , as shown in Fig. 17.

Axial and radial density and magnetic field variations can lead to wave refraction effects that alter the power flux profile as the wave propagates to the resonance zone. A density profile that is peaked on axis leads to a dielectric constant  $K_r$  that is peaked on axis. This in turn can lead to a self-focusing effect that can increase the sharpness of the microwave power profile as the wave propagates to the zone, adversely affecting uniformity. The mechanism is analogous to the use of a graded dielectric constant optical fiber to guide an optical wave. However, the ECR refraction problem is much more complicated because the density profile is not known *a priori* and the magnetized plasma medium cannot be represented as an isotropic dielectric. A simplified picture of the refraction is obtained in the geometrical optics limit by examining the trajectories of optical rays as they propagate. The ray dynamics are derivable from the dispersion equation and have a Hamiltonian form (127,128), with  $(k_z, z)$  and  $(k_\perp, r)$  canonically conjugate variable pairs. For high densities and magnetic fields ( $\omega_{pe}, \omega_{ce} \gg \omega$ ) and propagation at an angle to the magnetic field, the dispersion equation reduces to that of whistler waves (Ref. 126, p. 55):

$$kk_z/k_0^2 = \omega_{pe}^2/\omega\omega_{ce} . \quad (3.21)$$

where  $k = (k_\perp^2 + k_z^2)^{1/2}$  is the wavevector magnitude and  $k_\perp$  and  $k_z$  are the radial and axial components. Choosing  $\omega_{pe}^2/\omega_{ce}$  to have radial variation only, independent of  $z$ , Hamilton's equations show that  $k_z$  is conserved along the path of a ray (129). If  $\omega_{pe}^2/\omega_{ce}$  is a decreasing function of  $r$ , then (3.22) shows that  $k_\perp$  decreases with increasing  $r$ , implying that the ray bends toward the axis, a focusing action. On the other hand, for some parameter choices, e.g.,  $\omega_{pe} \sim \omega \sim \omega_{ce}$ , a refraction of the wave away from the axis has been found by numerical integration of the ray equations, leading, for this particular case, to an increased uniformity of the power flux profile (91).

For some source concepts (e.g., DECR in Fig. 12e), the microwave power is injected perpendicular to the magnetic field, and not parallel to the field. In this case, the feed structure excites the so-called extraordinary (X) wave, which in the WKB limit has a resonance at the upper hybrid frequency  $\omega_h = (\omega_{pe}^2 + \omega_{ce}^2)^{1/2}$ , where the wave power is absorbed (128,109). Since  $\omega_h$  depends on both  $\omega_{pe}$  and  $\omega_{ce}$ , we see that the shape and location of the resonance zone depends on the density as well as the magnetic configuration. Furthermore, the X-wave is evanescent for frequencies such that  $\omega_h < \omega < \omega_R$ , where

$$\omega_R = \frac{1}{2} [\omega_{ce} + (\omega_{ce}^2 + 4\omega_{pe}^2)^{1/2}] .$$

For a fixed driving frequency  $\omega > \omega_{ce}$ , there can be an evanescent layer that the X-wave must tunnel

through on its journey from the feed structure to the zone. For  $\omega_{pe} \gg \omega$  the tunneling is negligible and the wave cannot propagate to the zone. This can limit the density obtainable in these sources to order  $2 \times 10^{12} \text{ cm}^{-3}$  at 2450 MHz, although the limitation is not severe for typical processing applications. Microwave cavity sources (Fig. 12f) can suffer from similar limitations. On the other hand, densities as high as  $3 \times 10^{13} \text{ cm}^{-3}$  have been generated using RHP wave injection along  $B_0$  (130).

Although there are a number of commercially available ECR sources of considerable sophistication, they are generally not well characterized or understood. While the claim is sometimes made that ECR technology is complicated and expensive, we note that plasma generation is a relatively small part of the plasma processing system used in manufacturing. Other source concepts may provide a less expensive, more reliable technology for future high density processing applications and we turn to some of these now.

#### IV. HELICON DISCHARGES

Helicon generation of plasmas was first employed by Boswell (131), following a ten year history of helicon propagation studies, first in solid state and then in gaseous plasmas (132-134). Boswell and his group at the Australian National University have done the most extensive experimental studies, and Chen (86,135) has given the most complete theory of helicon propagation and absorption. Recent experiments have shed further light on mode excitation and absorption (84,85,135,136). Etching of silicon in helicon  $\text{SF}_6$  discharges was first performed by Boswell and Henry in 1985 (137), and the first helicon reactor specifically designed for materials processing was operated by Perry and Boswell in 1989 (138).

Helicons are propagating wave modes in a finite diameter, axially magnetized plasma column. The electric and magnetic fields of the modes have radial, axial, and usually, azimuthal variation, and they propagate in a low frequency, low magnetic field, high density regime characterized by

$$\omega_L \ll \omega \ll \omega_{ce} , \quad (4.1)$$

$$\omega_{pe}^2 \gg \omega \omega_{ce} , \quad (4.2)$$

where

$$\frac{1}{\omega_L^2} = \frac{1}{\omega_{pi}^2} + \frac{1}{\omega_{ce} \omega_{ci}}$$

defines the lower hybrid frequency  $\omega_L$ , with  $\omega_{pi}$  and  $\omega_{ci}$  the ion plasma frequency and ion gyrofrequency, respectively. The driving frequency is typically 1-50 MHz, with 13.56 MHz used for processing discharges. The magnetic fields vary from 50-100 G for processing discharges while fields up to 1000 G have been employed for some fundamental plasma studies. Charge densities range from  $10^{11}$ - $10^{14} \text{ cm}^{-3}$ , with  $10^{11}$ - $10^{12} \text{ cm}^{-3}$  typical for processing.

##### IV.A Helicon Configurations

Helicons are excited by an RF-driven antenna that couples to the transverse mode structure across an insulating chamber wall. The mode then propagates along the column, and the mode energy is absorbed by plasma electrons due to collisional (resistive) or collisionless (Landau) damping. All helicon applications to materials processing to date have utilized a process chamber downstream from the source. A typical helicon system is shown in Fig. 3.

The plasma potential in helicon discharges is typically low, of order 15-20 Volts, as for ECR's (139). However, the magnetic field is much lower than the 875 G required for ECR's, and the helicon power is supplied by rf rather than microwave sources. The smaller magnetic field, in particular, may provide lower cost of ownership for the helicon when compared to the ECR source. However, as we will see, the resonant coupling of the helicon mode to the antenna can lead to non-smooth variation of density with source parameters, known as "mode jumps", restricting the operating regime for a given source design.

Helicons are relatively undeveloped sources for materials processing. No sources were being used on production lines in 1992. However, several equipment vendors produce complete source systems for research and advanced development. Since close-coupled geometries have not been developed for helicons, as they have for ECR's (see Fig. 12d), the transport and diffusion of the source plasma into the process chamber is a significant issue (Sec. VIII). The process chamber can have multidipole confinement magnets to increase uniformity or can have a wafer-level magnet coil (e.g., as in Fig. 9) to keep the source plasma more tightly focused, thus increasing the etch rate with some reduction in uniformity (139).

The rf power system driving the helicon antenna can be of conventional design (as for RIE reactors). A 500–2000 W, 50 ohm, 13.56 MHz supply can be used to drive the antenna through a set of meters to measure incident and reflected power, followed by a matching network to minimize the reflected power seen by the supply. The matching network can be a  $\Pi$  design with the antenna itself as the horizontal inductive element and variable capacitors as the two legs. The antenna can also be driven through a balanced transformer so that the antenna coil is isolated from ground. This reduces the maximum antenna-plasma voltage by a factor of two, thus also reducing the undesired capacitive current coupled to the plasma by a factor of two.

#### IV.B Helicon Modes

Before we can consider helicon source design, which is mostly a matter of choosing antenna dimensions in addition to the radius and length of the source and the magnetic field profile, we must understand the helicon mode structure to which the antenna couples. Helicon modes are a superposition of low frequency whistler waves propagating at a common (fixed) angle to  $B_0$ . Hence, although helicons have a complex transverse mode structure, they have the same dispersion equation as whistlers, which is repeated here from Sec. IIC:

$$kk_z/k_0^2 = \omega_{pe}^2/\omega\omega_{ce} \quad (4.3)$$

where

$$k = (k_\perp^2 + k_z^2)^{1/2} \quad (4.4)$$

is the wavevector magnitude,  $k_\perp$  and  $k_z$  are the radial and axial components, and  $k_0 = \omega/c$ . The helicon modes are mixtures of electromagnetic ( $\nabla \cdot \mathbf{E} \approx 0$ ) and quasistatic ( $\nabla \times \mathbf{E} \approx 0$ ) fields having the form

$$\vec{\mathbf{E}}, \vec{\mathbf{H}} \sim \exp j(\omega t - k_z z - m\theta) \quad ,$$

where here the integer  $m$  specifies the azimuthal mode. For an insulating (or conducting) wall at  $r = R$  and assuming a uniform plasma density, the boundary condition on the total radial current density amplitude  $\vec{J}_r = 0$  (or  $\vec{E}_\theta = 0$ ) leads to

$$mkJ_m(k_\perp R) + k_z J_m'(k_\perp R) = 0 \quad , \quad (4.5)$$

where the prime denotes a derivative of the Bessel function,  $J_m$ , with respect to its argument. For a given frequency  $\omega$ , density  $n_0$ , and magnetic field  $B_0$ , (4.3)–(4.5) can be solved to obtain  $k_\perp$ ,  $k_z$ , and  $k$ .

Helicon sources based on excitation of the  $m = 0$  mode and the  $m = 1$  mode have been developed. Since the  $m = 0$  mode is axisymmetric and the  $m = 1$  mode has a helical variation, both modes generate time-averaged, axisymmetric field intensities. The transverse electric field patterns and the way these propagate along  $z$  are shown in Fig. 18a for the  $m = 0$  mode and in Fig. 18b for the  $m = 1$  mode (86,135). Undamped helicon modes have  $\vec{E}_z = 0$ , i.e., the quasistatic and electromagnetic components of  $\vec{E}_z$  exactly cancel. The antenna couples to the transverse electric or magnetic fields to excite the modes.

Equation (4.5) can be solved for  $k_\perp R$  as a function of  $k_z/k$ . There are an infinite number of solutions corresponding to different radial field variations and in any real system a mixture of modes is very likely excited. For simplicity, let us consider the first radial mode, shown in Fig. 18. For  $m = 0$ , we find

$$k_{\perp}R = 3.83 \quad (m = 0)$$

for any  $k_z/k$ . For  $m = 1$ , we solve numerically to obtain the graph shown in Fig. 19, with the limiting values

$$k_{\perp}R = 3.83 \quad (m = 1, k_{\perp} \gg k_z),$$

$$k_{\perp}R = 2.41 \quad (m = 1, k_z \gg k_{\perp}).$$

To design an antenna for efficient power coupling, we must solve (4.3)-(4.5) and determine  $k_{\perp}$  and  $k_z$ . For two limiting regimes this can be done analytically:

- (a) Low density with  $k_{\perp} \gg k_z$ ,
- (b) High density with  $k_z \gg k_{\perp}$ .

Rewriting (4.3) in more physical terms:

$$kk_z = \frac{e\mu_0 n_0 \omega}{B_0}. \quad (4.6)$$

Let us estimate the condition  $n = n_0^*$  for  $k_z = k_{\perp}$  for the  $m = 1$  mode. We have  $k_z = k_{\perp} \approx 2.9/R$  from Fig. 19, and  $k = \sqrt{2} k_z$ . Choosing typical processing source parameters of  $R = 5$  cm,  $f = 13.56$  MHz, and  $B_0 = 200$  G, we obtain  $n_0^* \approx 5.4 \times 10^{12}$  cm<sup>-3</sup>. Hence for this source with  $n_0 \ll n_0^*$ , we have  $k_{\perp} \gg k_z$  and, from (4.4),  $k \approx k_{\perp}$ . For this case, (4.6) yields the axial wavelength of the helicon mode for low density operation:

$$\lambda_z = \frac{2\pi}{k_z} = \frac{3.83}{R} \frac{B_0}{e\mu_0 n_0 f}. \quad (4.7)$$

This regime is of limited interest for materials processing because, setting the antenna length  $\ell \sim \lambda_z$  (see Sec. IV.C), requires  $R \ll \ell < L$ . Hence, the source would be long and thin and uniformity over a large area would be compromised.

For  $n_0 \gg n_0^*$ , we have  $k_z \gg k_{\perp}$  and  $k \approx k_z$ . In this high density regime, we find

$$\lambda_z = \left[ \frac{2\pi B_0}{e\mu_0 n_0 f} \right]^{1/2}. \quad (4.8)$$

This regime is of marginal interest because it requires  $\ell \ll R$ , a short fat antenna, which leads to inefficient coupling of power from the antenna to the plasma because, for a given current, only a small axial voltage is induced, leading to a small axial charge separation to drive the helicon mode. The regime of most interest for materials processing sources is  $n_0 \sim n_0^*$ , for which  $k_z \sim k_{\perp}$ ; hence, we have  $R \sim \ell \sim L$ , yielding a low profile source configuration. This regime is not easy to analyze. For  $m = 1$ , the solution must be found numerically. One usually chooses  $k_{\perp}$  somewhat larger than  $k_z$ ; hence we use (4.7) for simple estimates of source operation (84,86). Komori et al. have measured the helicon wave magnetic field using a magnetic pick-up coil (140,141) and circuit similar to that used by Stevens et al. (91) for measuring the microwave electric field (Fig. 16). The dependence of  $\lambda_z$  on  $B_0/n_0$  shown in Fig. 20 roughly follows (4.7).

Recall from Sec. II.A.3 that the bulk density  $n_0$  is determined by the absorbed power  $P_{abr}$  and the pressure  $p$  as specified in (2.19) and (2.20). Once  $B_0$ ,  $f$ , and  $R$  (for low density) are chosen, then (4.7) or (4.8) determine  $\lambda_z$ . Ideally, the antenna must be designed to excite modes having that particular  $\lambda_z$ . At first sight, this seems to limit source operation to one particular density unless  $B_0$  or  $f$  can be conveniently varied. Fortunately, antennas excite a range of  $\lambda_z$ 's, thus allowing source operation over a range of  $n_0$ 's.

#### IV.C Antenna Coupling

A typical antenna used to excite the  $m = 1$  mode is shown in Fig. 21. Other antennas are described by Chen (135). Looking at the  $x-y$  transverse coordinates shown in the figure, we see that this antenna generates a  $\vec{B}_x$  field over an axial antenna length  $\ell$ , which can couple to the transverse magnetic field of the helicon mode. The antenna also induces a current within the plasma column just beneath each horizontal wire, in a direction opposite to the currents shown. This current produces charge of opposite signs at the two ends of the antenna, which in turn generates a transverse quasistatic field,  $\vec{E}_y$ , which can couple to the transverse quasistatic fields of the helicon mode (see Fig. 18b). The conditions for which each form of coupling dominates are not well understood.

To illustrate the wavelength matching condition for helicon excitation, we consider an ideal antenna field for quasistatic coupling

$$\vec{E}_y(z) \sim \vec{E}_{y0} [\delta(z + \ell/2) - \delta(z - \ell/2)] , \quad (4.9)$$

where  $\delta$  is the Dirac delta function. This ideal field is sharply peaked near the two antenna ends, as shown schematically in Fig. 22a. Taking the Fourier transform,

$$E_y(k_z) = \vec{E}_{y0} \int_{-\infty}^{\infty} dz \vec{E}_y(z) \exp(-jk_z z) ,$$

and squaring this to obtain the spatial power spectrum of the antenna, we obtain

$$E_y^2(k_z) = 4\vec{E}_{y0}^2 \sin^2 \frac{k_z \ell}{2} , \quad (4.10)$$

which is plotted in Fig. 22b. We see that the antenna couples well to the helicon mode for  $k_z \approx \pi/\ell, 3\pi/\ell$ , etc, corresponding to  $\lambda_z \approx 2\ell, 2\ell/3$ , etc. The coupling is poor for  $k_z \approx 0, 2\pi/\ell, 4\pi/\ell$ , etc, corresponding to  $\lambda_z \rightarrow \infty, \lambda_z \approx \ell, \lambda_z \approx \ell/2$ , etc.

Figure 23 (139) shows the effect of the antenna coupling on the density  $n_0$  as the power  $P_{inc}$  supplied to the antenna is increased, based on a 36 GHz microwave interferometer measurement of  $n_0$ . For  $P_{inc} < 350$  W,  $n_0$  determined from power balance (2.19) is low, leading to  $k_z \ll \pi/\ell$  and, from (4.10), poor coupling to the helicon mode. The discharge in this regime is probably capacitively driven, with a relatively high antenna voltage ( $\sim 2$  kV) and plasma potential ( $> 30$  V). The transition to helicon mode operation with  $k_z \approx \pi/\ell \approx 0.4 k_{\perp}$  for  $P_{inc} \approx 400-750$  W and  $n_0 \approx 1.4 \times 10^{11} \text{ cm}^{-3}$  is clearly seen. A second transition is seen to  $k_z \approx 3\pi/\ell = k_{\perp}$  with  $n_0 \approx 2.7 \times 10^{11} \text{ cm}^{-3}$ . Since  $k_z \sim k_{\perp}$  for the second transition, the observed increase in  $n_0$  lies between the factors of 3 predicted from (4.7) and  $\sqrt{3}$  predicted from (4.8). Standing helicon wave effects may also play a role in this transition (139), as described in Sec. IV.D. Figure 24 (142) shows the roughly linear scaling of  $n_0$  with  $B_0$  predicted from (4.7) or (4.8), for a different source than that of Fig. 23. Again we see the density steps imposed by the antenna coupling condition. Depending on the specific experimental configuration, for example the distance between the antenna and the outer surface of the source dielectric cylinder, the density steps are not always as evident as shown in these data (143). They may also be produced by large relaxation oscillations as the discharge "hunts" between helicon and inductive excitation modes (83). The antenna can also be designed to couple efficiently to a wide range of  $k_z$ 's, reducing the importance of mode jumps in the density range of interest.

Similar effects can be expected for  $m = 0$  mode helicons. This mode can be excited by an antenna consisting of two circular coils of radius  $R$ , separated by a length  $\ell$ , carrying oppositely directed currents.

#### IV.D Helicon Mode Absorption

The helicon mode energy is believed to be transferred to the plasma electrons as the mode propagates along the column by collisional or collisionless (Landau) damping. The former mechanism transfers the energy to the thermal (bulk) electron population, while the latter mechanism can act to preferentially heat a

non-thermal electron population to energies greatly exceeding the bulk electron temperature. There is considerable evidence (86,135,142) that collisional absorption is too weak to account for energy deposition at low pressures (< 10 mTorr argon), although this mechanism may dominate at higher pressures. Landau damping is a process by which a wave transfers energy to electrons having velocities near the phase velocity  $u_{ph} = \omega/k_z$  of the wave. Chen (86) has estimated the effective collision frequency  $\nu_{LD}$  for Landau damping of the helicon mode as

$$\nu_{LD} \approx 2\sqrt{\pi} \omega \zeta^3 \exp(-\zeta^2), \quad \zeta \gg 1, \quad (4.11)$$

$$\nu_{LD}(\max) \approx 1.45 \omega, \quad (4.12)$$

where  $\zeta = \omega/(k_z u_{Te})$ , with  $u_{Te} = (2eT_e/m)^{1/2}$  the electron thermal velocity. From (4.7) or (4.8) we see that for  $\zeta \gg 1$ ,  $\nu_{LD}$  increases with increasing electron density at constant magnetic field. However, in typical helicon sources where  $\zeta$  may be less than or order unity,  $\nu_{LD}$  can decrease with increasing  $n$ . The total effective collision frequency can be written as

$$\nu_T = \nu_{eT} + \nu_{LD},$$

where  $\nu_{eT}$  is the sum of the electron-neutral and electron-ion collision rates. The axial decay length  $\alpha_z^{-1}$  for helicon mode damping is

$$\alpha_z^{-1} \approx \frac{\omega_{ce}}{k_{\perp} \nu_T} \quad (4.13)$$

for low density ( $k_{\perp} \gg k_z$ ) and

$$\alpha_z^{-1} \approx \frac{2\omega_{ce}}{k_z \nu_T} \quad (4.14)$$

for high density ( $k_z \gg k_{\perp}$ ). For efficient power transfer to the plasma electrons, we require that  $\alpha_z^{-1} \leq L$ , where  $L$  is the helicon chamber source length. However, if this condition is not satisfied, then power may still be efficiently absorbed by means of helicon standing waves along the source (length  $L$ ), or source and process chambers (total length  $L_T$ ), leading to additional resonant absorption effects when  $\lambda_z \sim 2L$  or  $\lambda_z \sim 2L_T$  (139,142,144).

By choosing the antenna length  $\ell$  such that  $k_z \approx \pi/\ell$ , it is possible to heat electrons, by Landau damping, whose energies are near that corresponding to the wave phase velocity

$$e\mathcal{E} = \frac{1}{2}m(\omega/k_z)^2. \quad (4.14)$$

If  $\mathcal{E}$  is chosen near the peak of the ionization cross section ( $\sim 50$  volts in argon), then the collisional energy  $\mathcal{E}_e$  lost per electron-ion pair created can be reduced to a low value, of order the ionization energy  $\mathcal{E}_{ie}$ . It follows from (2.19) that this can lead to a significant increase in density for the same absorbed power. However, the effective collision frequency  $\nu_{LD}$  falls precipitously for  $\omega/k_z \gg u_{Te}$ , leading to a low spatial decay rate and requiring  $L \gg R$ , of limited interest for materials processing sources having  $L \sim R$ . Also, there is some experimental evidence (145) that, if the antenna is designed to excite superthermal electrons ( $\zeta \gg 1$ ), then  $k_z$  adjust itself as the wave propagates away from the antenna so as to excite thermal electrons ( $\zeta \approx 1$ ) downstream of the antenna. Hence, it may not be easy to achieve excitation of superthermal electrons. Evidence of Landau damping has been reported by Komori et al. (84) and Lowenhardt et al. (85), but other absorption mechanisms, such as nonlinear excitation of plasma instabilities, may also play a role in helicon mode energy transfer (142).

In principle, the radial power deposition is different for the  $m = 0$  and  $m = 1$  modes. The  $m = 0$  mode deposits its energy preferentially on the axis, while the  $m = 1$  mode has a maximum power deposition at  $r = 0.48 R$  (86,135,146).

As an example of helicon design, let  $R = 5$  cm,  $L = 20$  cm,  $N = 3.3 \times 10^{13}$  cm<sup>-3</sup> (1 mTorr),  $\omega = 85 \times 10^6$  s<sup>-1</sup> (13.6 MHz), and  $P_{abr} = 300$  watts. At 1 mTorr,  $\lambda_i = 3$  cm. Then from (2.8) and (2.9)  $h_L = h_R = 0.33$ , and from (2.12),  $d_{eff} = 6.1$  cm. For argon we then obtain from Fig. 7 that  $T_e = 5.2$  V, and from Fig. 5, that  $\mathcal{E}_e = 39$  V. Using (2.2), we find  $\mathcal{E}_L = 76$  V. The Bohm velocity is  $u_B = 3.5 \times 10^5$  cm/s, and from (2.20),  $A_{eff} = 52$  cm<sup>2</sup>. Then from (2.19), we obtain  $n_0 = 2.7 \times 10^{12}$  cm<sup>-3</sup>. We see that  $n_0 < n_0^*$  at  $B_0 = 200$  G. From (4.7), we find  $\lambda_z = 20.8$  cm, and hence we choose an antenna length  $\ell = \lambda_z/2 = 10.4$  cm to optimize power coupling. We note that  $\omega/k_z = 2.8 \times 10^8$  m/s, compared with the electron thermal velocity  $u_{Te} = 1.4 \times 10^8$  cm/s. Hence,  $\zeta = 2$ , not far from the peak of the Landau damping rate for thermal electrons.

## V. INDUCTIVE DISCHARGES

Inductive discharges are nearly as old as the invention of electric power, with the first report of an "electrodeless ring discharge" by Hittorf in 1884 (147). He wrapped a coil around an evacuated tube and observed a discharge when the coil was excited with a Leyden jar. A subsequent fifty year controversy developed (148,149) as to whether these discharges were capacitively driven by plasma coupling to the low and high voltage ends of the cylindrical coil, as in an RF diode, or were driven by the induced electric field inside the coil. This issue was resolved with the recognition that the discharge was capacitively driven at low plasma densities, with a transition to an inductive mode of operation at high densities (150). Succeeding developments, which focused on pressures exceeding 20 mTorr in a cylindrical coil geometry, are described in a review article by Eckert (151). The high pressure regime was intensively developed in the 1970's with the invention of the open air induction torch and its use for spectroscopy. In the late 1980's, the planar coil configuration was developed (152,153), renewing interest in the use of high density inductive discharges for materials processing at low pressures (< 50 mTorr). It is this regime that is the primary focus here.

### V.A Inductive Source Configurations

The two exciting coil configurations, cylindrical and planar, are shown in Fig. 25 for a low profile source. The planar coil is a flat helix wound from near the axis to near the outer radius of the source chamber ("electric stovetop" coil shape). Planar and cylindrical coils can also be united to give "cylindrical cap" or "hemispherical" coil shapes. Multipoles can be used around the process chamber circumference to increase radial plasma uniformity, as shown. The planar coil can also be moved close to the wafer surface, resulting in a close-coupled or planar source geometry ( $L \leq R$ ) having good uniformity properties even in the absence of multidipole confinement (153). In the close-coupled configuration, the coil can be wound nonuniformly or driven with radially varying currents to control the radial plasma uniformity.

Similar to helicon antennas, inductive coils can be driven by a 13.56 MHz, 50 ohm rf supply through a  $\Pi$  matching network. The coil can be driven push-pull using a balanced transformer, which places a virtual ground in the middle of the coil and reduces the maximum coil-to-plasma voltage by a factor of two. This reduces the undesired capacitively coupled rf current flowing from coil to plasma by a factor of two. An electrostatic shield placed between the coil and the plasma can further reduce the capacitive coupling if desired, while allowing the inductive field to couple unhindered to the plasma.

Plasma in an inductive source is created by application of rf power to a non-resonant, inductive coil, resulting in the breakdown of the process gas within or near the coil by the induced rf electric field. The plasma potential in these discharges is typically less than 30-40 volts (153). Multidipole confinement can even further reduce these potentials. The plasma created in the source region streams toward a wafer holder that can be independently biased by application of rf power using a separate generator. Inductive sources have potential advantages over other high density sources, including simplicity of concept, no requirement for dc magnetic fields (as required for ECR's and helicons), rf rather than microwave source power, and non-resonant source operation, which can enable efficient power absorption over a wide range of source parameters.

In contrast to ECR's and helicons, which can be configured to achieve densities  $n_0 \geq 10^{13}$  cm<sup>-3</sup>, we will see (Sec. V.D) that inductive sources have natural density limits,  $n_0 \leq 10^{13}$  cm<sup>-3</sup>, for efficient power

transfer to the plasma. However, the density regime  $10^{11} \leq n_0 \leq 10^{13} \text{ cm}^{-3}$  for efficient inductive source operation, as much as a factor of 100 times higher than for rf diodes, is of considerable interest for low pressure processing.

Inductive sources for materials processing applications are in their infancy. The first commercially available system, the so-called TCP (transformer coupled plasma), was announced in Summer, 1992 (153). Other vendors are beta-testing similar products for release in 1992 or 1993.

### V.B Power Absorption and Operating Regimes

In the inductively coupled plasma, power is transferred from the electric fields to the plasma electrons by collisional (ohmic) dissipation. At very low pressures ( $< 1 \text{ mTorr}$ ; electron mean free path  $\geq R, L$ ), a collisionless heating process may also act, in which bulk plasma electrons "collide" with the oscillating, inductive fields and may be accelerated and thermalized in the absence of collisions much like the stochastic heating near capacitive rf sheaths we discussed in Sec. II.B. Here, we concentrate on the ohmic heating process.

The spatial decay constant  $\alpha_z$  for an electromagnetic wave incident on a uniform density plasma along  $\hat{z}$  is

$$\alpha_z = \text{Re} \left[ \frac{\omega}{c} \kappa_p^{1/2} \right], \quad (5.1)$$

where

$$\kappa_p = 1 - \frac{\omega_{pe}^2}{\omega(\omega - j\nu_c)} = - \frac{\omega_{pe}^2}{\omega^2(1 - j\nu_c/\omega)} \quad (5.2)$$

is the relative plasma (Lorentz) dielectric constant, valid in the absence of a magnetic field (compare to  $\kappa_r$  in (3.11)), and  $\nu_c$  is the electron-neutral collision frequency. For  $\nu_c \ll \omega$ , we obtain

$$\alpha_z = \frac{\omega_{pe}}{c} = \frac{1}{\delta_p}, \quad (5.3)$$

where  $\delta_p$  is the collisionless skin depth:

$$\delta_p = \left[ \frac{m}{e^2 \mu_0 n_0} \right]^{1/2}. \quad (5.4)$$

For  $\nu_c \gg \omega$ , we obtain

$$\alpha_z = \frac{1}{\sqrt{2}} \frac{\omega_{pe}}{c} \left[ \frac{\omega}{\nu_c} \right]^{1/2} = \frac{1}{\delta_c}, \quad (5.5)$$

where  $\delta_c$  is the collisional skin depth:

$$\delta_c = \left[ \frac{2}{\omega \mu_0 \sigma} \right]^{1/2}, \quad (5.6)$$

where

$$\sigma = \frac{e^2 n_0}{m v_c} \quad (5.7)$$

is the dc conductivity of the plasma. We therefore distinguish two pressure regimes:

- (a) low pressure,  $v_c \ll \omega$ , skin depth  $\delta_p$ ;
- (b) high pressure,  $v_c \gg \omega$ , skin depth  $\delta_c$ .

For each pressure regime, we also distinguish two density regimes:

- (a) high density,  $\delta \ll R, L$ ;
- (b) low density,  $\delta \gg R, L$ .

At 13.56 MHz in argon, we find  $v_c = \omega$  for  $p^* \approx 25$  mTorr. Let us consider the low pressure regime (a) with  $p \ll p^*$ . For a cylindrical coil with  $R \approx 10$  cm, or for a planar coil with  $L = 10$  cm, we find from (5.4) that  $\delta_p = R, L$  for  $n_0^* \approx 3 \times 10^9$  cm<sup>-3</sup>. Hence, for a typical low pressure processing discharge with  $n_0 \geq 3 \times 10^{10}$  cm<sup>-3</sup>, we have  $v_c \ll \omega$  and  $\delta_p \ll R, L$  as the regime of operation. We briefly discuss the  $v_c \ll \omega$  and  $\delta_p \gg R, L$  regime in Sec. V.D when we consider the minimum current and power necessary to generate an inductively coupled plasma.

### V.C Source Operation and Coupling

Although most systems are operated with planar coils (see Fig. 25b), finite geometry effects make these configurations difficult to analyze. To illustrate the general principles of inductive source operation, we concentrate on the cylindrical source (Fig. 25a) in the long thin geometry  $L \gg R$ . We take the source coil to have  $\eta$  turns at radius  $b > R$ . For ohmic heating in the plasma skin,

$$P_{abs} = \frac{1}{2} \frac{J^2}{\sigma} 2\pi R L \delta_p, \quad (5.8)$$

where  $J$  is the RF induced current density in the skin near  $r = R$  (opposite in direction to the applied current in the coil). Letting  $I_p = J L \delta_p$  be the total induced RF current and defining the plasma resistance through  $P_{abs} = \frac{1}{2} I_p^2 R_p$ , we obtain

$$R_p = \frac{2\pi R}{\sigma L \delta_p}. \quad (5.9)$$

The plasma inductance  $L_p$  is found using  $\Phi = L_p I_p$ , where  $\Phi$  is the total magnetic flux linked by the skin current. Using  $\Phi = \mu_0 \pi R^2 H_z$ , where  $H_z = J \delta_p$  is the magnetic field produced by the skin current, we obtain

$$L_p = \frac{\mu_0 \pi R^2}{L}. \quad (5.10)$$

Letting the coil have  $\eta$  turns at a radius  $b \geq R$ , where  $b - R$  is the "thickness" of the dielectric interface separating coil and plasma, then we can model the source as the TCP shown in Fig. 26. Evaluating the inductance matrix for this transformer, defined through (154, p. 27)

$$V_{rf} = j\omega L_{11} I_{rf} + j\omega L_{12} I_p, \quad (5.11)$$

$$V_p = j\omega L_{21} I_{rf} + j\omega L_{22} I_p, \quad (5.12)$$

we obtain

$$L_{11} = \frac{\mu_0 \pi b^2 \eta^2}{L}, \quad (5.13)$$

$$L_{12} = L_{21} = \frac{\mu_0 \pi R^2 \eta}{L}, \quad (5.14)$$

$$L_{22} = L_p = \frac{\mu_0 \pi R^2}{L}. \quad (5.15)$$

Using  $V_p = -I_p R_p$  (see Fig. 26) in (5.12) and inserting into (5.11), we can solve for the impedance seen at the coil terminals:

$$Z_s = \frac{V_{rf}}{I_{rf}} = j\omega L_{11} + \frac{\omega^2 L_{12}^2}{R_p + j\omega L_p}. \quad (5.16)$$

For  $\delta_p \ll R$ , it can easily be seen that  $R_p \ll \omega L_p$ . Hence expanding the denominator in (5.16), we obtain

$$L_s = \frac{\mu_0 \pi R^2 \eta^2}{L} \left[ \frac{b^2}{R^2} - 1 \right], \quad (5.17)$$

$$R_s = \eta^2 \frac{2\pi R}{\sigma L \delta_p}, \quad (5.18)$$

where  $Z_s = R_s + j\omega L_s$ . The power balance

$$P_{abs} = \frac{1}{2} I_{rf}^2 R_s \quad (5.19)$$

then yields the required rf source current, and the rf voltage is determined from

$$V_{rf} = I_{rf} Z_s. \quad (5.20)$$

As an example, let  $R = 5$  cm,  $b = 6$  cm,  $L = 20$  cm,  $\eta = 5$  turns,  $N = 3.3 \times 10^{13}$  cm<sup>-3</sup> (1 mTorr, 298K),  $\omega = 85 \times 10^6$  s<sup>-1</sup> (13.6 MHz), and  $P_{abs} = 300$  watts. At 1 mTorr,  $\lambda_i \approx 3$  cm. Then from (2.8) and (2.9)  $h_L = h_R \approx 0.33$ , and from (2.12),  $d_{eff} \approx 6.1$  cm. For argon we then obtain from Fig. 7 that  $T_e \approx 5.2$  V, and from Fig. 5, that  $\mathcal{E}_c \approx 39$  V. Using (2.2), we find  $\mathcal{E}_L \approx 76$  V. The Bohm velocity is  $u_B \approx 3.5 \times 10^5$  cm/s, and from (2.20),  $A_{eff} \approx 52$  cm<sup>2</sup>. Then from (2.19), we obtain  $n_0 \approx 2.7 \times 10^{12}$  cm<sup>-3</sup>. Estimating  $v_c$  for argon from Fig. 4, we find  $v_c \approx 4.3 \times 10^6$  s<sup>-1</sup>, and, from (5.7),  $\sigma \approx 1.8 \times 10^4$  mho/m. Using (5.4), we obtain  $\delta_p \approx 3.2$  mm. Evaluating (5.17) and (5.18), we find  $R_s \approx 0.68$  ohms and  $L_s \approx 0.63$   $\mu$ H, such that  $\omega L_s \approx 50$  ohms. Equations (5.19) and (5.20) then yield  $I_{rf} \approx 30$  A and  $V_{rf} \approx 1500$  V. The high inductive voltage required for this five turn source can be supplied from a 50 ohm RF power source through a capacitive matching network.

#### V.D Low Density Operation and Source Efficiency

Since the dc conductivity  $\sigma \propto n_0$ , and  $\delta_p \propto n_0^{-1/2}$ , it is apparent from (5.18) and (5.19) that at fixed driving current  $I_{rf}$ , we have the scaling

$$P_{abs} \propto n_0^{-1/2}. \quad (5.21)$$

However, at low densities, such that  $\delta_p \gg R$ , the conductivity is low and the fields fully penetrate the plasma. In this case, applying Faraday's law to determine the induced electric field,  $E_\theta$  within the coil, we obtain

$$E_{\theta}(r) = \frac{1}{2} j \omega r \mu_0 \eta I_{rf} / L ,$$

and, writing  $J = j \omega \epsilon_0 K_p E$  for  $v_e \ll \omega$ , we have  $J \propto n_0 r I_{rf}$ . Evaluating the power absorbed for this case,

$$P_{abs} = \frac{1}{2} \int_0^R \frac{J^2(r)}{\sigma} 2\pi r L dr$$

yields

$$P_{abs} \propto n_0 \tag{5.22}$$

in this low density regime. Comparing (5.21) and (5.22), we see that for fixed  $I_{rf}$ ,  $P_{abs}$  versus  $n_0$  must have a maximum near  $\delta_p \sim R$ , as sketched in Fig. 27 for several different values of  $I_{rf}$ . Now consider the power balance requirement (2.19), which is plotted as the straight line in the figure. The intersection of the line with the curves defines the equilibrium point for discharge operation. We see that inductive source operation is impossible if the source current  $I_{rf}$  is below some minimum value  $I_{min}$ . In this regime, any discharge must be capacitive. The required  $I_{min}$  is similar to the required minimum value of  $P_{inc}$  to sustain an ECR discharges, as shown in Fig. 15.

Let us note that the driving coil (primary of the transformer shown in Fig. 26) has some resistance  $R_{coil}$ . Hence, even if the discharge is extinguished ( $n_0 = 0$ ), there is a minimum power  $P_{inc} = \frac{1}{2} I_{min}^2 R_{coil}$  supplied by the source before the inductive discharge can form.

Because  $P_{abs} \propto n_0^{-1/2}$  at high densities, we see from Fig. 27 that the power transfer efficiency  $P_{abs}/P_{inc}$  falls continually as  $n_0$  is increased, hence limiting source operation at very high densities because of power supply limitations. As pointed out by Piejak et al. (107), the poor power transfer to the plasma at very low and at very high densities is analogous to the well known property of an ordinary transformer with an open and a shorted secondary winding. In both cases no power is dissipated in the load (here the plasma), but in both cases there is power dissipated in the primary winding (here the coil) due to its inherent resistance. Piejak et al. (107) have given a complete analysis of an inductive discharge in the high pressure regime in terms of measurable source voltages and currents based on this analogy.

We see that  $\delta_p \sim R$  is the preferred operating regime for maximum power efficiency in the low pressure regime. In fact, at high pressure, Thomson (148) obtained the similar condition  $\delta_c \approx 0.57 R$  for maximum power efficiency in a uniform density source.

Other issues of inductive source operation include finite geometry effects ( $L \sim R$ ), planar coil source operation, collisionless heating at very low pressures, capacitive operating mode and startup, and self-resonant coil effects due to stray coil capacitances. Some of these issues are addressed in the literature (107,151,155,156).

## VI. HELICAL RESONATOR DISCHARGES

While helical resonators have long been used as electronic circuit elements (157), they have only recently been used for efficient plasma generation at pressures as low as  $10^{-5}$  Torr. High pressure discharges ( $\sim 1$  Torr) were first applied by Steinberg and Steinberg (158) and used for downstream stripping. The concept was further refined and applied to low pressures discharges (0.1-1 mTorr) by Flamm et al. (159) and was used by Flamm (160) and by Cook et al. (18,161) for polysilicon gate etching and for downstream deposition of silicon dioxide and silicon nitride films.

Helical resonator plasmas operate at radio frequencies (3-30 MHz) with simple hardware, do not require a dc magnetic field (as for ECR's and helicons), and exhibit high  $Q$  (600-1500 typically without the plasma present) and high characteristic impedance ( $Z_0$ ). These resonators are slow wave structures, supporting an electromagnetic wave propagating along the  $z$  axis with phase velocity  $u_{ph} \ll c$ . As shown in Fig. 28, the source consists of a coil surrounded by a grounded coaxial cylinder. The composite structure becomes

resonant when an integral number of quarter waves of the rf field fit between the two ends. When this condition is satisfied, the intense electromagnetic fields within the helix can sustain a plasma with negligible matching loss at low gas pressure.

As with inductive discharges, which they resemble, helical resonator discharges can be operated in two regimes:

- (a) Capacitive coupling, low power, low density and high plasma potential
- (b) Inductive coupling, high power, high density and low plasma potential

In the capacitive regime, the discharge is driven by rf current flowing through the plasma from the high voltage to the low voltage end of the coil, and energy transfer to the plasma electrons is through the  $\vec{E}_r$  and  $\vec{E}_z$  fields. This regime is similar to that of an rf diode.

The inductive regime is of major interest for high density plasma assisted materials processing. To force operation in this regime, an electrostatic shield can be added between the helix and the plasma column to reduce the capacitive coupling to a negligible value. The shield is typically a metal cylinder slotted along  $z$  that allows the inductive field  $\vec{E}_\theta$  to penetrate into the plasma, while shorting out the capacitive  $\vec{E}_r$  and  $\vec{E}_z$  fields.

There have been few fundamental studies of helical resonator discharges (162,163). There is one commercial manufacturer (164) of sources for research and advanced development applications. Sources as large as 25 cm in diameter are available, driven by up to 5 kW of rf power at 13.56 MHz and producing plasmas with densities (in Ar) exceeding  $2 \times 10^{12} \text{ cm}^{-3}$ .

The basic design parameters for a helical resonator discharge consist of pressure, RF power, source length, plasma radius, helix radius, outer cylinder radius, winding pitch angle, and excitation frequency. This is a complicated system that is not well understood. A first step is to determine the helical slow-wave modes and their interaction with the plasma. This has not been done for an electrostatically shielded discharge, so we illustrate the approach for an unshielded plasma column. The dispersion equation  $k_z$  versus  $\omega$ , and the relationship among the field quantities, can be found in the approximation of a uniform, collisionless ( $\omega \gg \nu_c$ ) plasma having relative dielectric constant  $K_p = 1 - \omega_{pe}^2/\omega^2$  [See (5.2)] by using a "developed sheath helix" model, in which the rf current in the helical wires is replaced by a continuous current sheet ("sheath") and the cylindrical  $(r, \theta, z)$  geometry is unfolded into a rectangular  $(x, y, z)$  geometry ("developed"). This is a standard analytical technique for treating helical systems (165) that retains most essential physics. The details of the calculation are given in Lieberman et al. (162). In the absence of the plasma, it can be shown that there is a single mode that tends to propagate along the helical wire, as expected for this two-conductor transmission line system.<sup>3</sup> For typical source parameters,  $R=3$  cm,  $b=5$  cm,  $c=10$  cm,  $L=30$  cm, and  $\psi=0.1$  radians, where the parameters are defined in Fig. 28, we determine the propagation at low plasma density  $n_0 = 10^9 \text{ cm}^{-3}$ , at high density  $n_0 = 10^{11} \text{ cm}^{-3}$ , and without plasma  $n_0 = 0$ . Figure 29 gives  $k_z$  versus  $f=\omega/2\pi$  with  $n_0$  as a parameter. For comparison, the upper line shows a wave following the geometrical helix pitch,

$$k_{zh} = \frac{\omega}{c \tan \psi} \quad (6.1)$$

and the lower line shows a light wave  $k_{z0} = \omega/c$ . Without a plasma, there is only one mode of propagation, with  $k_z$  somewhat smaller than  $k_{zh}$ ; ie, the wave velocity  $\omega/k_z$  is somewhat larger than  $c \tan \psi$ . As  $n_0$  increases, the wave speeds up, and as  $n_0 \rightarrow \infty$ ,  $\omega/k_z \rightarrow c$ . For this "coax" mode, at large  $n_0$ , the plasma is at a high voltage with respect to the outer cylinder.

<sup>3</sup> This is analogous to wave propagation in a coaxial line, with the helical coil being the inner conductor and the grounded cylinder being the outer conductor.

A second "helix" mode appears when  $n_0$  is such that  $\omega_{pe} > \omega$ , a condition that is always met for typical discharge operation. Hence, both modes coexist during typical operation. The wave velocity for the second mode is always smaller than the helix velocity  $c \tan \psi$ . The mode appears as a resonance  $k_z \rightarrow \infty$  at  $n_0$  such that  $\omega_{pe} = \omega$ , and the wave slows down as  $n_0$  increases. For the helix mode at large  $n_0$ , the plasma and outer cylinder are at nearly the same voltage, and the helix is at a high voltage with respect to them both. We expect to see two modes in the high density limit because the plasma acts like a conducting cylinder; hence we have a three conductor transmission line system in this limit.

At high densities, the axial wavenumbers for the two modes are very different. For example, at  $n_0 = 10^{11} \text{ cm}^{-3}$ ,  $k_z(\text{coax}) \approx 0.5 \text{ m}^{-1}$  and  $k_z(\text{helix}) \approx 5.5 \text{ m}^{-1}$ . Since the source length  $L$  is chosen to be roughly a quarter wavelength at the helix geometrical pitch,  $k_{zh}L \approx \pi/2$ , the coax mode is not resonantly excited [ $k_z(\text{coax}) \ll k_{zh}$ ]. However, this mode does play a role in source operation at start-up. During typical source operation, only the helix mode is resonant, and it dominates the source operation.

As an example, for  $L = 30 \text{ cm}$  and  $k_zL = \pi/2$ , we obtain  $k_z = 5.2 \text{ m}^{-1}$ . Then from (6.1), we estimate the resonant frequency  $f \approx 25 \text{ MHz}$  at high densities. Other methods for estimating the frequency are also available (166). In particular, end effects can change the resonant frequency due to additional capacitive coupling.

Once the resonant frequency for quarter wavelength operation is determined, then the fields within all regions inside the helical resonator can be found. The characteristic impedance of the helical transmission line can then be found:

$$Z_0 = \frac{1}{3} \tilde{\zeta} \left( \frac{\mu_0}{\epsilon_0} \right)^{1/2} \frac{\eta b}{L}, \quad (6.2)$$

where  $\eta$  is the number of helical turns, and  $\tilde{\zeta}$  is a geometrical factor of order unity. Typically,  $Z_0 \sim 1000$  ohms. From the fields in the plasma, the absorbed power can be found. This has been done for a quasistatic field approximation in the capacitively coupled regime where both ohmic and stochastic heating (see Sec. II.B) contribute to the power absorbed by the electrons (162). The calculation has not been performed for the inductive regime, where only  $\vec{E}_0$  contributes to the absorbed power. However, the analysis should be similar to that used for conventional inductive sources (see Sec. V).

Power can be simply coupled from an external generator to the resonator, and the condition for a match (critical coupling) can be estimated approximately from a perturbation analysis. Consider the rf generator and its transmission line to have characteristic impedances  $Z_S$ , with one side of the transmission line connected to the helix at the tap position  $z_T$  and the other side connected to the outer shield, as shown schematically in Fig. 28. Since the helix characteristic impedance  $Z_0$  given in (6.2) is typically large compared to  $Z_S$ , we expect a match to occur with the tap made near the shorted end of the helical resonator, where the voltage is small and the current is large.

From perturbation theory, the conductance seen at the position of the tap is

$$G_T = \frac{2 P_{abs}}{|V_T|^2}, \quad (6.3)$$

where  $P_{abs}$  is the total RF power absorbed and

$$V_T = V_m \sin k_z z \quad (6.4)$$

is the helix voltage at the tap. For a match we require  $G_T = Z_S^{-1}$ . Substituting (6.4) in (6.3) and expanding for  $k_z z_T \ll 1$ , we obtain

$$V_m^2 k_z^2 z_T^2 = 2 P_{abs} Z_S. \quad (6.5)$$

For our example with  $k_z = \pi/(2L) = 0.052 \text{ cm}^{-1}$ , and with  $P_{abs} = 51 \text{ W}$ ,  $V_m = 1610 \text{ V}$  and  $Z_S = 50$

ohms, we obtain  $z_T \approx 0.85$  cm, corresponding to a tap between one and two turns.

## VII. SURFACE WAVE DISCHARGES

Electromagnetic surface waves that propagate along a cylindrical plasma column can be efficiently absorbed by the plasma, hence sustaining a discharge. Surface waves, which are propagating modes having strong fields only near the plasma column surface, were first described by Smullin and Chorney (167) and Trivelpiece and Gould (168). The first surface-wave sustained discharge was operated by Tuma in 1970 (169). Moisan and his group at the Universite de Montreal have extensively analyzed the concept and developed high power wave launching systems over a wide frequency range (1 MHz–10 GHz). Surface wave sources have been reviewed by Moisan and Zakrzewski (170). Although there are some applications to materials processing (171-173), the absorption length  $\alpha_z^{-1}$  for the surface modes tends to be long, such that  $L \gg R$  for these discharges. Hence, they are not suitable as low profile sources for wide-area materials processing, and have found wider application for ion sources, lasers and spectroscopy. Surface wave discharges having diameters as large as 15 cm have been operated, although diameters of 3–10 cm are more commonly used. The simplest sources operate without an imposed axial magnetic field. At the high densities of interest here, the sources must be driven at microwave frequencies in the range of 1–10 GHz.

The simplest electromagnetic surface mode propagates on a non-magnetized plasma column of radius  $R$  confined by a thick dielectric tube (radius  $b \gg R$ ) having relative dielectric constant  $\mathcal{K}_d$ . The azimuthally symmetric  $m = 0$  mode has  $\tilde{H}_z = 0$  and

$$\tilde{E}_z = \tilde{E}_{z0} \frac{I_0(k_{\perp p} r)}{I_0(k_{\perp p} R)} \exp j(\omega t - k_z z), \quad r < R, \quad (7.1)$$

$$= \tilde{E}_{z0} \frac{K_0(k_{\perp d} r)}{K_0(k_{\perp d} R)} \exp j(\omega t - k_z z), \quad r > R, \quad (7.2)$$

where

$$k_{\perp p}^2 = k_z^2 - k_0^2 \mathcal{K}_p, \quad (7.3)$$

$$k_{\perp d}^2 = k_z^2 - k_0^2 \mathcal{K}_d, \quad (7.4)$$

and where  $\mathcal{K}_p$ , given by (5.2), is the plasma relative dielectric constant.  $I_0$  and  $K_0$  are the modified Bessel functions of the first and second kind,  $k_{\perp p}$  and  $k_{\perp d}$  are the transverse wavenumbers inside and outside the plasma respectively, and  $k_z$  is the complex axial propagation constant. We note from the form of the Bessel functions that the fields decay away from the surface of the plasma in both directions.

The transverse fields are obtained from  $\tilde{E}_z$  using Maxwell's equations. In particular, we find

$$\tilde{H}_\theta = -\frac{j\omega\epsilon_0 \mathcal{K}}{k_{\perp}^2} \frac{\partial \tilde{E}_z}{\partial r}$$

in the two regions. The continuity of the tangential magnetic field  $\tilde{H}_\theta$  then yields the dispersion equation

$$\frac{\mathcal{K}_p}{k_{\perp p} R} \frac{I_0'(k_{\perp p} R)}{I_0(k_{\perp p} R)} = \frac{\mathcal{K}_d}{k_{\perp d} R} \frac{K_0'(k_{\perp d} R)}{K_0(k_{\perp d} R)}. \quad (7.5)$$

From (7.1) and (7.2), it is clear that  $k_{\perp} R \gg 1$  for the surface mode to decay rapidly. Using the asymptotic expansions of the Bessel functions  $I_0'/I_0 = 1$  and  $K_0'/K_0 = -1$ , we obtain

$$\mathcal{K}_p k_{\perp d} = -\mathcal{K}_d k_{\perp p}. \quad (7.6)$$

Substituting (7.3) and (7.4) into (7.6) and solving for  $k_z$  yields

$$k_z = k_0 \left[ \frac{\kappa_p \kappa_d}{\kappa_p + \kappa_d} \right]^{1/2} \quad (7.7)$$

For the case of no loss,  $\nu_c = 0$ , we obtain from (7.7) that

$$k_z = \kappa_d^{1/2} \frac{\omega}{c} \left[ \frac{\omega_{pe}^2 - \omega^2}{\omega_{pe}^2 - (1 + \kappa_d)\omega^2} \right]^{1/2}$$

Figure 30 shows  $k_z$  versus  $\omega$  for the lossless case. We see that  $k_z$  is real for  $\omega \leq \omega_{res}$ , where  $\omega_{res} = \omega_{pe}/(1 + \kappa_d)^{1/2}$  gives the resonance  $k_z \rightarrow 0$  of the surface wave. For  $\omega \ll \omega_{res}$ , we see that  $k_z \approx \omega/c$ . However, in this low frequency limit, the ordering  $k_{\perp} R \gg 1$  is not valid, and the complete dispersion equation (7.6) must be solved numerically. The result is similar to that shown in Fig. 30. The region of interest for surface wave sources is  $\omega$  near but just below  $\omega_{res}$ . Hence for high density sources, the frequencies of interest are above 1 GHz; i.e., microwave frequencies.

Fixing  $\omega$  for the source, we introduce the resonance value of the density  $n_{res} = \epsilon_0 m \omega^2 (1 + \kappa_d) / e^2$ . Then the surface wave propagates for densities  $n_0 \geq n_{res}$ . The source operation for the usual case of a long, thin source,  $L \gg R$ , follows from the general principles described in Sec. II.A. In particular the local power balance along  $z$  determines the density  $n_0$  for a given absorbed power  $P'_{abs}$  per unit length along the column, as in the derivation leading to (2.19). Letting  $P_w$  be the power carried by the wave along the column at the position  $z$ , at which the density is  $n_0$ , then

$$P'_{abs}(n_0) = 2 \alpha_z(n_0) P_w \quad (7.8)$$

where  $\alpha_z$  is the axial attenuation constant of the wave fields at the density  $n_0$ . Equating  $P'_{abs}$  to the power  $P'_{lost}$  lost per unit length,

$$P'_{lost}(n_0) = e n_0 u_B A'_{eff} \mathcal{E}_L \quad (7.9)$$

where  $A'_{eff} = 4\pi R h_R$  is the effective (radial) loss area per unit length, we obtain  $n_0(z)$  for a given wave power  $P_w(z)$ .

The mode attenuates as it propagates along  $z$  due to a non-zero  $\nu_c$ . Letting  $\nu_c \ll \omega$  in (5.2), substituting this in (7.7), and taking the imaginary part, we obtain the attenuation constant  $\alpha_z(n_0) = -\text{Im } k_z$  at a fixed  $\omega$ . The expression is complicated and we give only the scaling for  $n_0$  greater than, but not too near, resonance:

$$\alpha_z \propto \frac{n_0 \nu_c}{(n_0 - n_{res})^{3/2}} \quad (7.10)$$

At resonance, there is a finite  $\alpha_z$ , while for  $n_0 < n_{res}$ , the wave does not propagate and  $\alpha_z$  falls sharply. For this variation of  $\alpha_z$ ,  $P'_{abs}$  is plotted versus  $n_0$  for several different values of  $P_w$  in Fig. 31. The linear variation of  $P'_{lost}$  given by (7.9) is also plotted on the figure. The intersection of  $P'_{abs}$  with  $P'_{lost}$  determines the equilibrium density along the column. It can be seen that there is a minimum value  $P_{wmin}(z)$  below which a discharge at that  $z$  cannot be sustained. A discharge forms near the position of surface wave excitation  $z = 0$  for  $P_{wmax} > P_{wmin}$ . As the wave propagates,  $P_w$  attenuates along  $z$  due to wave absorption. A discharge cannot be sustained when  $P_w$  falls below  $P_{wmin}$  at  $z = z_{max}$ . Hence the discharge exists as a finite length plasma column over  $0 < z < z_{max}$ . Typical plasma column variations of  $n_0$  and  $P_w$  are shown in Fig. 32.

We note in Fig. 31 that there are generally two intersections of  $P'_{abs}(n_0)$  with  $P'_{lost}(n_0)$ . The lower density intersection is an unstable equilibrium because a fluctuation that decreases  $n_0$  leads to  $P'_{abs} < P'_{lost}$ , thus further decreasing  $n_0$ . The higher density intersection is stable by similar reasoning.

High power wave launchers and matching networks for surface wave discharges have been developed (170). The addition of an axial magnetic field allows further choice of propagating modes (174), but has not been applied to materials processing.

## VIII. PLASMA TRANSPORT

In the preceding sections, we have outlined simple, unifying, analytical theories with which plasma source design can be understood and the generation rates and densities of ions and electrons can be quickly estimated. This analysis could be extended by using the electron temperature from (2.11) and suitable cross sections, to estimate generation and loss rates, and thereby densities, for reactive neutral species. We now turn to plasma transport: effects on materials processes, measurements, and strategies for control.

Consider etching. We can understand the influence of plasma transport on etching rates by reviewing a simple model proposed by Mayer and Barker (175) to explain the so-called ion-neutral synergistic effect (176,177). The etching rate may be expressed as the ion flux times the average volume removed per ion. Alternatively, one may express the etching rate as the neutral flux times the reaction probability times the volume removed per reaction event. Such rate expressions, however, cannot be directly applied because the yield per ion and the reaction probability of neutrals both depend on the neutral and ion fluxes. This linkage can be broken by expressing rates in terms of the ion- and neutral-flux-dependent surface coverage of reactants. Assuming that the yield per ion is proportional to the ion energy times the surface coverage of the chemically assisting neutral species, the etching rate is given by:

$$ER = \nu_i \Theta \epsilon_i \Gamma_i, \quad (8.1)$$

where  $\nu_i$  is the volume removed per unit bombardment energy ( $\text{cm}^3/\text{eV}$ ) for a saturated surface, and  $\Theta$  is the surface coverage. For this simple model, we assume that  $\nu_i$  is independent of  $\epsilon_i$ . To complete the model, we assume Langmuir adsorption kinetics where the reactive sticking probability of neutrals is proportional to the number of bare sites on the surface. Thus, the etching rate is also given by:

$$ER = \nu_n SC_0 (1 - \Theta) \Gamma_n, \quad (8.2)$$

where  $\nu_n$  is the volume removed per reacting neutral ( $\text{cm}^3$ ),  $SC_0$  is the reactive sticking probability on a bare surface (unitless), and  $\Gamma_n$  is the neutral flux ( $\text{cm}^{-2}\text{s}^{-1}$ ) to the surface. Equating the above rate expressions, we obtain an expression for the surface coverage as a function of the ion energy flux to neutral flux ratio.

$$\Theta = \frac{1}{1 + \nu_i \epsilon_i \Gamma_i / (\nu_n SC_0 \Gamma_n)} \quad (8.3)$$

Substituting this into (8.1) we obtain our final expression for the etching rate as a function of the ion and neutral fluxes.

$$ER = \frac{\nu_i \epsilon_i \Gamma_i}{1 + \nu_i \epsilon_i \Gamma_i / (\nu_n SC_0 \Gamma_n)} \quad (8.4)$$

Ion-neutral synergy is clearly evident in (8.4): If the neutral flux is negligible,  $\nu_n SC_0 \Gamma_n = 0$ , the etch rate becomes vanishingly small (we have neglected sputtering); similarly, when the ion energy flux is negligible,  $\epsilon_i \Gamma_i = 0$ , the etch rate again vanishes (we have neglected thermally activated neutral etching). Thus, the total etch rate with both neutrals and ions is greater than the etching rates with either species alone. (176,177) The validity of (8.4) has been verified for many material/ion/assisting-species combinations including: Si/He<sup>+</sup>/Cl<sub>2</sub> (178), Si/Ne<sup>+</sup>/Cl<sub>2</sub> (178), Si/Cl<sub>2</sub><sup>+</sup>/Cl<sub>2</sub> (179), Si/Ar<sup>+</sup>/Cl<sub>2</sub> (175,178,180), SiO<sub>2</sub>/CF<sub>x</sub><sup>+</sup>/CF<sub>4</sub> (179,181), and organic polymer/O<sub>2</sub><sup>+</sup>/O<sub>2</sub> (182). The measured dependence of the surface coverage on the ion to neutral flux ratio has also confirmed the predictions of (8.3) for the Si/Ar<sup>+</sup>/Cl<sub>2</sub> system (175,180).

There are two interesting limiting cases of (8.4). When  $\nu_n SC_0 \Gamma_n \gg \nu_i \epsilon_i \Gamma_i$ , the surface is saturated with neutrals and the etching rate  $ER = \nu_i \epsilon_i \Gamma_i$  depends only on the ion energy flux and is independent of the neutral flux as assumed, for example, by Shaqfeh and Jurgensen (183). In this case, ion generation and transport in the plasma will govern etching rates and etching uniformity. In the opposite case where  $\nu_n SC_0 \Gamma_n \ll \nu_i \epsilon_i \Gamma_i$  the surface is starved for neutrals and the etching rate  $ER = \nu_n SC_0 \Gamma_n$  is proportional only to the flux of assisting neutral species. Which regime is dominant? That is dictated in large part by source design and operation.

The ion-neutral synergism is useful for understanding rate enhancement when both ions and neutrals impinge on surfaces. It is also easy to understand, then, the origin of anisotropy in plasma etching: because ion transport is anisotropic, etch rate enhancement via the ion-neutral synergism is also anisotropic. However, other factors must also be considered. For example, the expression for the etching rate above ignores the possibility that there is a threshold energy below which the reactive ion sputter yield  $\nu_i$  is negligible (184,185). Such an effect is clearly evident in the  $Cl_2$  helicon etching of  $SiO_2$  as a function of bias shown in Fig. 33 and can play a role in determining selectivity of etching one material with respect to another. Similarly, damage created by atomic displacement when an energetic ion impinges on a surface may be minimized or even eliminated by tuning ion energies below the damage threshold. In general, the threshold energies for etching and damage are poorly known, but one of the guiding principles in and major motivations behind new plasma source development is that ion energies must be "fine" tuned to take advantage of threshold effects.

### VIII.A The Ion Energy Distribution Function

In Sec. II.A.2 we estimated the mean ion energy and mean ion velocity at the sheath edge as a function of electron temperature, source design, and rf biasing. However, these simple scaling relationships do not provide estimates of the ion energy distribution function, iedf, or spread in ion energy. This is by no means a trivial matter. What good is it, for example, to fine tune  $\epsilon_i$  to just above threshold for etching poly-Si and just below threshold for etching  $SiO_2$  when the breadth of the iedf is 5 times broader than its mean?

In equilibrium, the iedf is characterized simply by the ion temperature, which, for convenience, we generalize to  $T_i \equiv M \langle (u_i - \langle u_i \rangle)^2 \rangle / e$  (in volts) for use in describing the iedf in non-equilibrium systems. In magnetized, low pressure, high efficiency plasmas considered here, the iedf is frequently anisotropic so that different "temperatures",  $T_{i\perp}$  and  $T_{i\parallel}$  are needed to characterize the iedf perpendicular and parallel, respectively, to the magnetic field axis. Even in unmagnetized plasmas, one expects an anisotropic iedf as ions are accelerated along a specific direction. The ion velocity distribution function, ivdf, may also depart significantly from a Maxwellian form, in which case the temperatures defined above are inadequate to describe the distribution function: higher order moments are also required.

Source design and operation determine the iedf. Ions gain directed energy by acceleration in an electric field, created, for example, by an expanding magnetic field, by sheaths at bounding surfaces, by double layers and striations separating different plasma regions, by pre-sheaths, and by applied bias voltages (Sec. II.A.2). Ions lose energy by collisions, primarily with neutral atoms and molecules. Two collisional processes are dominant: charge exchange and elastic scattering. Charge exchange is effective in transforming hot, fast ions into hot, fast neutrals and cold, slow neutrals into cold, slow ions. Elastic scattering is effective in transforming directed energy gained by the ions falling through a potential into random energy with a large component perpendicular to the strong electric field. Both processes tend to broaden the iedf and the ion angular distribution function, iadf, and thereby possibly compromising selectivity, anisotropy, rate, and damage control.

Besides collisional energy transfer, the iedf can also be broadened, (so that precision energy control is lost), as a result of ionization occurring over a distributed sheath created, for example, by plasma expansion or by fluctuations in the plasma potential caused by power source fluctuations or inherent plasma instabilities (114).

Another limit to ion energy control in plasma processing has been little considered until recently (143): the creation and build-up of energy in excited states. All atomic ions have metastable excited electronic states that typically can pool energies of 10 eV or more above the ground state. Recent experimental work

indicates that at least 25% of the ions in a low pressure argon helicon plasma are in excited states with more than 16 eV energy above the ground state ion (143). Molecular ions can also effectively pool energy in vibrational and rotational modes as well as in excited electronic states. The pooling of energy in excited states should be most important in low pressure, high density plasmas where deactivation by collision with neutrals is relatively rare compared to frequent production by collision with electrons. How important 10 eV or more of excess, internal energy can be in etching and deposition applications must depend on the specific materials involved but is basically an open question for which little or no data exist. Besides metastable states, in high density plasmas one must also anticipate the production and build-up of large concentrations of doubly ionized ions. These will impact device surfaces with at least two times the kinetic energy of their singly ionized counterparts. To make matters even more complicated, metastable and doubly charged ions may have significantly different iadfs thereby making CD as well as selectivity and damage more difficult to control.

**VIII.A.1 Ion Transport and Etching Anisotropy** It is instructive to consider the consequences of a finite iadf on etch anisotropy in the regime where the ion energy flux is rate limiting, i.e.  $\nu_n SC_0 \Gamma_n \gg \nu_i \epsilon_i \Gamma_i$ . Ions impinging on the surface at oblique angles may accelerate etching of the sidewall and compromise pattern transfer fidelity. A useful metric for describing the iadf is the normalized, energy-flux-weighted, cumulative angular distribution function (66,183):

$$C(\theta) = \frac{\int_0^\theta \int_0^\infty d\theta \sin\theta d\epsilon_i \cos\theta \gamma(\theta, \epsilon_i) \epsilon_i(\theta)}{\int_0^{\pi/2} \int_0^\infty d\theta \sin\theta d\epsilon_i \cos\theta \gamma(\theta, \epsilon_i) \epsilon_i(\theta)}, \quad (8.5)$$

where  $\theta$  is the polar angle from the surface normal and  $\gamma(\theta, \epsilon_i) \cos(\theta)$  is the differential ion flux normal to the surface. Physically,  $C(\theta)$  is proportional to the etching rate of a surface perpendicular to the accelerating electric field and shadowed by a cone of half angle  $\theta$  when the etching is ion-energy-flux-limited (183). Thus, measurement or calculation of  $C(\theta)$  is necessary for accurate simulation and prediction of etched profiles.  $C(\theta)$ , in turn, is determined by the transport of ions to and then through the sheath to the wafer surface.

Since the sheaths are so thin in high efficiency plasmas (Sec. II.A.2), transport of ions through the sheath is effectively collisionless:  $s/\lambda_i \ll 1$ . This is one of the characteristics of high density plasmas that distinguishes them from the conventional rf diode and is a direct consequence of the high charge density and lower rf bias voltages at lower pressures. Because the sheath is collisionless, the perpendicular ion velocity at the sheath edge is preserved as the ions are accelerated to the wafer surface. Thus,  $T_{i\perp}$  largely determines the anisotropy of the ion transport and the angular dependence of  $C(\theta)$ . Consider a simple example, where the spread in  $u_{ix}$ , ion speed normal to a surface in the xy plane, is negligible compared to the velocity gained by acceleration across the sheath,  $u_{ix} \equiv (2eV_s/m)^{1/2}$ , and the distribution of perpendicular velocities,  $f(u_{i\perp})$ , is Gaussian with temperature  $T_{i\perp}$ . In this case,

$$C(\theta) = \frac{\int_0^\theta d\theta \tan\theta \exp(-\beta \tan^2 \theta) / \cos^3 \theta}{\int_0^{\pi/2} d\theta \tan\theta \exp(-\beta \tan^2 \theta) / \cos^3 \theta} \quad (8.6)$$

where  $\beta \equiv V_s/T_{i\perp}$ . This function and its derivative are plotted in Fig. 34 for  $\beta = 10$  and 100 along with the corresponding function for an isotropic angular distribution, i.e.  $T_{ix} = T_{i\perp}$  and  $u_{ix} = 0$ . Clearly, the effects of transverse ion energy can be significant and the design of plasma sources must take into account the mechanisms by which ions gain energy transverse to the surface normal. Before discussing these design aspects, we digress to consider how measurements of the iedf, ivdf, and iadf are made.

### VIII.B Methods for Measuring Ion Energy Distribution Functions

Electrostatic energy analysis and Doppler-shift spectroscopy are the two methods used most often for measuring ion energy and velocity distributions, respectively. Electrostatic energy analyzers consist of a pin-hole to sample the ions, a grid at the same potential as the sampling electrode to provide a field-free drift, grids to repel electrons and accelerate ions, grids to retard ions below a cut-off energy, and a detector (Fig. 35). If desired, ions can be mass filtered first and then energy analyzed. The distribution function is obtained by differentiating the measured ion current as a function of retarding voltage. Advantages of this technique stem from its universality and simplicity. Recently, Liu et al. (186) have used an electrostatic energy analyzer with a sectored current collector to determine not only the iedf but also the iadf at each energy, albeit with fairly low angular resolution, in an rf diode reactor.

In high charge density plasmas, these measurements are more challenging than usual if quantitatively meaningful data are to be obtained. For example, the pin-hole acts as an energy dependent lens and restricts the solid angle from which ions are accepted, thus discriminating against detection of low energy, obliquely incident ions. The usual solution to this problem is to use pinholes that are small compared to the sheath thickness, but because the Debye and sheath lengths are so short in high density sources (see Sec. II.A.2), the pin-hole must be  $\ll 50 \mu\text{m}$  to minimize artifacts. Unless the sampling is done through the wafer platen, the technique is also inherently intrusive: the sampling probes are relatively large, drawing significant current, and inducing a sheath and pre-sheath that can perturb the plasma over large distances. In a magnetized plasma, the ion sampling probe will subtend only a sub-set of flux tubes resulting in perturbations that are radially isolated but which propagate large distances along the flux tubes. In strong magnetic fields, ions are easily deflected in the analyzer and extra care must be taken to ensure that angle and energy distribution functions are not distorted. Finally, ion sampling in the plasma using probes lacks good spatial resolution. Despite these deficiencies and caveats, electrostatic energy and angle analysis is well suited for sampling through the wafer platen which yields the most vital information from a processing perspective: the iedf and iadf at the wafer.

Since the sheath is collisionless, however, it can be useful to measure the ivdf throughout the plasma. This can be done with great precision by using spectroscopic methods that rely on the shift in absorption or emission frequency (Doppler effect) that occurs when the ion is moving with respect to the reference frame:

$$\bar{\sigma} = \bar{\sigma}_0(1 - u_x/c) \quad (8.7)$$

where  $\bar{\sigma}$  is the Doppler shifted absorption or emission frequency;  $\bar{\sigma}_0$  is the corresponding line-center (rest velocity) frequency;  $u_x$  is the ion velocity along the light beam propagation direction, taken here to be along the  $\hat{z}$  axis; and,  $c$  is the speed of light. In both absorption and emission experiments, the measured line profile as a function of frequency is given by an integral over the perpendicular velocity components,  $u_x$  and  $u_y$ , and the spatial volume sampled:

$$I(\nu) d\nu \propto \iiint \iiint n_0(x,y,z) f(u_x, u_y, u_z, x, y, z) du_x du_y dx dy dz du_z \quad (8.8)$$

where the limits of integration correspond to the volume sampled. Both the ion density,  $n_0$  and the ivdf,  $f$ , are assumed to depend on position, *i.e.* the plasma is not uniform. Because of the integrations in (8.8), Doppler-shifted absorption and emission data must be measured along many axes and then suitably transformed to obtain a truly one-dimensional ivdf at any given position (187). In the simplest case of cylindrical symmetry, for example, an Abel inversion of line profiles obtained from line-of-sight along a cord, must be used to obtain the radial variation of the radial component of the ivdf. Without inversion, the data are of little quantitative value in distinguishing, for example, between random and directed energy.

The multiple integral in (8.8) is easily simplified experimentally by detecting absorption via the appearance of fluorescence, *i.e.* laser-induced fluorescence (LIF). In this case, the fluorescence induced by absorption of laser light is detected perpendicular to the laser propagation direction and imaged onto a spatial filter that discriminates against all but a small portion of the  $\hat{z}$  axis (Fig. 36). Typical spatial resolution along  $\hat{z}$  or  $\hat{x}$  - dictated by laser beam diameter, the magnification provided by the fluorescence collecting lenses, and the dimensions of the slits onto which the fluorescent image is projected - is 0.5 - 2 mm, sufficiently small for probing all but the sheath regions of low pressure high density discharges that the integrals over  $x$ ,  $y$ , and  $z$  in (8.8) are eliminated. Thus, the LIF method provides a precision measurement of the ivdf, albeit

still averaged over the velocity components perpendicular to the laser propagation direction,<sup>4</sup> at a specific point in the plasma and, thereby provides information on distributed sheaths, distributed ionization, plasma uniformity, etc.

Because ground state ions typically undergo rapid charge exchange with ground state neutrals, information can be lost concerning ion formation and transport when ground state ions are probed using LIF. The component of ion velocity measured will be dictated by the energy gained from the field since the last collision:

$$u_i \approx (2eE\lambda_i/M)^{1/2}. \quad (8.9)$$

Thus, such measurements tend to sample the local field. For example, den Hartog et al. (188) showed that above 1.0 mTorr, the drift of  $N_2^+$  downstream from an ECR source is given by

$$u_i = \mu(E)E \quad (8.10)$$

where  $\mu(E)$  is the field-dependent mobility (2.5), dictated in large part by the charge exchange cross section. In fact, using (8.10), den Hartog et al. deduced the electric field from the measured ion Doppler shift.

By contrast, consider the collisionless limit where the Doppler shift is now a measure of the energy gained,  $e\Delta V$ , by the ions between the point of formation and the point of observation. If ions are formed over a large enough region so that the plasma potential varies significantly, a distribution of Doppler shifts will be measured. If a net shift is observed, it means that the ions have fallen through a potential which in turn implies, through the Boltzmann relation (2.7), a plasma density gradient. Of course, the collisionless limit may be realized by probing ground state ions at low pressures ( $\ll 1$  mTorr) or by probing excited ionic states with smaller collisional cross sections. Such an approach has been taken by Sadeghi *et al.* (101,189,190). who probed metastable ionic states of Ar and Cl. Because charge exchange is a 2-electron process ( $3p^43d \leftrightarrow 3p^6$  in Ar) for the metastable state and a 1-electron process ( $3p^5 \leftrightarrow 3p^6$  in Ar) for the ground state, it is reasonable to expect the charge exchange cross section to be smaller for the metastable state. Furthermore, metastable states, and excited states in general, can often be quenched easily at higher pressures, for example by the nearly resonant Penning ionization process in Ar:



Thus, such destructive collisions help to preserve the collisionless ivdf by selectively removing ions that have undergone collision.

### VIII.C Methods for Measuring Plasma Potentials

The variation in plasma potential caused by expansion, pre-sheath formation, distributed sheath formation, etc. can be measured either by spatially resolving ivdf's (101) or by using electrostatic (Langmuir, emissive, double, ...) probes. It is beyond the scope of this work to discuss electrostatic probe methodology and the reader is referred to the reviews by Chen (191) and Hershkowitz (192) and the book by Swift and Schwar (193). Of particular note is the recent review by Godyak et al. (194) who describe the great care that must be used when using probes to measure plasma properties in the presence of rf excitation or bias. In addition, several caveats are offered concerning the use of Langmuir probes in measuring plasma parameters in high density, magnetized plasmas. As Chen points out (191), making meaningful probe measurements in magnetized plasmas is extremely difficult. An anomalously small electron to ion saturation current ratio is a clear indication that the probe characteristic is distorted by the magnetic field. When in the electron saturation current regime, the probe will tend to deplete electrons along a flux tube but not outside this flux tube thereby giving an anomalously small electron saturation current and perturbing the discharge. It is often possible to see visually the distortion of the plasma created by insertion of a probe; in etching and deposition plasmas, it is also possible to image the probe onto the thin film being processed.

<sup>4</sup> To obtain ion trajectories, one must resort to optical tomography as described by Koslover and McWilliams (187). This approach, while elegant, requires optical access not readily available in processing reactors.

These distortions are important when interpreting the probe current-voltage characteristic in terms of electron "temperature" or the electron energy distribution function (eedf) or the plasma potential. For example, the plasma potential is routinely estimated by linearly extrapolating, on a semi-log plot, the current from the electron current saturation regime into the electron retarding current regime (191) and similarly extrapolating linearly the current from the retarding current regime into the saturation current regime. Where the two lines intersect is commonly taken to be the plasma potential. Clearly, if the electron current is artificially suppressed for the reasons discussed above, the plasma potential might be in error. With these caveats in mind, we still use literature estimates of plasma potential and electron temperature determined in this way. From comparisons with recent numerical simulations (195) we find that the qualitative trends are useful in gaining insight into high density plasma generation and transport.

#### VIII.D Measurements of Energy Distributions and Potentials

*VIII.D.1 Ion Acceleration Outside the Sheath* Most measurements of high efficiency plasma iedfs have been done for diverging field ECR systems. The work of Matsuoka and Ono (196,197) is typical (Fig. 37). Microwaves are launched from a cavity into a high magnetic field region so that the RHP wave propagates and then is absorbed, heating electrons in the process (Sec. III). Because the magnetic field continues to decrease and, equivalently, expand, the plasma expands, the plasma density decreases and an ambipolar field is created that accelerates ions along the magnetic field gradient (Sec. II.A.2).

At some point downstream, ions are sampled through a 50  $\mu\text{m}$  pinhole and energy analyzed using two grids and a collector (Fig. 35). Although the relatively large orifice diameter and the use of arbitrary units for spatial distance makes this work of dubious quantitative value, the trends are still notable and are borne out in many other experiments (101,185,188,189,198-201).

Matsuoka and Ono focussed primarily on the effects of magnetic field configuration and pressure. By varying the current in an electromagnet located near the sampling plane, they modified the divergence of the magnetic field: from a mirror to a cusp. Figure 37 shows their iedf's for different sub-coil currents. As the field is collimated,  $\text{tipar}$  decreases and  $\epsilon_i$  shifts to lower values. At the same time, the ion current density increases, the plasma potential (deduced from Langmuir probe current-voltage characteristics) decreases, and the plasma potential gradient or electric field decreases. These effects are all consistent with reduced plasma expansion. The decrease in  $\text{tipar}$  results from the smaller electric field so that distributed ionization no longer broadens the iedf. By contrast, the largest  $\epsilon_i$  and  $\text{tipar}$  are obtained when the sub-coil magnet is used to produce a cusp before the sampling orifice. Note, however, that the iedf is clearly not Gaussian under these conditions and  $T_{iz}$  alone is not sufficient to describe the distribution function. Under these conditions, the plasma expansion is largest as the magnetic field decreases to zero and then reverses on the other side of the cusp.<sup>5</sup>

Regardless of the magnetic field configuration, both  $\epsilon_i$  and  $T_i$  decrease as the pressure is increased and charge exchange cools the iedf (185,196-199,202,203). Using Doppler-shifted LIF, Woods et al. (188,200,201) have examined the ground state  $\text{N}_2^+$  ivdf as a function of pressure downstream from a diverging field ECR source similar to Matsuoka and Ono's and also find (Figs. 38 and 39) that  $\epsilon_i$  and  $T_i$  decrease with increasing pressure. The LIF data further show a bimodal distribution function<sup>6</sup> resulting from charge exchange (204): the slow component has been created by charge exchange of fast ions with slow neutrals.

Acceleration of ions caused by plasma expansion can clearly be seen in the metastable LIF measurements of Sadeghi et al. (101,189) (Fig. 40) as well in electrostatic analyzer data (198,199,203,205). The

<sup>5</sup> Note that ions and electrons do not follow field lines through a cusp since the field decreases to zero (189).

<sup>6</sup> Because of kinematic compression when the ions fall through the sheath to the pinhole, the slow and fast velocity components tend to merge after the sheath is traversed. In addition, because of the finite size of the pinhole, one must be concerned about the energy or velocity dependence to Matsuoka and Ono's detection efficiency. In any case, the iedfs reported by Matsuoka and Ono, as well as others (101,189,201,203,204) are clearly asymmetric suggesting more than one velocity or energy component consistent with the LIF measurements.

ivdf measured where the source expands into the downstream region shows two components that are attributed to ions created in the source, the fast component, and ions created at the junction between source and reactor where the plasma expansion commences. The fast component has already gained an energy of approximately 13 eV parallel to the magnetic field axis as a result of the large potential difference between the source and downstream regions caused by the plasma expansion. This effect has been simulated recently by Porteous et al. (195) using a so-called hybrid approach where electrons are treated as a fluid and ions as particles. Their result for the plasma potential is reproduced here in Fig 41. When a collimating magnet is used downstream as in the Matsuoka and Ono experiments, this potential drop and the corresponding energy of the fast component both decrease. While the origin of this "distributed sheath" or double layer lies with the plasma expansion, the magnitude is also affected by a neutral density gradient from the source to the reactor (101,112,113,195) that arises from the depletion of neutrals due to the high ionization rate in the source, as well as ion acceleration and neutral heating. It is this gradient coupled with the decreasing electron density caused by the plasma expansion that causes the secondary source of ionization at the expansion point: here, the neutral density rises rapidly while the electron density is decreasing, thus leading to a local maximum in the ionization rate, shown schematically in Fig. 42. The ground state ion formation rate should also be enhanced at this point and these results suggest that many of the ions impacting device wafers downstream from the source will have been created downstream and not in the plasma source!

The effect of the wafer platen pre-sheath can also be seen in the metastable LIF data of Sadeghi et al. (101,189) (Fig. 40). The velocities of both slow and fast components increase systematically as the distance from the source increases and the platen is approached, and, assuming collisionless transport for the metastable ions at this low pressure (0.5 mTorr), a pre-sheath electric field of  $-0.5$  V/cm is determined, in excellent agreement with recent numerical simulations (195).

What are the consequences of ion acceleration outside the sheath? The primary result is to broaden the ivdf normal to the surface, but if the sheath potential is large, this will have a negligible effect on etch anisotropy. This is easily seen by approximating  $C(\theta)$  using a Gaussian distribution with temperature  $T_{ix}$  for the parallel component. Although the parallel distribution is clearly not Gaussian and therefore  $T_{ix}$  is not sufficient to describe the distribution, this simple analysis is useful for illustrating the effects of a finite width of the parallel ivdf. We find that broadening in the parallel ivdf, for  $T_{ix}/T_{i\perp} \sim 10$ , has a negligible effect on the anisotropy. However, the broadening of the parallel ivdf can degrade etching selectivity and increase atom displacement damage (Sec. IX) when processes are designed to operate near threshold. Therefore, sources should be designed to minimize both  $T_{ix}$  and  $T_{i\perp}$ . This is most easily done by using the close-coupled configurations (Fig. 12) that eliminate acceleration caused by plasma expansion. By making the plasma as uniform as possible, broadening of the ivdf resulting from distributed ionization can be minimized. However, the pre-sheath field cannot be eliminated and to the extent that ionization occurs in this region, some residual broadening of the ivdf is unavoidable.

**VIII.D.2 Transverse Ion Energy** Source designs that employ plasma expansion create further problems by broadening the perpendicular ivdf. This is clearly seen in the spatially resolved ivdf's measured using the LIF technique (Fig. 43): both ground state and metastable state ions show systematic Doppler shifts with increasing distance radially from the center axis of the source (101,189,201). These shifts correspond to acceleration along a radial electric field that in turn is created because of the plasma density gradient in the radial direction. Plasma expansion aggravates the magnitude of this density gradient and the corresponding potential gradient. Note that ions have little trouble crossing magnetic field lines since they are only weakly magnetized.

By collimating the downstream field, the shift in the ivdf is clearly reduced (Fig. 43) although, curiously, the broadening of the ivdf can increase as a result of local ionization. By adding the collimating field and increasing the confinement downstream, the ionization rate downstream is also increased. But ions created downstream have not been accelerated to the same extent radially as those ions which stream out of the source. Thus, collimating the field and increasing the confinement of plasma produces a slow, somewhat isotropic velocity component downstream.

Large radial density gradients and the resultant radial acceleration of ions can severely affect etching anisotropy, particularly on the outer edges of a wafer where the radial velocity component is largest (Fig.

43). This again is illustrated by calculating  $C(\theta)$  using a shifted Gaussian distribution for the  $u_{i\perp}$  velocity component (Fig. 34): besides  $\beta$ , we need another scaling parameter,  $\xi = 2u_{i\perp}^{(0)}/u_{is}$  or the ratio of the directed radial velocity to the velocity gained by acceleration through the sheath. In Fig. 34, we have chosen  $\beta = 100$  as before and  $\xi = 0.6$ . For a sheath voltage of 50 V, this corresponds to  $T_{i\perp} = 0.5$  V and a radially directed energy of 4.5 V or a directed velocity of  $4.6 \text{ km s}^{-1}$ , which is comparable to that observed at only 7 cm from the axis in Fig. 43. Note that  $C(\theta)$  exhibits a threshold for this case as the directed velocity exceeds the ion thermal speed and no ions can impact the surface at normal ( $0^\circ$ ) incidence (Fig. 34). However, for etched profile simulation, this situation is considerably more complex as the velocity distribution for finite radius is no longer axisymmetric: the profiles can be etched at a net angle with respect to the surface normal and  $C(\theta)$  is no longer directly correlated with the etch rate induced by ions within a cone angle  $\theta$ . To our knowledge, this problem has not been treated in simulations of etched profiles.

Besides the directed radial velocity component, in magnetized plasmas there is also rotational motion,  $u_{i\phi}$ , caused by  $\mathbf{E} \times \mathbf{B}$  and diamagnetic drifts (109). The diamagnetic drift arises from the diffusive flux along the radial density gradient. Downstream, where the magnetic field is usually weak, this rotational motion is a small fraction of the "thermal" spread in perpendicular velocity (101,189). However, in the source of an ECR where the magnetic fields are on the order of 1000 G, the rotational velocity can be many times the "thermal" velocity (195).

The last source of transverse energy is the "random" or "thermal" component. The distributions are Gaussian about their mean except for large radial positions (Fig. 43). However, the origin of this broadening is unclear. Given an electron temperature of 5 eV, an ion temperature of 0.25 eV, a plasma density of  $10^{12} \text{ cm}^{-3}$ , and an ion-electron energy transfer cross section of  $10^{-14} \text{ cm}^{-2}$  and assuming ambipolar diffusive loss for the ions, only  $\sim 10^{-3}$  eV of energy can be gained by the ions via elastic collisions with electrons before the ions are lost to the walls (Sec. II.A.1, 206); this is insufficient to account for the ion temperatures measured (Figs. 39 and 43). For lower charge densities and a smaller cross section, the energy transfer from electrons to ions is even less. Most likely, the "random" ion energy observed results from elastic collisions between ions and neutrals that convert the directed ion motion, discussed above, into random perpendicular motion. Because ionization takes place over dimensions that are large compared to the uniformity in the plasma potential, a distribution of ion energies in each direction also results as ions flow from one region to another; again, making the plasma more uniform will largely eliminate this source of broadening.

As shown in Fig. 39 for ground state  $N_2^+$ ,  $T_{i\perp}$  decreases monotonically as the pressure is increased, most likely as a result of charge exchange collisions. This means that linewidth control in anisotropic etching should be optimized at an intermediate pressure: at low pressures,  $T_{i\perp}$  is larger but if the pressure is increased too much, the sheath becomes collisional and linewidth control is sacrificed once more (66).

### VIII.E Ion Energy Control

As we have said, a primary motivation for replacing conventional rf diode systems with high efficiency sources is the need for independent control of ion energy and flux so that rate, selectivity, and film properties can be optimized. By placing the wafer on a platen to which a bias voltage is applied while generating the plasma with a high density source, this problem is nominally circumvented.

For most applications, rf biasing has been employed although rf is no longer essential, as it is with the conventional diode, since the plasma is maintained using a separate source. In conventional RIE, rf is used to maintain the plasma in the presence of insulating thin films on one of the electrodes. Because the measurements are easier to make, however, resort is made to dc biasing when the iedfs from high efficiency plasmas have been sampled. To our knowledge, Holber and Foster (185) and Sadeghi et al. (101) are the only ones to have examined the iedf and ivdf, respectively, with an applied rf bias. In the experiments of Holber and Foster, the electrostatic energy analyzer is biased along with the sampling electrode to measure the iedfs through the rf modulated sheath. The results are reproduced here in Fig. 44, where distributions are shown for two different frequencies: 0.5 and 20 MHz. In the high frequency case, the iedf is relatively narrow with a width of  $\sim 5$  eV and an average energy of  $\sim 35$  eV, corresponding to the streaming energy of 15 eV, resulting from expansion of a divergent-field ECR (see Sec. VIII.D.1), and a dc bias across the rf sheath of 20 eV.<sup>7</sup> At the lower frequency, the ion transit time across the sheath is long compared to the rf period

and the ion energy is modulated as the ion traverses the sheath. This leads to substantial broadening, ~ 37 eV, with a width determined by the peak-to-peak rf voltage. The maximum ion energy in this case corresponds to the peak rf voltage plus the streaming energy. Clearly, lower frequency bias should be avoided if precision ion energy control is desired to optimize selectivity and minimize atomic displacement damage. However, we shall see shortly (Sec. IX) that, in fact, the commercial ECR system sold by Hitachi as well as other prototype systems have been operated at frequencies as low as 400 kHz to minimize charge-up damage.

Although the above results indicate that rf biasing is useful for tuning ion energies, as desired, other experiments indicate that the extent to which ion energy can be precisely controlled depends on system design. Consider the recent results of Reinke et. al. (199) who used a dc bias to tune the ion energy, sampled through a pin-hole with an electrostatic energy analyzer (Fig. 35). The mean ion energy is only tuned with the dc bias when the biased electrode is "sufficiently" small (Fig. 45). In Reinke et. al.'s experiment, "sufficiently" small is an electrode whose diameter is 6 cm or less. In other experiments, Shirai and Gonda (207) used a 3x3 cm dc biased plate and Iizuka and Sato (208) used a 25 cm diameter electrode and found that the plasma and floating potentials, as measured using Langmuir probes, did not depend on the bias voltage for negative bias voltages, indicating that the biased electrode sheath in these cases were effectively modulated along with ion energy. In Shirai and Gonda's experiment, the electrode was smaller than the limit found in Reinke's experiment but this was not the case in the Iizuka and Sato experiment. However, in the latter, a grounded limiter was used at the exit of the source such that the plasma made good contact with ground.

What determines how small the biased electrode must be before gaining ion energy control? This is not a question unique to processing with high efficiency plasmas, but it is perhaps one that needs more thought when designing such sources with large areas of insulating materials in contact with a magnetized plasma. The voltage division between the biased electrode sheath and the grounded walls is dictated by the relative impedances of the sheaths (Fig. 46), yielding, for the plasma-to-plate dc self-bias voltage  $V_a$ :

$$V_a = V_{rf} \left[ \frac{Z_a}{Z_a + Z_b} \right]. \quad (8.12)$$

For the dc biasing case, the impedance is simply the sheath resistance which in turn depends on the electrode area, sheath thickness, and sheath conductivity according to

$$Z_{dc} = R = \frac{s}{\sigma A}. \quad (8.13)$$

For the more usual rf biasing case, the impedance can be approximated by the capacitive impedance which for a parallel plate depends only on the area  $A$  and sheath thickness  $s$ ,

$$Z_{rf} = \frac{1}{\omega C} = \frac{s}{\omega \epsilon_0 A}. \quad (8.14)$$

Thus, we see that at fixed  $s/\sigma$  in the dc case and fixed  $s$  in the rf case, the voltage ratios scale inversely with area ratios. Although these assumptions on  $s/\sigma$  and  $s$  are not valid, (8.12)-(8.14) illustrate the importance of the area ratio in determining the extent to which ion energies impacting wafer surfaces can be controlled using external bias supplies. Consider two limiting cases,

---

7 The experiments of Sadeghi et al. (101) provide further qualitative evidence for ion energy tuning by application of a 13.56 MHz bias, but the LIF method lacks sufficient spatial resolution to resolve the sheath and the ivdfs measured appear anomalously broadened as a result of the spatial averaging.

$$\frac{A_a}{A_b} \ll 1 \quad V_a \rightarrow V_{rf} \quad (i)$$

$$\frac{A_a}{A_b} \gg 1 \quad V_a \rightarrow 0 \quad (ii)$$

Clearly, for case (i), the desired result, we have control of ion impact energy. For case (ii), we have no control.<sup>8</sup>

RF biasing of the wafer platen is generally used in high efficiency sources. Taking into account the variation of sheath thickness with voltage, let us determine the ratio  $V_a/V_b$  of the dc plasma-to-electrode voltages at the powered wafer platen (a) and grounded (b) electrodes in high efficiency sources having unequal electrode areas  $A_a$  and  $A_b$ . Referring to Fig. 46, we see that the quantity usually measured, the dc bias voltage of the wafer platen with respect to ground, is given by  $V_{bias} = V_b - V_a$ . As will be shown below, simple one dimensional arguments (209) for Child law sheaths (2.18) assuming equal ion densities at the plasma-sheath edges of the platen and grounded electrodes yield the scaling of the voltage ratio on the area ratio as  $V_a/V_b = (A_b/A_a)^{1/4}$ , contrary to measurements (99,209-215) that indicate a much weaker dependence of  $V_a/V_b$  on  $A_b/A_a$  for area ratios much different from unity. One dimensional models incorporating the effects of the dc floating potentials (216) and one dimensional spherical shell models have also been developed (217,218), incorporating various assumptions for the sheath and glow physics, and obtaining a scaling more in agreement with measurements. However, rf biasing in high efficiency sources is generally done in finite cylindrical geometry having two dimensionless parameters; e.g., the powered-to-grounded electrode area ratio and the length-to-radius ratio for a finite length cylinder. In principle, the voltage ratio depends on both parameters, and, therefore, there is no simple scaling with the area ratio alone (219).

To determine the fundamental scaling formula in the limit of high voltage rf-driven sheaths (see Sec. II.A.2), we let  $\bar{x}$  be a two dimensional vector that specifies the position on the electrode surface,  $n_e(\bar{x})$  be the density at the plasma-sheath edge,  $V(\bar{x})$  be the dc plasma-to-electrode (sheath) voltage,  $s(\bar{x})$  be the sheath thickness, and  $\vec{J}(\bar{x})$  be the rf current density normal to the electrode surface. A key observation is that the plasma, being highly conducting, cannot support a potential difference greater than a few  $T_e$ 's. Since  $V \gg T_e$ , the plasma-sheath edge is an equipotential surface. Since each electrode *a* and *b* is also an equipotential surface, the plasma-to-electrode voltage across each sheath is a constant, independent of the position  $\bar{x}$  along the electrode surface. For the powered electrode, we therefore have  $V_a(\bar{x}) = V_a = \text{const}$ .

For high voltage capacitive sheaths, the rf voltage amplitude  $\bar{V}_a$  and the dc voltage drop  $V_a$  across the sheath are approximately equal:  $\bar{V}_a \approx V_a$ . In this limit, using (8.14), we can relate the rf current density to the dc sheath voltage and sheath thickness using the capacitive sheath assumption:

$$\vec{J}_a(\bar{x}) \propto V_a/s_a(\bar{x}) . \quad (8.15)$$

For a collisionless (Child law) sheath, we have from (2.18) that

$$n_{sa}(\bar{x}) \propto V_a^{3/2}/s_a^2(\bar{x}) . \quad (8.16)$$

The total rf current  $\vec{J}_a$  flowing to the powered electrode is

<sup>8</sup> Note that the measured dc bias voltage in most systems is relative to ground and may bear little relation to the voltage across the sheath that accelerates ions to the wafer. Also, the measured voltage will depend not only on the effective area ratio of the grounded and biased surfaces but also the degree to which the electrode is insulated and what value of blocking capacitor is used in the rf circuit.

$$\tilde{I}_a \propto \int_{A_a} \tilde{J}_a(\bar{x}) d^2x . \quad (8.17)$$

Inserting (8.15) into (8.17) and using the collisionless sheath scaling to eliminate  $s_a$ , we obtain

$$\tilde{I}_a \propto V_a^{1/4} \int_{A_a} n_{sa}^{1/2}(\bar{x}) d^2x . \quad (8.18)$$

A similar expression to (8.18) is obtained for the grounded electrode  $b$ . Equating  $\tilde{I}_a$  to  $\tilde{I}_b$ , the current to the ground electrode, by continuity of rf current, we obtain the scaling formula for high voltage sheaths

$$\left[ \frac{V_a}{V_b} \right] = \left[ \frac{\int_{A_b} n_{sb}^{1/2}(\bar{x}) d^2x}{\int_{A_a} n_{sa}^{1/2}(\bar{x}) d^2x} \right]^4 . \quad (8.19)$$

We see that the voltage ratio is independent of the rf driving voltage and the electron temperature for high voltage sheaths. The voltage ratio is determined by integrals over the powered and grounded areas that depend on the density at the plasma-sheath edge. This density and its variation along the powered and grounded surface areas are determined by the generation and loss processes for ions in the bulk plasma (219).

We note that making the simple assumption  $n_{sb} = n_{sa} = \text{const}$  yields the scaling  $V_a/V_b = (A_b/A_a)^4$ . However, the density variations along the surfaces due to the plasma transport in finite cylindrical geometry strongly modify this scaling (219). Further, for large area ratios, the voltage across the grounded electrode is low and the dc floating potentials cannot be neglected (216,219). A further issue for bias control in high efficiency source design stems from the use of magnetic confinement and insulating liners. Magnetic confinement effectively limits cross field electron transport and thereby limits the grounded surface in contact with the plasma. To make matters worse, the use of insulating liners to reduce metallic wall sputtering (87,101,112,113), further reduces the grounded surface area and the plasma potential can easily be decoupled from ground. For rf biasing, a thick liner effectively makes  $s$  very large and has the same effect as making the grounded surface area very small. In other high density sources, such as the helicon, inductively coupled plasma, and helical resonator, the power is purposely coupled to the plasma through a dielectric wall and there is an inherent ground reference problem. In the helicon, for this reason, it is common to use a grounded plate at the top of the source. In the TCP and helical resonator, the problem may be less severe because magnetic confinement is not required and the plasma might "find" ground below the wafer surface. Unfortunately, few iedf measurements as a function of dc or rf bias have been made except for ECR sources.

**VIII.E.1 Plasma Anodization** In the above discussion we have focussed on tuning ion energies to optimize selectivity and linewidth control while minimizing atomic displacement damage during etching. However, ion energy control is critical for controlling the properties, such as stress, index of refraction, and stoichiometry, of deposited thin films (78). Recently, positive biases have been used for oxidizing single crystalline Si (61,62) and the process has been referred to as plasma anodization. As expected, Shirai and Gonda (207) and Iizuka and Sato (208) both found that the plasma potential floats above the bias potential when the dc bias voltage is made positive with respect to ground and a large electron current is drawn to the wafer platen. So, although the electron flux is increased to the wafer surface during these so-called anodization processes, electrons still diffuse against the electric field and are slowed as they impact the surface. There is also a low energy, positive ion flux that is less than the electron flux, since net current is drawn to the wafer.

## IX. Device Damage

### IX.A Atomic Displacement Damage

If conventional rf diodes did not produce excessive damage when operated at high power and low pressure, there might not be such a concerted effort toward developing high efficiency sources. For minimizing atomic displacement damage caused by energetic ion and/or neutral impact, the advantages of using high efficiency sources with independent ion energy and flux control seem clear. By reducing the plasma potential and decoupling ion energy and flux control, the extent to which atomic displacement occurs can be kept to a minimum. This is clearly evident in the experiments by Yapsir et al. (111) where Si was etched using a  $\text{CF}_4$  diverging-field ECR and the displaced atom density,  $\Delta D_{da}$ , was measured using Rutherford Backscattering Spectroscopy (RBS). Hara et al. made similar measurements using  $\text{SF}_6$  ECR plasmas to treat GaAs (220), where etching should be limited to physical sputtering, and to etch Si (221). In these experiments, comparisons to RIE treatments showed that  $\Delta D_{da}$  can be reduced by typically a factor of two using ECR treatments. Of course, such comparisons must be examined carefully to understand their meaning. In principle, if the same ion and neutral fluxes and energy distributions are obtained in both systems, the same damage should result. There is no inherent difference between RIE and ECR except that the latter affords superior control over these key parameters. Hara et al. made such a comparison at constant current density (Fig. 47) suggesting that the improvement with the ECR system stems from a narrowing of the iedf and/or a reduction in the mean ion energy; however, neither parameter was measured in either system.

Interestingly, Yapsir et al. (111) found that the displaced atom density was slightly reduced by application of an rf bias, which, as discussed above, should increase the ion energy. They noted similar improvements in other damage metrics when the rf bias was applied: smaller Schottky diode leakage currents, reduced heavy metal contamination, lower MOS generation current, and fewer defect-induced etch pits. Over the same range of rf bias power, the Si etch rate increased, suggesting that the reduction in damage was correlated with a faster removal of the damage layer. This is supported by the observation that  $\Delta D_{da}$  increased with rf bias power when argon was substituted for the  $\text{CF}_4$  gas and physical sputtering replaced ion-assisted chemical etching. On the other hand, X-ray photoelectron spectroscopy (XPS) measurements show a residual contamination layer containing Si, F, C, and O that is about 0.5 nm thicker when an rf bias is applied during ECR processing (222). Apparently, this added contamination has little effect on the electrical properties and RBS is probably too insensitive to detect the difference in lattice displacement. Clearly, more experiments along these lines are needed to understand how best to minimize plasma-induced damage as the bias voltage is changed. Simultaneous measurements of ion flux and energy are also needed.

### IX.B Contamination

Contamination by heavy metals, as documented by Yapsir et al. (111), raises important design issues for high density sources. Because the electron temperature can be relatively large compared to rf diode reactors, the potential difference between the plasma and the grounded or floating walls can exceed the sputtering threshold for the wall material (see Sec. II.A.2). Thus, while the ion energies are reduced relative to those impacting the electrodes in an rf diode, sputtering can still be a problem. This has been observed by several groups (87,101,111-113) and a common solution is to use a dielectric liner with low sputtering yield, such as quartz or alumina, in the source. However, sputtering of these materials may still occur, compromising etching selectivity (223) and leading to particulate formation. For example, if  $\text{SiO}_2$  is sputtered from a liner during poly-Si etching, it can be difficult to etch without applying a bias voltage to the wafer; with no bias, net deposition can occur. It is critical that source design take into account the ion energy and flux not only to the device wafer but also to the walls of the reactor.

### IX.C Charging

Another mechanism by which microelectronic devices can be damaged and manufacturing yields deleteriously affected is charging of insulators during plasma treatment. An excellent, short review has recently been presented by Gabriel and McVittie (224), who point out that charging damage has become more apparent in recent years as gate oxide thicknesses have shrunk to 10 nm or less. This problem is not unique to processing with high efficiency plasma sources and in fact was initially recognized as a problem in the stripping of photoresist using an rf barrel etcher (225). However, the larger current densities to the wafer and the possibility for large current non-uniformities resulting from magnetic confinement are cause

for concern when designing high efficiency sources for microelectronic device fabrication.

Some of the metrics used for evaluating charging damage include: the flat-band voltage shift ( $\Delta V_{FB}$ ) of a metal-nitride-oxide-silicon (MNOS) non-volatile memory device (226) (Fig. 48), the frequency of dielectric breakdown as a function of field strength across the dielectric (224,227-229), the leakage current in CMOS inverter circuits (230), and the threshold voltage shift in an MOS transistor (230).

*IX.C.1 Plasma Uniformity* While there may be many factors influencing charging damage, plasma uniformity is clearly one of the most important. For this reason, the damage is readily observed in rf magnetrons (88). Achieving adequate uniformity at the wafer surface is a central issue for high efficiency sources. There is no simple solution because of the many interrelated physics issues that affect uniformity. These include:

- (a) Incident (microwave or rf) power flux profile;
- (b) Wave refraction during propagation to the absorption zone;
- (c) Absorption zone size, shape, and location;
- (d) Wave absorption profile;
- (e) Transport of heated electrons and their subsequent ionization profile;
- (f) Transport and diffusion of bulk plasma (and free radicals) to the wafer surface.

We have touched on all these issues in the preceding sections. To some extent, these issues are alleviated in low profile or close coupled geometries, thus prompting recent interest in those configurations.

The effect of plasma uniformity has been most extensively studied by Samukawa (230,231) who used a Faraday cup to measure the ion current density as a function of axial and radial position in a diverging-field type ECR (Fig. 12a). The extent of oxide damage clearly correlated with the degree of radial non-uniformity in the ion current to the wafer. This can be seen in Fig. 49 where the leakage current measured from a CMOS inverter circuit is plotted vs. the ion current density difference,  $\Delta J_i$ , from the wafer center to the wafer edge. By varying the magnetic field configuration and the position of the wafer with respect to the resonance zone,  $\Delta J_i$  could be varied over the range shown producing a five order-of-magnitude variation in leakage current. By collimating the field and placing the wafer near the ECR resonance zone where the ion current density was more uniform (Fig. 12d), Samukawa showed that the extent of damage could be dramatically reduced.

Why should the uniformity of ion current density affect gate oxide damage? It is safe to say that this remains an open question, but the simple explanation offered in Fig. 50 is worth considering. Since the top surface of the wafer exposed to the plasma is isolated from the bulk of the wafer and substrate holder by, for example, gate and field oxide, the top surface of the wafer will charge to a potential such that the time-averaged ion and electron fluxes are equal. Providing the top surface is electrically conducting, for example, before etching is completed, any non-uniformity in the current density to the wafer will not result in a surface potential difference across the wafer. However, once the pattern clears at the etching end-point so that the top surface forms isolated regions, a surface potential can exist when the current density is non-uniform. The surface potential, in turn, is a driving force for Fowler-Nordheim tunneling current (226) through the insulating layer. The largest current will occur where the oxide is thinnest, i.e. the gate oxide, and if the current is large enough it can produce premature breakdown,  $\Delta V_{FB}$ , leakage current, etc. Processing in high efficiency plasmas leaves one particularly prone to this problem as the current densities, and therefore, the surface charge densities, are much larger than in conventional rf diode processing. Coupled with a difficulty in obtaining uniform plasma density in magnetized systems and the unprecedented thinness of gate oxides, the problem has recently become a matter of alarm (228).

*IX.C.2 Biasing* Application of a bias voltage to the wafer also affects the extent of gate oxide damage in high density plasma processing. Namura et al. (232) showed that the  $\Delta V_{FB}$  from an MNOS device increased, albeit non-uniformly across the wafer, as an rf bias was applied to the wafer exposed to a close-coupled ECR source (Fig. 12d). Thus, the advantage of putting the wafer into the source, as discussed by Samukawa, appears to be mitigated when a 13 MHz bias is applied to the wafer. Namura et al. suggest that

the application of rf bias produces a non-uniform current density to the wafer, which again leads to a surface potential difference, presumably because the rf current to the walls is larger on the edges nearest to the walls. They offer an equivalent circuit model that includes the MNOS devices on the wafer and the capacitive coupling of the wafer to the plasma through the sheath. A key ingredient of the circuit is the anisotropic conductivity of the plasma: conduction along the magnetic field being much larger than conduction across the field owing to magnetization of the electrons. Although this simple model appears to give good agreement with the observed radial dependence of  $\Delta V_{FB}$  across the wafer, the model parameters are *ad hoc* and the equivalent circuit model used to describe coupling of the plasma to the substrate of the device is not clearly explained.

Samukawa (233) also suggests that the 13 MHz bias results in a non-uniform plasma above the wafer and reports a "local discharge between the chamber wall and the substrate holder." To alleviate this problem, Samukawa reduced the bias frequency and found that both the plasma uniformity improved (Fig. 51) and the incidence of gate oxide breakdown was dramatically reduced (Fig. 52). At the same time, Tsunokuni et al. (234) reported similar observations. Samukawa says that use of such low frequencies eliminates the local discharge. Since the capacitive impedance of the sheath increases with decreasing frequency, the sheath becomes predominantly resistive at frequencies below 1 MHz with the sheath current being predominantly ion conduction current (64,78,236). If the plasma is uniform initially, applying a low frequency bias will serve primarily to accelerate ions to the surface without altering the plasma potential profile and producing large, localized currents to the walls.

The bias frequency dependence of the gate oxide damage illustrates once more the importance of plasma source design. Surely, the extent to which local discharges are created will depend on the geometry of the source and, in particular, the proximity of grounded surfaces to the wafer edge. We have already discussed how  $\Delta D_{ox}$  can increase with increasing ion energy so it does not appear desirable to solve the gate oxide damage problem by resorting to low frequency rf bias. In many ways this defeats the purpose behind using the high density plasma in the first place. Nonetheless, we note that Hitachi currently employs low frequency bias (typically  $< 2$  MHz) in their ECR machines sold for etching of poly-Si, metals, and oxides.

The sequence by which the plasma process is terminated apparently also has an effect on gate oxide damage. Samukawa (230) reports that when the rf (13 MHz) bias is extinguished prior to turning off the microwave power supply that the CMOS leakage current is reduced by more than five orders of magnitude and that the gate oxide breakdown voltage is increased by two times. The origin of this effect is not well understood and needs further investigation. Similarly, the extent of gate oxide damage produced by helicons, helical resonators, and TCPs has not been reported to our knowledge. Typically, 13 MHz bias frequencies have been used with these sources and it is reasonable to expect similar problems to arise.

#### IX.D Radiation

Photon irradiation is another mechanism by which microelectronic devices can be damaged during high efficiency plasma processing. In this regard, the difference between high density sources and conventional rf diodes stems from the efficiency of electron heating at low pressure that can lead to production of large excited state densities (143) and energetic photon irradiation (236). Damage to  $\text{SiO}_2$  by absorption of above-band-gap energy photons has been studied most extensively (237-239). Depending on the photon energy (240,241), the free electrons and/or holes created by the absorption process may find their way to traps within the oxide or at the oxide-silicon interface. In both cases, device performance can be affected by shifting threshold voltages and by creating leakage and generation currents. Although in some instances it is possible to anneal out such damage (237,238), it is preferable to prevent damage formation in the first place and thereby preserve the thermal processing budget (1). One means for doing this was suggested by Yunogami et al. (241) who showed that radiation damage could be minimized by maintaining the substrate at temperatures as low as 120 K during plasma irradiation. The improvement in the positive charge generation rate was ascribed to a reduction in the hole mobility at low temperature that enhanced the probability for recombination before trapping.

In addition to VUV photon production, Castagna et al. (242) have shown that runaway electrons in ECR plasmas can generate significant fluxes of x-rays when they impact the reactor walls. The runaway electrons are created primarily at lower pressures and higher microwave powers where the electrons can gain energy (Sec. III.B) faster than they dissipate it by collisions with neutrals. After acquiring more than  $\sim 100$

eV of energy, the collision cross sections begin to decrease with increasing electron energy permitting the electrons to "runaway" to energies approaching 1 keV before impacting the source walls and producing x-rays.

Unfortunately, there are virtually no measurements of *absolute* photon fluxes to device wafers in high density plasmas and therefore it is difficult to judge the severity of the radiation problem. Such measurements are essential if one wants to distinguish between x-ray, VUV, ion, electron, and fast neutral bombardment damage mechanisms and distinguish these in turn from the charging damage already discussed.

## X. SUMMARY AND REMAINING QUESTIONS

The results of any plasma process depend on more than just plasma properties and plasma source design. Choice of chemistry - both gas-phase and on the surface - play paramount roles in the outcome of etching, deposition, and passivation treatments. Nonetheless, plasma source design can influence the materials process. The plasma governs the generation and transport of reactive species to and from the surface and many surface processes are limited by this transport. We have seen that plasma source design can have a profound effect on charged particle transport. For example, high profile, diverging magnetic field designs induce a distributed sheath that accelerates ions to higher energies and limits ion energy control.

While most measurements and simulations have been concerned with the transport of ions and electrons, there have been but a few (201,243,244) measurements of neutral, reactive species transport in high efficiency plasmas. In only one case are we aware of a measurement of the degree of dissociation in an ECR plasma and this was made on N<sub>2</sub> gas (243). We have seen how sources differ in the mechanism by which electrons are heated and although it has been useful to view the electron energy distribution function as Maxwellian, subtle deviations may affect the generation rate of key reactive intermediates. Clearly, if we are to understand the subtle interplay between source design and surface modification we must measure the flux of reactive species to the surface and this means measuring the absolute concentrations and "temperatures" of gas-phase reactive intermediates.

Another factor influencing the transport of reactive neutrals is the composition of wall material in plasma sources. Consider that for each of the sources reviewed here, a dielectric, usually fused silica or alumina, is used either as a barrier through which wave energy is coupled or as a liner to protect against sputtering of metallic wall materials. Regardless of electron heating and ion transport mechanisms, the extensive use of these materials marks a sharp distinction between the new generation of high efficiency sources and their conventional rf diode predecessors. These materials can alter surface chemistry by reducing reactant fluxes, by the loading effect (223), or by generating small concentrations of species such as oxygen that can dramatically alter the rates of both gas-phase and surface reactions (245). This area, again, is virtually unexplored.

We have seen that source design can be critical for minimizing the extent of damage and yield loss. In particular, plasma uniformity has been empirically correlated with charging damage and, in turn, plasma uniformity depends on such design features as the magnetic field profile, source dimensions, wave propagation, and the electron heating mechanism. Much work remains before we can control plasma uniformity and relate uniformity to charging damage. Similarly, we find it ironic that low frequency bias voltages are used to minimize charging damage during anisotropic etching since the ion bombarding energy and the extent of atomic displacement damage is clearly higher at these lower frequencies. Again, the benefits of low frequency bias appear traceable to an improvement in plasma uniformity, but we suspect that this effect is strongly dependent on the details of plasma source design: for example, how near the walls lie to the edge of the wafer. It is also curious that the application of a bias voltage which increases the ion bombarding energy can reduce the extent of electrical damage. Is this simply a question of the faster etching rate leading to faster removal of damaged material or is there a more subtle explanation?

While plasma source design is primarily concerned with efficient plasma generation and ion energy control at low pressures to maintain critical dimensional control and high throughput while minimizing device damage, there are clearly fundamental limits to the control available. Generation of intense plasma necessarily implies larger currents to device wafers leading to an increased probability for charging damage. Intense plasma generation also implies large densities of excited electronic states that will radiate and

expose wafers to above band-gap radiation and thereby produce trapped charge and interface states. In electron cyclotron resonance plasmas, electron heating can be so efficient that "run away" occurs and electrons can gain more than 1 kV before impacting walls and generating potentially damaging x-rays. Finally, the control of ion bombardment energy is limited by the extent to which a broad distribution of internal energy states are created.

Plasma stability is an area of concern that we have not reviewed because of a paucity of measurements and theory. The consequences of plasma instability should be obvious: in large volume manufacturing, one can little afford a process that inexplicably deviates from its normal behavior. Plasma are notoriously non-linear and, as such, are a rich medium for instabilities and turbulence. Arguably, low pressure, magnetized plasmas are more prone to unstable operation than their unmagnetized counterparts since more modes can be excited and mode switching is prevalent (112,114,208,246-248) But, even for unmagnetized, conventional rf diodes, bistability and hysteresis have been observed and correlated with changes in etching rate (249,250). So unmagnetized sources such as the inductively coupled plasma, helical resonator, or surface wave excited plasma can be prone to instability. This is an area in need of careful experimental investigation and theoretical analysis.

To facilitate comparisons between plasma sources, we have relied on simple scaling relationships. Clearly these have limited validity and serve no more than to provide crude estimates. What we really need is a computer aided design tool with which plasma generation, transport, and stability in two or three dimensions can be simulated. In this manner, reactors and processes could be modified rapidly in software and a preliminary design selected prior to making a hardware prototype. While recent progress along these lines has been impressive, the field is too young to warrant an in-depth review. With rapid improvements in computational power, we look forward to increasingly sophisticated codes in the next few years and a continuing progression toward plasma sources that provide the level of process control needed to meet the demands of future materials processing applications.

## XI. ACKNOWLEDGEMENTS

The authors gratefully acknowledge A.J. Lichtenberg for his reading and comments on a draft of this manuscript, F.F. Chen for his comments on a draft of Sec. IV, C. W. Jurgensen for helpful discussions on ion energy control and etching anisotropy, and E. S. Aydil for a critical reading of the manuscript. We thank V. Vahedi for generating Figures 4, 5, and 7. The support of MAL by National Science Foundation Grant ECS-85-17363 and Department of Energy Grant DE-FG03-87-ER13727 is gratefully acknowledged.

## XI. SYMBOL DEFINITIONS

<b>B</b>	Magnetic field
<b>B<sub>0</sub></b>	DC magnetic field
<b>b</b>	Inductive or helical coil radius
<b>C<sub>0</sub></b>	Normalized, energy-flux-weighted, cumulative angular distribution function
<b>c</b>	Shield radius for helical resonator; Speed of light
<b><math>\Delta D_{da}</math></b>	Displaced atom density
<b><math>d_{eff}</math></b>	Effective plasma source size
<b>ER</b>	Etching rate
<b>E</b>	Electric field
<b><math>E_{rhp}</math></b>	Amplitude of RHP electric field
<b><math>E_{lhp}</math></b>	Amplitude of LHP electric field
<b><math>\tilde{E}</math></b>	Complex amplitude of rf electric field
<b><math>\epsilon_c</math></b>	Collisional energy lost per electron-ion pair created
<b><math>\epsilon_{exc}</math></b>	Effective excitation energy
<b><math>\epsilon_i</math></b>	Ion energy
<b><math>\epsilon_L</math></b>	Total energy lost per electron-ion pair created
<b>e</b>	Electronic charge
<b>eedf</b>	Electron energy distribution function
<b>I</b>	Current
<b><math>H_z</math></b>	Magnetic field induced by skin current in inductively coupled plasma
<b><math>h_L</math></b>	Ratio of plasma density at axial sheath edge to density in plasma center
<b><math>h_R</math></b>	Ratio of plasma density at radial sheath edge to density in plasma center
<b><math>I_0</math></b>	Modified Bessel function of the first kind
<b>iadf</b>	Ion angular distribution function
<b>iedf</b>	Ion energy distribution function
<b>ivdf</b>	Ion velocity distribution function
<b><math>J_m</math></b>	Bessel function of order <i>m</i>
<b>J</b>	Current density
<b><math>J_{iL}</math></b>	Ion current density at axial wall
<b><math>\tilde{J}</math></b>	Complex amplitude of rf current density
<b><math>\tilde{J}_a</math></b>	DC ion current density at the wafer platen
<b><math>\tilde{J}_a</math></b>	RF current density at the wafer platen
<b><math>\tilde{J}_b</math></b>	DC ion current density at the grounded surface
<b><math>\tilde{J}_b</math></b>	RF current density at the grounded surface
<b>K</b>	Second order rate constant
<b><math>K_{el}</math></b>	Elastic scattering rate constant
<b><math>K_{exc}</math></b>	Excitation rate constant
<b><math>K_{is}</math></b>	Ionization rate constant
<b><math>K_0</math></b>	Modified Bessel function of the second kind
<b><math>k_0</math></b>	Free space wavenumber, $\omega/c$
<b><math>k_r</math></b>	Spatially varying propagation constant, $k_0 K_r$ <sup>1/2</sup>
<b><math>k_z</math></b>	Wavenumber along $\hat{z}$
<b><math>k_{\perp}</math></b>	Wavenumber perpendicular to $\hat{z}$
<b><math>k_{\perp d}</math></b>	Transverse wavenumber for surface wave inside dielectric tube
<b><math>k_{\perp p}</math></b>	Transverse wavenumber for surface wave inside plasma
<b><math>k_{zh}</math></b>	Helical pitch wavenumber
<b>L</b>	Reactor length; Inductance
<b><math>L_d</math></b>	Characteristic length over which $V_d$ occurs
<b><math>\ell</math></b>	Helicon antenna length

LHP	Left hand circularly polarized
$M$	Ion mass
$m$	Electron mass; Azimuthal mode number
$N$	Neutral gas density
$\eta$	Number of turns in inductive coil
$n$	Plasma density
$n_p$	Plasma density downstream from source
$n_s$	Plasma charge density at sheath edge
$n_c$	Critical density
$P_{abs}$	Absorbed power
$P_{inc}$	Incident power
$P_{refl}$	Reflected power
$P_{trans}$	Transmitted power
$P_{\mu w}$	Microwave power
$P_w$	Power carried by wave
$p$	Neutral gas pressure
$p_{min}$	Minimum pressure needed to sustain ECR discharge
$R$	Reactor radius; Resistance
RHP	Right hand circularly polarized
$S_e$	Stochastic energy flux
$S_{ECR}$	ECR energy flux
$S_{ion}$	Ion energy flux
$S_r$	RHP energy flux
$S_{ohm}$	Ohmic energy flux
$SC_0$	Reactive sticking coefficient on bare surface
$s$	Sheath thickness
$T$	Neutral temperature
$T_e$	Electron temperature
$T_i$	Ion temperature
$T_{i\perp}$	Ion temperature perpendicular to the magnetic field
$T_{i\parallel}$	Ion temperature parallel to the magnetic field
TCP	Transformer coupled plasma
$t_{res}$	Time electron spends in resonance zone
$U_i$	Volume removed per unit ion bombarding energy
$U_n$	Volume removed per reacting neutral
$u_B$	Bohm velocity
$u_i$	Ion speed
$u_{is}$	Ion energy gained by acceleration through sheath potential, $V_s$
$u_{in}$	Ion speed normal to the surface
$u_{i\parallel}$	Radial ion speed (parallel to the surface)
$u_{i\perp}^{(0)}$	Directed ion radial speed
$u_{i\perp}^{(1)}$	Wave phase velocity, $\omega/k_z$
$u_{ph}$	Parallel electron velocity at resonance zone
$u_{res}$	Ion thermal speed
$u_{Ti}$	Electron thermal speed
$u_{Te}$	DC bias voltage of plasma with respect to wafer platen
$V_a$	RF voltage amplitude of plasma with respect to wafer platen
$\hat{V}_a$	DC bias voltage of plasma with respect to ground
$V_b$	RF voltage amplitude of plasma with respect to ground
$\hat{V}_b$	DC voltage of wafer platen with respect to ground
$V_{bias}$	Distributed sheath voltage
$V_d$	rf voltage amplitude between powered electrode and ground
$V_{rf}$	

$V_s$	Voltage between plasma and floating surface
$V_T$	Helical voltage at tap position
$\tilde{V}_{pw}$	rf voltage amplitude between plasma and wafer
$\bar{V}_{pw}$	dc voltage between plasma and wafer resulting from rf bias
$\Delta V_{FB}$	Flat-band voltage shift
$W_{ECR}$	Transverse energy gained from one pass through ECR resonance zone
$Z$	Impedance
$z_{res}$	Axial ECR resonance position
$\Delta z_{res}$	Width of ECR resonance zone
$z'$	Distance from resonance zone
$z_T$	Tap position on helical resonator coil
$\alpha$	Inverse scale length of cyclotron frequency near resonant zone, $\omega^{-1} \partial \omega_{ce} / \partial z'$
$\alpha_z$	Inverse of decay length along $\hat{z}$
$\beta$	Ratio of sheath potential to perpendicular ion temperature ( $V_s / T_{i\perp}$ )
$\delta_c$	Collisional skin depth
$\delta_p$	Collisionless skin depth
$\gamma(\theta, \epsilon_i)$	Differential ion flux
$\Gamma_e$	Electron flux
$\Gamma_i$	Ion flux
$\Gamma_{iL}$	Ion flux at axial wall
$\Gamma_n$	Neutral flux
$\kappa_d$	Relative dielectric constant for insulating tube
$\kappa_r$	Relative dielectric constant of plasma
$\lambda_{De}$	Electron Debye length
$\lambda_i$	Combined mean free path for ion-neutral momentum and charge exchange
$\lambda_r$	Wavelength for RHP wave in plasma, $2\pi/k_r$
$\lambda_z$	Wavelength along $\hat{z}$
$\mu_i$	Ion mobility
$\eta$	Microwave power attenuation coefficient, $\omega_{pe}^2 / (\omega c  \alpha )$
$\omega$	Angular frequency
$\omega_{ce}$	Electron cyclotron frequency
$\omega_{ci}$	Ion cyclotron frequency
$\omega_h$	Upper hybrid frequency
$\omega_L$	Lower hybrid frequency
$\omega_{pe}$	Electron plasma frequency
$\omega_{pi}$	Ion plasma frequency
$\omega_R$	RHP cut-off frequency
$\Phi$	Magnetic flux in inductive plasma; Spatially varying plasma potential
$\psi$	Pitch angle of helical coil in helical resonator
$\sigma$	DC conductivity of plasma
$\sigma_i$	Combined ion momentum and charge transfer cross section
$\bar{\sigma}$	Absorption or emission frequency
$\bar{\sigma}_0$	Rest absorption or emission frequency
$\Theta$	Surface coverage
$\nu_c$	Electron-neutral collision frequency
$\nu_{cT}$	Sum of electron-neutral and electron-ion collision frequencies
$\nu_{LD}$	Effective collision frequency for Landau damping
$\nu_T$	Total effective collision frequency
$\xi$	Ratio of directed velocity to sheath velocity, $2u_{i\perp}^{(0)} / u_{is}$
$\zeta$	Ratio of helicon phase velocity to electron thermal speed, $\omega / (k_z u_{Te})$

## XII. REFERENCES

- 1 R. B. Fair, *Proceedings of the IEEE* **78**, 1687 (1990).
- 2 J. M. Cook and K. G. Donohoe, *Solid State Tech.* **34**, 119 (1991).
- 3 J. Asmussen, *J. Vac. Sci. Technol. A* **7**, 883 (1989).
- 4 R. R. Burke and C. Pomot, *Solid State Technol.* **31**, 67 (1988).
- 5 K.-H. Kretschmer, K. Matl, G. Lorenz, I. Kessler, and B. Dumbacher, *Solid State Technol.* **33**, 53 (1990).
- 6 W. M. Holber, in "Handbook of Ion Beam Processing Technology," edited by J. J. Cuomo, S. M. Rossnagel, and H. R. Kaufman, Noyes Publications (Park Ridge, NJ, 1989), p. 21.
- 7 D. Dane, P. Gadgil, T. D. Mantei, M. A. Carlson, and M. E. Weber, *J. Vac. Sci. Technol. B* **10**, 1312 (1992).
- 8 A. Hall and K. Nojiri, *Solid State Technol.*, May 1991, p. 107.
- 9 Y. H. Lee, Z. H. Zhou, D. A. Danner, P. M. Fryer, and J. M. Harper, *J. Appl. Phys.* **68**, 5329 (1990).
- 10 J. Pelletier and M. J. Cooke, *J. Vac. Sci. Technol.* **7**, 59 (1989).
- 11 T. Ono, M. Oda, C. Takahashi, and S. Matsuo, *J. Vac. Sci. Technol. B* **4**, 696 (1986).
- 12 H. Shindo, T. Hashimoto, F. Amasaki, and Y. Horiike, *Jpn. J. Appl. Phys.* **29**, 2641 (1990).
- 13 H. Uetake, T. Matsuura, T. Ohmi, J. Murota, K. Fukuda, and N. Mikoshiba, *Appl. Phys. Lett.* **57**, 596 (1990).
- 14 G. Fortuno-Wiltshire, *J. Vac. Sci. Technol. A* **9**, 2356 (1991).
- 15 C. Constantine, D. Johnson, S. J. Pearton, U. K. Chakrabarti, A. B. Emerson, W. S. Hobson, and A. P. Kinsella, *J. Vac. Sci. Technol. B* **8**, 596 (1990).
- 16 S. J. Pearton, F. Ren, J. R. Lothian, T. R. Fullowan, R. F. Kopf, U. K. Chakrabarti, S. P. Hui, A. B. Emerson, R. L. Kostelak, and S. S. Pei, *J. Vac. Sci. Technol. B* **9**, 2487 (1991).
- 17 K. D. Choquette, R. C. Wetzal, and R. S. Freund, (preprint).
- 18 J. M. Cook, D. E. Ibbotson, P. D. Foo, and D. L. Flamm, *J. Vac. Sci. Technol. A* **8**, 1820 (1990).
- 19 S. Tachi, K. Tsujimoto, S. Arai, and T. Kure, *J. Vac. Sci. Technol. A* **9**, 796 (1991).
- 20 D. X. Ma, T. A. Lin, and C. H. Chen, *J. Vac. Sci. Technol. A* **10**, 1217 (1992).
- 21 W. F. Marx, D. X. Ma, C. H. Chen, *J. Vac. Sci. Technol. A* **10**, 1232 (1992).
- 22 S. M. Gorbatkin, L. A. Berry, and J. Swyers, *J. Vac. Sci. Technol. A* **10**, 1295 (1992).
- 23 P. K. Gadgil, D. Dane, and T. D. Mantei, *J. Vac. Sci. Technol. A* **10**, 1303 (1992).
- 24 K. W. Whang, S. H. Lee, and H. J. Lee, *J. Vac. Sci. Technol. A* **10**, 1307 (1992).
- 25 S. J. Pearton, U. K. Chakrabarti, W. S. Hobson, C. R. Abernathy, A. Katz, F. Ren, T. R. Fullowan, and A. P. Perley, *J. Electrochem. Soc.* **139**, 1763 (1992).
- 26 K. Suzuki, K. Ninomiya, S. Nishimatsu, and S. Okudaira, *J. Vac. Sci. Technol. B* **3**, 1025 (1985).
- 27 K. Suzuki, S. Okudaira, and I. Kanomata, *J. Electrochem. Soc.* **126**, 1024 (1979).
- 28 S. Samukawa, M. Sasaki, and Y. Suzuki, *J. Vac. Sci. Technol.* **8**, 1062 (1990).
- 29 S. Samukawa, S. Mori, and M. Sasaki, *Jpn. J. Appl. Phys.* **29**, 792 (1990).
- 30 S. Samukawa, Y. Suzuki, and M. Sasaki, *Appl. Phys. Lett.* **57**, 403 (1990).

- 31 S. Samukawa, M. Sasaki, and Y. Suzuki, *J. Vac. Sci. Technol.* **8**, 1192, (1990).
- 32 S. Samukawa, T. Toyosato, and E. Wani, *J. Vac. Sci. Technol. B* **9**, 1471 (1991).
- 33 D.A. Carl, D.W. Hess, and M.A. Lieberman, *J. Appl. Phys.* **68**, 1859 (1990). vol 68, no. 4, p. 1859 (1990).
- 34 F. Plais, B. Agius, F. Abel, J. Siejka, M. Puech, G. Ravel, P. Alnot, and N. Proust, *J. Electrochem. Soc.* **139**, 1489 (1992).
- 35 M. Kitagawa, K. Setsune, Y. Manabe, and T. Hirao, *Jpn. J. Appl. Phys.* **27**, 2026 (1988).
- 36 T. Hirao, K. Setsune, M. Kitagawa, Y. Manabe, K. Wasa, and S. Kohiki, *Jpn. J. Appl. Phys.* **26**, L544 (1987).
- 37 Y. Manabe and T. Mitsuyu, *J. Appl. Phys.* **66**, 2475 (1989).
- 38 C. S. Pai, J. F. Miner, and P. D. Foo, *J. Electrochem. Soc.* **139**, 850 (1992).
- 39 R. D. Knox, V. L. Dalal, and O. A. Popov, *J. Vac. Sci. Technol. A* **9**, 474 (1991).
- 40 J. C. Barbour, H. J. Stein, O. A. Popov, M. Yoder, and C. A. Outten, *J. Vac. Sci. Technol. A* **9**, 480 (1991).
- 41 M. Kitagawa, N. Matsuo, G. Fuse, H. Iwasaki, A. Yoshida, and T. Hirao, *Jpn. J. Appl. Phys.* **27**, L2139 (1988).
- 42 N. Cheung, *Nucl. Instr. Methods Phys. Res.* **B55**, 811 (1991).
- 43 X. Y. Qian, N. W. Cheung, M. A. Lieberman, S. B. Felch, R. Brennan, and M. I. Current, *Appl. Phys. Lett.* **59**, 348 (1991).
- 44 X. Y. Qian, D. Carl, J. Benasso, N. W. Cheung, M. A. Lieberman, I. G. Brown, J. E. Galvin, R. A. MacGill, and M. I. Current, *Nucl. Instr. Methods Phys. Res.* **B55**, 844 (1991).
- 45 M. H. Kiang, M. A. Lieberman, N. W. Cheung, and X. Y. Qian, *Appl. Phys. Lett.* **60**, 2767 (1992).
- 46 N. Kondo and Y. Nanishi, *Jpn. J. Appl. Phys.* **28**, L7 (1989).
- 47 S. Sugata, A. Takamori, N. Takado, K. Asakawa, E. Miyauchi, and H. Hashimoto, *J. Vac. Sci. Technol. B* **6**, 1087 (1988).
- 48 Z. Lu, M.T. Schmidt, D. Chen, R.M. Osgood, Jr., W.M. Holber, D.V. Podlesnik and J. Forster, *Appl. Phys. Lett.* **58**, 1143(1991).
- 49 K. D. Choquette, M. Hong, R. S. Freund, J. P. Mannaerts, and R. C. Wetzel, (preprint).
- 50 G. M. Mikhailov, P. V. Bulkin, S. A. Khudobin, A. A. Chumakov, and S. Y. Shapoval, *Vacuum* **43**, 199 (1992).
- 51 M. Delfino, S. Salimian, and D. Hodul, *J. Appl. Phys.* **70**, 1712 (1991).
- 52 M. Delfino, S. Salimian, D. Hodul, A. Ellingboe, and W. Tsai, *J. Appl. Phys.* **71**, 1001 (1992).
- 53 Z. Lu, M. T. Schmidt, R. M. Osgood, W. M. Holber, and D. V. Podlesnik, *J. Vac. Sci. Technol. A* **9**, 1040 (1991).
- 54 A. Kishimoto, I. Suemune, K. Hamaoka, T. Kouji, Y. Honda, and M. Yamanishi, *Jpn. J. Appl. Phys.* **29**, 2273 (1990).
- 55 H. Yamada, *J. Appl. Phys.* **65**, 775 (1989).
- 56 K. Nakashima, M. Ishii, I. Tajima, and M. Yamamoto, *Appl. Phys. Lett.* **58**, 2663 (1991).
- 57 T. Shibata, Y. Nanishi, and M. Fujimoto, *Jpn. J. Appl. Phys.* **29**, L1181 (1990).
- 58 H. Hirayama and T. Tatsumi, *J. Appl. Phys.* **66**, 629 (1989).

- 59 M. Ishii, K. Nakashima, I. Tajima, and M. Yamamoto, *Appl. Phys. Lett.* **58**, 1378 (1991).
- 60 T. Takeshita, T. Unagami, and O. Kogure, *Jpn. J. Appl. Phys.* **27**, L2118 (1988).
- 61 K. Miyake, S. Kimura, T. Warabisako, H. Sunami, and T. Tokuyama, *J. Vac. Sci. Technol. A* **2**, 496 (1984).
- 62 D. A. Carl, D. W. Hess, and M. A. Lieberman, *J. Vac. Sci. Technol. A* **8**, 2924 (1990).
- 63 D. A. Carl, D. W. Hess, M. A. Lieberman, T. D. Nguyen, and R. Gronsky, *J. Appl. Phys.* **70**, 3301 (1991).
- 64 R.A. Gottscho, *Phys. Rev. A* **36**, 2233 (1987).
- 65 A. von Engel, "Ionized Gases," Clarendon Press (1965).
- 66 C. W. Jurgensen, *J. Appl. Phys.* **64**, 590 (1988).
- 67 R. Warren, *Phys. Rev.* **98**, 1658 (1955).
- 68 B. Chapman, *Glow Discharge Processes*, John Wiley and Sons (New York, 1980).
- 69 R. T. Farouki, M. Dalvie, L. F. Pavarino, *J. Appl. Phys.* **68**, 6106 (1990).
- 70 D. H. Economou, D. R. Evans, and R. C. Alkire, *J. Electrochem. Soc.* **135**, 756 (1988).
- 71 M. A. Lieberman, *IEEE Trans. Plasma Sci.* **16**, 638 (1988).
- 72 M. A. Lieberman *IEEE Trans. Plasma Sci.* **17**, 338 (1989).
- 73 V. A. Godyak and N. Sternberg *Phys. Rev. A* **42**, 2299 (1990).
- 74 V. A. Godyak and R. B. Piejak, *Phys. Rev. Lett.* **65**, 996 (1990).
- 75 G. A. Hebner, J. T. Verdeyen, and M. J. Kushner, *J. Appl. Phys.* **63**, 2226 (1988).
- 76 V.M. Donnelly, D.L. Flamm, W.C. Dautremont-Smith, and D.J. Werder, *J. Appl. Phys.* **55**, 242 (1984).
- 77 C. P. Chang, D. L. Flamm, D. E. Ibbotson, and J. A. Mucha, *J. Vac. Sci. Technol. B* **6**, 524 (1988).
- 78 W. C. Dautremont-Smith, R. A. Gottscho, and R. J. Schutz, "Plasma Processing: Mechanisms and Applications", in *Semiconductor Materials and Process Technology Handbook*, edited by G. E. McGuire, (Noyes, Park Ridge, NJ, 1988), chap. 5.
- 79 A. S. Bergendahl, D. V. Horak, P. E. Bakeman, and D. J. Miller, *Semicond. Int.*, Sept. 1990, p. 94.
- 80 Lieberman, M.A., Lichtenberg, A.J. and Savas, S.E. (1990). *IEEE Trans. Plasma Sci.* **19**, 189.
- 81 A. V. Lukyanova, A. T. Rakhimov, and N. V. Suetin, *IEEE Trans. on Plasma Sci.* **19**, 197 (1991).
- 82 R. W. Boswell, "A Study of Waves in Gaseous Plasma," Ph.D. Thesis, Flinders University of South Australia, July 1970.
- 83 F. F. Chen, *Laser and Part. Beams*, **7**, 551 (1989).
- 84 A. Komori, T. Shoji, K. Miyamoto, J. Kawai, and K. Kawai, *Phys. Fluids B* **3**, 893 (1991).
- 85 P. K. Lowenhardt, B. D. Blackwell, R. W. Boswell, G. D. Conway, and S. M. Hamberger, *Phys. Rev. Lett.* **67**, 2792 (1991).
- 86 F. F. Chen, *Plasma Phys. Controlled Fusion* **33**, 339 (1991).
- 87 S. M. Gorbatkin and L. A. Berry, *J. Vac. Sci. Technol. A* **10**, 3104 (1992).
- 88 H. Hoga, T. Orita, T. Yokoyama, and T. Hayashi, *Jpn. H. Appl. Phys.* **30**, 3169 (1991).
- 89 J. H. Ingold, in "Gaseous Electronics," edited by M. N. Hirsh and H. J. Oskam, Academic Press (Orlando, FL, 1978), p. 19.

- 90 T. Nakano, N. Sadeghi, and R. A. Gottscho, *Appl. Phys. Lett.* **58**, 458 (1991).
- 91 J. E. Stevens, Y. C. Huang, R. L. Jarecki, and J. L. Cecchi, *J. Vac. Sci. Technol.* **A10**, 1270 (1992).
- 92 M. D. Bowden, T. Okamoto, F. Kimura, H. Muta, T. Sakoda, K. Muraoka, M. Maeda, Y. Manabe, M. Kitagawa, and T. Kimura, (preprint).
- 93 E. Eggarter, *J. Chem. Phys.* **62**, 833 (1975).
- 94 L.R. Peterson and J.E. Allen, Jr., *J. Chem. Phys.* **56**, 6068 (1972).
- 95 M. Hayashi, Report IPPJ-AM-19, Inst. Nucl. Phys., Nagoya U. (1981).
- 96 Tonks, L. and Langmuir, I. (1929). *Phys. Rev.* **34**, 876.
- 97 W. Schottky (1924). *Phys. Zeits.* **25**, 635.
- 98 Smirnov, B.M. (1981). *Physics of Weakly Ionized Gases*, Mir, Moscow, USSR, p. 216-217.
- 99 V.A. Godyak, "Soviet Radio Frequency Discharge Research", Delphic Associates, Inc., (Falls Church, VA, 1986), p. 86-90.
- 100 Godyak, V.A. and Maximov, V.N. (1977). *Vestnik Moskovskoy Universiteta, ser. Fiz. Astr.* **18**, 51.
- 101 N. Sadeghi, T. Nakano, D. J. Trevor, and R. A. Gottscho, *J. Appl. Phys.* **70**, 2552 (1991); N. Sadeghi, T. Nakano, D. J. Trevor, and R. A. Gottscho, *J. Appl. Phys.* **71**, 3648 (1992).
- 102 Thornton, J.A. and Penfold, A.S. (1978). In *Thin Film Processes*, ed. by J.L. Vossen and W. Kern, Academic Press, New York, NY.
- 103 Rossnagel, S.M. and Kaufman, H.R. (1986). *J. Vac. Sci. Technol.* **4**, 1822.
- 104 Wendt, A.R. and Lieberman, M.A. (1990). *J. Vac. Sci. Technol.* **A8**, 902.
- 105 Goree, J. and Sheridan, T.E. (1991). *Appl. Phys. Lett.* **59**, 1052.
- 106 Misium, G.R., Lichtenberg, A.J., and Lieberman, M.A. (1989). *J. Vac. Sci. Technol.* **A7**, 1007.
- 107 Piejak, R.B., Godyak, V.A., and Alexandrovich, B.M. (1992). To appear in *Plasma Sources Sci.*
- 108 S. C. Brown, *Basic Data of Plasma Physics*, MIT Press and John Wiley & Sons, Inc. (New York, 1959).
- 109 F. F. Chen, *Introduction to Plasma Physics*, Plenum (New York, 1974).
- 110 J. Spencer, "Recent Advances in ECR Plasma Sources", as reported at the Plasma Etch Users' Group Monthly Meeting, Varian Research Center, Palo Alto, CA, April 9, 1992
- 111 A. S. Yapsir, G. Fortuno-Wiltshire, J. P. Gambino, R. H. Kastl, and C. C. Parks, *J. Vac. Sci. Technol.* **A 8**, 2939 (1990).
- 112 S. M. Gorbatkin, L. A. Berry, and J. B. Roberto, *J. Vac. Sci. Technol.* **A 8**, 2893 (1990).
- 113 S. M. Rossnagel, S. J. Whitehair, C. R. Guarnieri, and J. J. Cuomo, *J. Vac. Sci. Technol.* **A 8**, 3113 (1990).
- 114 S. Samukawa, T. Nakamura, and A. Ishitani, *Jpn. J. Appl. Phys.* **31**, L594 (1992).
- 115 C. G. Montgomery, R. H. Dicke, and E. M. Purcell, "Principles of Microwave Circuits," (Dover, New York, 1965).
- 116 Mauel, M. (1992). Private communication.
- 117 Williamson, M.C., Lichtenberg, A.J. and Lieberman, M.A. (1992). To appear in *J. Appl. Phys.*
- 118 Mantai, T.D. and Ryle, T.E. (1991). *J. Vac. Sci. Technol.* **B9**, 29.
- 119 Mantai, T.D. and Dhole, S. (1991). *J. Vac. Sci. Technol.* **B9**, 26.

- 120 Samukawa, S., Mori, S. and Sasaki, M. (1991). *J. Vac. Sci. Technol.* A9, 85.
- 121 M. Pichot, A. Durandet, J. Pelletier, Y. Arnal, and L. Vallier, *Rev. Sci. Instrum.* 59, 1072 (1988).
- 122 Root, J. and Asmussen, J. (1985). *Rev. Sci. Instrum.* 56, 154.
- 123 Jaeger, F., Lichtenberg, A.J., and Lieberman, M.A. (1972). *Plasma Phys.* 14, 1073.
- 124 Ginzburg, (1964). *The Propagation of Electromagnetic Waves in Plasmas*, Pergamon Press, Oxford, England.
- 125 Budden, K.G. (1966). *Radio Waves in the Ionosphere*, Cambridge University Press, England, pp. 474-479.
- 126 Stix, T. (1962). *The Theory of Plasma Waves*, McGraw-Hill, New York, NY.
- 127 Born, M. and Wolf, E. (1980). *Principles of Optics*, Sixth Edition, Pergamon Press, Oxford, England, Appendix II.
- 128 Allis, W.P., Buchsbaum, S.J. and Bers, A. (1963). *Waves in Anisotropic Plasmas*, MIT Press, Cambridge, MA.
- 129 Lichtenberg, A.J. and Lieberman, M.A. (1981). *Regular and Stochastic Motion*, Springer-Verlag, New York, NY.
- 130 Tanaka, M., Nishimoto, R., Higashi, S., Harada, N., Ohi, T., Komori, A. and Kawai, Y. (1991). *J. Phys. Soc. Japan* 60, 1600.
- 131 Boswell, R.W. (1970). *Phys. Lett.* 33A, 457.
- 132 Bowers, R., Legendy, C., and Rose, F.E. (1961). *Phys. Rev. Lett.* 7, 339.
- 133 Harding, G.N. and Thonemann, P.C. (1965). *Proc. Phys. Soc.* 85, 301.
- 134 Davies, B.J. (1970). *Plasma Phys.* 4, 43.
- 135 Chen, F.F. (1992). *J. Vac. Sci. Technol.* A10, 1389.
- 136 Chen, F.F. and Decker, C.D. (1992). *Plasma Phys. Controlled Fusion* 34, 635.
- 137 Boswell, R.W. and Henry, D. (1985). *Appl. Phys. Lett.* 47, 1095.
- 138 Perry, A.J. and Boswell, R.W. (1989). *Appl. Phys. Lett.* 55, 148.
- 139 Perry, A.J., Vender, D., and Boswell, R.W. (1991). *J. Vac. Sci. Technol. B* 9, 310.
- 140 P. K. Loewenhardt, B. Zhang, B. D. Blackwell, and R. W. Boswell, (preprint, 1992)
- 141 R. H. Lovberg, in "Plasma Diagnostic Techniques," edited by R. H. Huddleston and S. L. Leonard, (Academic Press, New York, 1965), p. 69.
- 142 Boswell, R.W. (1984). *Plasma Phys. Controlled Fusion* 26, 1147.
- 143 K. P. Giapis, N. Sadeghi, J. Margot, R. A. Gottscho, and T. C. Lee, submitted *J. Appl. Phys.* (1992)
- 144 Boswell, R.W. and Porteous, R.K. (1987). *Appl. Phys. Lett.* 50, 1130.
- 145 Chen, F.F. (1992a). Private communication.
- 146 Conn, R. (1992). As reported at the Plasma Etch Users' Group Monthly Meeting, Varian Research Center, Palo Alto, CA, April 9.
- 147 Hittorf, W. (1884). *Wiedemanns Ann. d. Physik.* 21, 90.
- 148 Thomson, J.J. (1927). *Philos. Mag.* 4, 1128.
- 149 Townsend, J.S. and Donaldson, R. H. (1929). *Philos. Mag.* 8, 605.
- 150 McKinnon, K.A. (1929). *Philos. Mag.* 8, 605.

- 151 Eckert, H.U. (1986). *Proc. 2nd Intl. Conf. on Plasma Chem. and Technol.*, H. Boenig, ed., Technomic Publ., Lancaster, PA.
- 152 Keller, J. H., Barnes, M.S., and Forster, J.C. (1990). 43rd Annual Gaseous Electronics Conference, Champaign-Urbana, IL, 16-19 Oct. 1990, Abstract NA-5.
- 153 Lam Research Corporation (1992). Technical Note TN-003.
- 154 Oldham, W.G., and Schwarz, S.E., *An Introduction to Electronics* Holt, Reinhart and Winston, New York, 1972.
- 155 Denneman, J.W. (1990). *J. Phys. D: Appl. Phys.* 23, 293.
- 156 Amorim, J., H.S. Maciel, and Sudano, J.P. (1991). *J. Vac. Sci. Technol.* B9, 362.
- 157 Macalpine, W.W. and Schildknecht, R.O. (1959). *Proc. Inst. Radio Engrs.*, December, 2099.
- 158 Steinberg, G.N. and Steinberg, A.R. (1983). U.S. Patent No. 4,368,092 issued Jan. 11, 1983.
- 159 Flamm, D.L., Ibbotson, D.E., and Johnson, W.L., U.S. Patent No. 4,918,031 issued April 17, 1990.
- 160 Flamm, D.L. (1989). As presented at the International Union for Pure and Applied Chemistry, 9th International Symposium on Plasma Chemistry, Pungochiuso, Italy, Sept. 7-15.
- 161 Cook, J.M., Ibbotson, D.E., and Flamm, D.L. (1990). *J. Vac. Sci. Technol.* B8, 1.
- 162 M. A. Lieberman, A. J. Lichtenberg, and D. L. Flamm, Memorandum No. UCB/ERL M90/10, Electronics Research Laboratory, College of Engineering, University of California, Berkeley, CA, Feb 5 (1990).
- 163 Bletzinger, P. (1991). 44th Annual Gaseous Electronics Conference, 22-25 October 1991, Albuquerque, NM, Abstract RB-1, p. 201.
- 164 Prototech Research (1992). As presented at the Plasma Etch Users' Group Monthly Meeting, Varian Research Center, Palo Alto, CA, April 9.
- 165 Pierce, J.R. (1950). *Traveling Wave Tubes*, D. Van Nostrand, New York, NY, Cha. 3.
- 166 Welton, R.F., Thomas, E.W., Feeney, R.K., and Moran, T.F. (1991). *Measurement Sci. Technol.* 2, 242.
- 167 Smullin, L.D. and Chorney, P. (1958). *Proc. Inst. Radio Engrs.* 46, 360.
- 168 Trivelpiece, A.W. and Gould, R.W. (1959). *J. Appl. Phys.* 30, 1784.
- 169 Tuma, D.R. (1970). *Rev. Sci. Instrum.* 41, 1519.
- 170 Moisan, M. and Zakrzewski, Z. (1991). *J. Phys. D: Appl. Phys.* 24, 1025.
- 171 Paquin, L., Masson, D., Wertheimer, M. and Moisan, M. (1985). *Can. J. Phys.* 63, 831.
- 172 Claude, R., Moisan, M., Wertheimer, M.R. and Zakrzewski, Z. (1987). *Appl. Phys. Lett.* 50, 1797.
- 173 Sauve, G., Moisan, M., Paraszczak, J., and Heindenreich, J. (1988). *Appl. Phys. Lett.* 53, 470.
- 174 Margot, J. and Moisan, M. (1991). *J. Phys. D: Appl. Phys.* 24, 1765.
- 175 T. M. Mayer and R. A. Barker, *J. Vac. Sci. Technol.* 21, 757 (1982).
- 176 J. W. Coburn and H. F. Winters, *J. Appl. Phys.* 50, 3189 (1979).
- 177 H. F. Winters, J. W. Coburn, and T. J. Chuang, *J. Vac. Sci. Technol. B* 1, 469 (1983).
- 178 U. Gerlach-Meyer, J. W. Coburn, and E. Kay, *Surf. Sci.* 103, 177 (1981).
- 179 T. M. Mayer, R. A. Barker, L. J. Whitman, *J. Vac. Sci. Technol.* 18, 349 (1981).
- 180 R. A. Barker, T. M. Mayer, and W. C. Pearson, *J. Vac. Sci. Technol. B* 1, 37 (1983).

- 181 T. M. Mayer and R. A. Barker, *J. Electrochem. Soc.* **129**, 585 (1982).
- 182 H. Gokan and S. Esho *J. Electrochem. Soc.* **131**, 131 (1984).
- 183 E. S. G. Shaqfeh and C. W. Jurgensen, *J. Appl. Phys.* **66**, 4664 (1989).
- 184 H. Nogami, Y. Ogahara, S. Mashiro, T. Tsukada, and D. I. C. Pearson, 39th Spring Meeting of the Japanese Society of Applied Physics, 30p-ZS-8 (1992); S. Mashiro, H. Nogami, Y. Ogahara, T. Tsukada, and D. I. C. Pearson, *loc cit*, 29-NC-3 (1992).
- 185 W. M. Holber and J. Forster, *J. Vac. Sci. Technol. A* **8**, 3720 (1990).
- 186 J. Liu, G. L. Huppert, and H. H. Sawin, *J. Appl. Phys.* **68**, 3916 (1990).
- 187 R. Koslover and R. McWilliams, *Rev. Sci. Instr.* **57**, 2441 (1986).
- 188 E. A. Den Hartog, H. Persing, J. S. Hamers, and R. C. Woods, 44th Annual Gaseous Electronics Conference, Albuquerque, NM, October 1991, Abstract DA-1.
- 189 T. Nakano, N. Sadeghi, D. J. Trevor, R. A. Gottscho, and R. W. Boswell, *J. Appl. Phys.* (in press, 1992).
- 190 T. Nakano, R. A. Gottscho, N. Sadeghi, D. J. Trevor, R. W. Boswell, A. J. Perry, T. C. Lee, K. P. Giapis, and J. Margot, *Jpn. Soc. Appl. Phys.* **61**, 711 (1992).
- 191 F. F. Chen, in "Plasma Diagnostic Techniques," edited by R. H. Huddleston and S. L. Leonard, (Academic Press, New York, 1965), p. 113.
- 192 N. Hershkowitz, in *Plasma Diagnostics*, vol. 1, Ed. by O. Auciello and D.L. Flamm, Academic Press, New York (1989).
- 193 J. D. Swift and M. J. R. Schwar, "Electrical Probes for Plasma Diagnostics," (Elsevier, New York, 1969).
- 194 V. A. Godyak, R. B. Piejak, and B.M. Alexandrovich, *Plasma Sources Sci. Technol.* **1**, 36 (1992).
- 195 R. K. Porteous, H.-M. Wu, and D. B. Graves, *J. Phys. D.* (submitted).
- 196 M. Matsuoka and K. Ono, *Appl. Phys. Lett.* **50**, 1864 (1987).
- 197 M. Matsuoka and K. Ono, *J. Vac. Sci. Technol. A* **6**, 25 (1988).
- 198 P. Reinke, W. Jacob, and W. Moller, *Proc. NATO-ASI on Diamond and Diamond-Like Films and Coatings*, edited by R. E. Clausing, L. L. Harton, F. C. Augus, and P. Koidl, NATO-ASI Series B: Physics, Volume 266, Plenum, New York 1991.
- 199 P. Reinke, S. Schetz, W. Jacob, and W. Moller, *J. Vac. Sci. Technol. A* **10**, 434 (1992).
- 200 E. A. Den Hartog, H. Persing, and R. C. Woods, *Appl. Phys. Lett.* **57**, 661 (1990).
- 201 R. C. Woods, R. L. McClain, L. J. Mahoney, E. A. Den Hartog, H. Persing, and J. S. Hamers, *SPIE Vol. 1594*, 366 (1991).
- 202 S. Samukawa, Y. Nakagawa, and K. Ikeda, *Jpn. J. Appl. Phys.* **29**, 88 (1990).
- 203 C. Charles, R. W. Boswell, and R. K. Porteous, *J. Vac. Sci. Technol. A* **10**, 398 (1992).
- 204 M. A. Hussein, G. A. Emmert, N. Hershkowitz, and R. C. Woods, *J. Vac. Sci. Technol.* (in press, 1992).
- 205 H. Fujita, Y. Okuno, Y. Ohtsu, and S. Yagura, *J. Appl. Phys.* **67**, 6114 (1990).
- 206 V. E. Golant, A. P. Zhilinsky, and I. E. Sakharov, *Fundamentals of Plasma Physics*, John Wiley & Sons (New York, 1977).
- 207 K. Shirai and S. Gonda, *J. Appl. Phys.* **68**, 4258 (1990).

- 208 S. Iizuka and N. Sato, *J. Appl. Phys.* **70**, 4165 (1991).
- 209 H.R. Koenig and L.I. Maissel, *IBM J. Res. Dev.* **14**, 168 (1970).
- 210 J.L. Vossen, *J. Electrochem. Soc.* **126**, 2345 (1979).
- 211 V.A. Godyak, *Sov. J. Plasma Phys.* **2**, 78 (1976).
- 212 K. Kohler, J. W. Coburn, D. E. Horne, E. Kay, and J. H. Keller, *J. Appl. Phys.* **57**, 59 (1985).
- 213 J.W. Coburn and E. Kay, *J. Appl. Phys.* **43**, 4965 (1972).
- 214 C. M. Horwitz, *J. Vac. Sci. Technol. A* **1**, 60 (1983).
- 215 G.Y. Yeom, J.A. Thornton, and M.J. Kushner, *J. Appl. Phys.* **65**, 3825 (1989).
- 216 A.M. Pointu, *Appl. Phys. Lett.* **50**, 1047 (1987).
- 217 M.A. Lieberman, *J. Appl. Phys.* **65**, 4186 (1989).
- 218 M. V. Alves, M. A. Lieberman, V. Vahedi, and C. K. Birdsall, *J. Appl. Phys.* **69**, 3823 (1991).
- 219 M. A. Lieberman and S. E. Savas, *J. Vac. Sci. Technol. A* **8**, 1632 (1990).
- 220 T. Hara, J. Hiyoshi, and H. Hamanaka, M. Sasaki, F. Kobayashi, K. Ukai, and T. Okada, *J. Appl. Phys.* **67**, 2836 (1990).
- 221 G. Washidzu, T. Hara, J. Hiyoshi, M. Sasaki, Y. Suzuki, and K. Ukai, *Jpn. J. Appl. Phys.* **30**, 1045 (1991).
- 222 A. S. Yapsir, G. S. Oehrlein, G. Fortuno-Wiltshire, and J. C. Tsang, *Appl. Phys. Lett.* **57**, 590 (1990);
- 223 A. J. Watts and W. J. Varhue, *Appl. Phys. Lett.* **61**, 549 (1992).
- 224 C. T. Gabriel and J. P. McVittie, *Solid State Technol.*, June 1992, p. 81;
- 225 K. Tsunokuni, K. Nojiri, S. Kuboshima, K. Hirobe, Ext. Abstr. 19th Conf. Solid State Dev. and Materials, Tokyo 1987, p. 195.
- 226 S.M. Sze, *Semiconductor Devices*, John Wiley (New York 1985).
- 227 S. B. Felch, S. Sa'imian, and D. T. Hodul, *J. Vac. Sci. Technol. B* **10**, 1320 (1992).
- 228 P. H. Singer, *Semiconductor Int.*, May 1982, p. 78.
- 229 C. T. Gabriel, *J. Vac. Sci. Technol. B* **9**, 370 (1991).
- 230 S. Samukawa, *Jpn. J. Appl. Phys.* **29**, 980 (1990).
- 231 S. Samukawa, *Jpn. J. Appl. Phys.* **30**, L1902 (1991);
- 232 T. Namura, H. Okada, Y. Naitoh, Y. Todokoro, and M. Inoue, *Jpn. J. Appl. Phys.* **29**, 2251 (1990).
- 233 S. Samukawa, *Jpn. J. Appl. Phys.* **30**, 3154 (1991);
- 234 K. Tsunokuni, K. Nojiri, M. Nawata, Ext. Abstr. 38th Mtg. Jpn. Soc. Appl. Phys. 1991, p. 499.
- 235 C. B. Zarowin, *J. Vac. Sci. Technol. A* **2**, 1537 (1984).
- 236 S. Miyake, W. Chen, and T. Ariyasu, *Jpn. J. Appl. Phys.* **29**, 2491 (1990).
- 237 D. J. DiMaria, L. M. Ephrath, and D. R. Young, *J. Appl. Phys.* **50**, 4015 (1979).
- 238 L. M. Ephrath and D. J. DiMaria, *Solid State Technol.*, April 1981.
- 239 D. A. Buchanan and G. Fortuno-Wiltshire, *J. Vac. Sci. Technol. A* **9**, 804 (1991).
- 240 T. Yunogami, T. Mizutani, K. Suzuki, and S. Nishimatsu, *Jpn. J. Appl. Phys.* **28**, 2172 (1989).

- 241 T. Yunogami, T. Mizutani, K. Tsujimoto, and K. Suzuki, *Jpn. J. Appl. Phys.* **29**, 2269 (1990).
- 242 T. J. Castagna, J. L. Shohet, K. A. Ashtiani, and N. Hershkowitz, *Appl. Phys. Lett.* **23**, 2856 (1992); *J. Vac. Sci. Technol. A* **10**, 1325 (1992).
- 243 S. Meikle and Y. Hatanaka, *Appl. Phys. Lett.* **54**, 1648 (1989).
- 244 J. L. Cecchi, J. E. Stevens, R. L. Jarecki, Jr., and Y. C. Huang, *J. Vac. Sci. Technol. B* **9**, 318 (1991).
- 245 J. P. Booth and N. Sadeghi, *J. Appl. Phys.* **70**, 611 (1992).
- 246 D. A. Carl, M. C. Williamson, M. A. Lieberman, and A. J. Lichtenberg, *J. Vac. Sci. Technol. B* **9**, 339 (1991).
- 247 P. K. Shufflebotham and D. J. Thomson, *J. Vac. Sci. Technol. A* **8**, 3713 (1990).
- 248 R. A. Dandl and G. E. Guest, *J. Vac. Sci. Technol. A* **9**, 3119 (1991).
- 249 E. S. Aydil and D. J. Economou, *J. Appl. Phys.* **69**, 109 (1991).
- 250 P. A. Miller and K. E. Greenberg, *Appl. Phys. Lett.* **60**, 2859 (1992).

### XIII. FIGURE CAPTIONS

1. Capacitive RF discharges; (a) plane parallel geometry; (b) coaxial ("hexode") geometry.
2. RF diode physical model.
3. Some high density remote sources.
4. Electron-collision rate coefficients in argon gas.
5. Collisional energy  $\epsilon_c$  lost per electron-ion pair created in argon gas.
6. Simple model of cylindrical high density plasma source.
7. Electron temperature  $T_e$  for a given neutral argon density  $N$  and effective plasma size  $d_{eff}$  in a low pressure high density source.
8. The wall sheath region in a high density source.
9. A typical high profile ECR system; (a) geometric configuration; (b) axial magnetic field variation, showing one or more resonance zones.
10. Typical ECR microwave system.
11. Microwave field patterns for ECR excitation.
12. Common ECR configurations; (a) high profile; (b) low profile; (c) low profile with multidipoles; (d) close-coupled; (e) distributed (DECR); (e) microwave cavity excited
13. Basic principle of ECR heating; (a) continuous energy gain for right hand polarization; (b) oscillating energy gain for left hand polarization; (c) energy gain in one pass through a resonance zone
14.  $K_r$  versus  $\omega_{ce}/\omega$  for (a) low density  $\omega_{pe} < \omega$  and (b) high density  $\omega_{pe} > \omega$
15. Parameters for good ECR source operation: Pressure vs. power.
16. Schematic illustration of circuit used to measure wave electric field amplitude, kindly provided by Stevens et al. (91).
17. Electric field amplitude of RHP wave for two different magnetic field configurations. Note that the wave is damped at the Doppler shifted resonant field of  $\sim 975$  Gauss. Adapted from Ref. (91) with permission.
18. Transverse electric fields of helicon modes at five different axial positions; (a)  $m = 0$ ; (b)  $m = 1$  (after Chen, 1991).
19.  $k_{\perp}R$  versus  $k_z/k$  for helicon modes.
20. Magnetic field amplitude for helicon waves at three different values of  $B_0/n$ . Reprinted from Ref. (84) with permission.
21. Illustrating the antenna for  $m = 1$  helicon mode excitation (after Boswell et al, 1982).
22. Illustrating the quasistatic antenna coupling field  $\vec{E}_r$ ; (a) ideal and actual field; (b) spatial power spectrum of the field.
23. Measured density as a function of input power for  $B_0 = 80$  G at 5 mTorr in argon.
24. Measured density as a function of magnetic field at a fixed input power. The dashed line represents the resonance condition imposed by the antenna.
25. Schematic of inductively driven sources in (a) cylindrical and (b) planar geometries.
26. Equivalent transformer coupled circuit model of an inductive discharge.
27. Power versus density from the inductive source characteristics (curves) and from the plasma power balance (straight line). The curves are drawn for different values of the driving current  $I_{rf}$ .

28. Schematic of a helical resonator plasma source.
29. Axial wavenumber  $k_z$  versus frequency  $f$  for the coax and helix modes, with density  $n_0$  as a parameter. (○) helix mode,  $n_0 = 10^9 \text{ cm}^{-3}$ ; (□) helix mode,  $n_0 = 10^{11} \text{ cm}^{-3}$ ; (+) coax mode,  $n_0 = 0$ ; (Δ) coax mode,  $n_0 = 10^9 \text{ cm}^{-3}$ ; (×) coax mode,  $n_0 = 10^{11} \text{ cm}^{-3}$ .
30. Surface wave dispersion  $k_z$  versus  $\omega$  for the  $m = 0$  mode.
31. Illustrating the determination of the equilibrium density in a surface wave discharge. The high density intersection of the  $P'_{\text{abs}}$  and  $P'_{\text{lost}}$  gives the equilibrium density (after Moisan and Zakrzewski, 1991).
32. Density  $n_0$  and wave power  $P_w$  versus  $z$  for a typical surface wave source.
33. Etch rate of  $\text{SiO}_2$  as a function of peak-to-peak bias voltage in helicon discharge through chlorine. A threshold is clearly observed near 40 V (184). Figure kindly provided by and reprinted with permission from Plasma Materials and Technology.
34. Normalized, energy-flux-weighted, (a) cumulative and (b) differential angular distribution functions vs. incident, polar angle.
35. Schematic illustration of gridded energy analyzer used for measurements of ion energy distribution functions. Reprinted from (199) with permission.
36. Schematic illustration of apparatus used to measure spatially-resolved ion velocity distribution functions by laser-induced fluorescence (101).
37. Change in the bombarding ion energy distribution as the wafer-level coil current  $i_m$  is varied. Reprinted from (196,197) with permission.
38. Ion velocity distribution functions at several pressures downstream from (a)  $\text{N}_2$  and (b)  $\text{N}_2/\text{He}$  ECR plasmas. Reprinted from (201) with permission.
39. (a) Average ion velocity along  $\mathbf{B}$ ,  $v_z$ , measured by Doppler shifted laser-induced fluorescence, (b) corresponding average energy, " $k_B T_z$ ", and (c) perpendicular ion temperature  $T_{i\perp}$ , all as a function of pressure downstream from a  $\text{N}_2$  and  $\text{N}_2/\text{He}$  ECR sources. Reprinted from (201) with permission.
40. Parallel ion velocity distribution functions at different positions from a wafer platen situated downstream from an Ar/He ECR source (101).
41. Simulated plasma potential as a function of axial and radial position for an ECR source. Note the distributed sheath or potential step from the narrow source region, between axial positions 0 and 40 cm, and the downstream region beyond 40 cm. Reprinted from (195) with permission.
42. Simulated ionization rate as a function of radial and axial position for the same system as in Fig. 41. Note the local maximum in the ionization rate where the plasma expands which results from a neutral density gradient. Reprinted with permission from (195).
43. Perpendicular ion velocity distribution functions at different radial positions (101). When a collimating magnetic field is applied (dashed curves), the mean ion velocity is reduced but the spread in ion energies increases. (a) 0.38 mTorr; (b) 0.82 mTorr.
44. Ion energy distributions through an rf sheath biased at 0.5 and 20 MHz. Reprinted with permission from (185).
45. Variation of maximum ion energy through dc biased sheath as a function of electrode area. Smaller electrodes exhibit larger variation of ion energy with bias voltage. Reprinted with permission from (199).
46. Equivalent circuit model used to explain distribution of voltages between biased and grounded sheaths for both low and high frequency.
47. Displaced atom density,  $\Delta D_{\text{da}}$ , for a GaAs surface as a function of ion current density in  $\text{SF}_6$  ECR and RIE plasmas. For the same ion flux, damage in the ECR is significantly reduced presumably

- because of a reduction in ion energy. Reprinted with permission from (220).
48. Metal oxide nitride silicon (MNOS) device used to measure charging voltage in high efficiency plasmas. The flat band voltage shift  $\Delta V_{FB}$  depends on the peak voltage, created by charging in the plasma, across the dielectric. Reprinted with permission from (232).
  49. Leakage current from CMOS inverter circuit as a function of difference in current density from the center to the edge of an ECR plasma Adapted from Figs. 5 and 6 in (230).
  50. Schematic illustration of how uniformity of plasma current density can induce charging damage.
  51. Dependence of ion current density uniformity on bias frequency in  $N_2$  ECR plasma. Reprinted with permission from (233).
  52. Cumulative failure rate caused by gate oxide breakdown as a function of bias frequency in an  $O_2$  plasma. Reprinted with permission from (233).

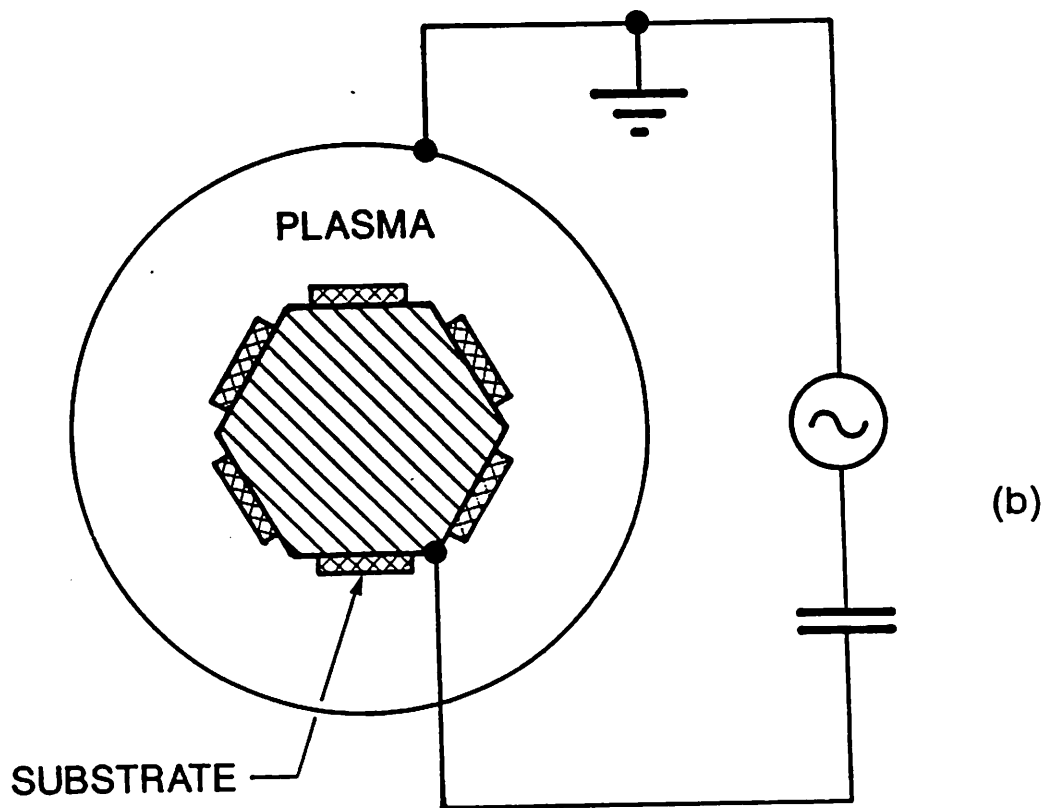
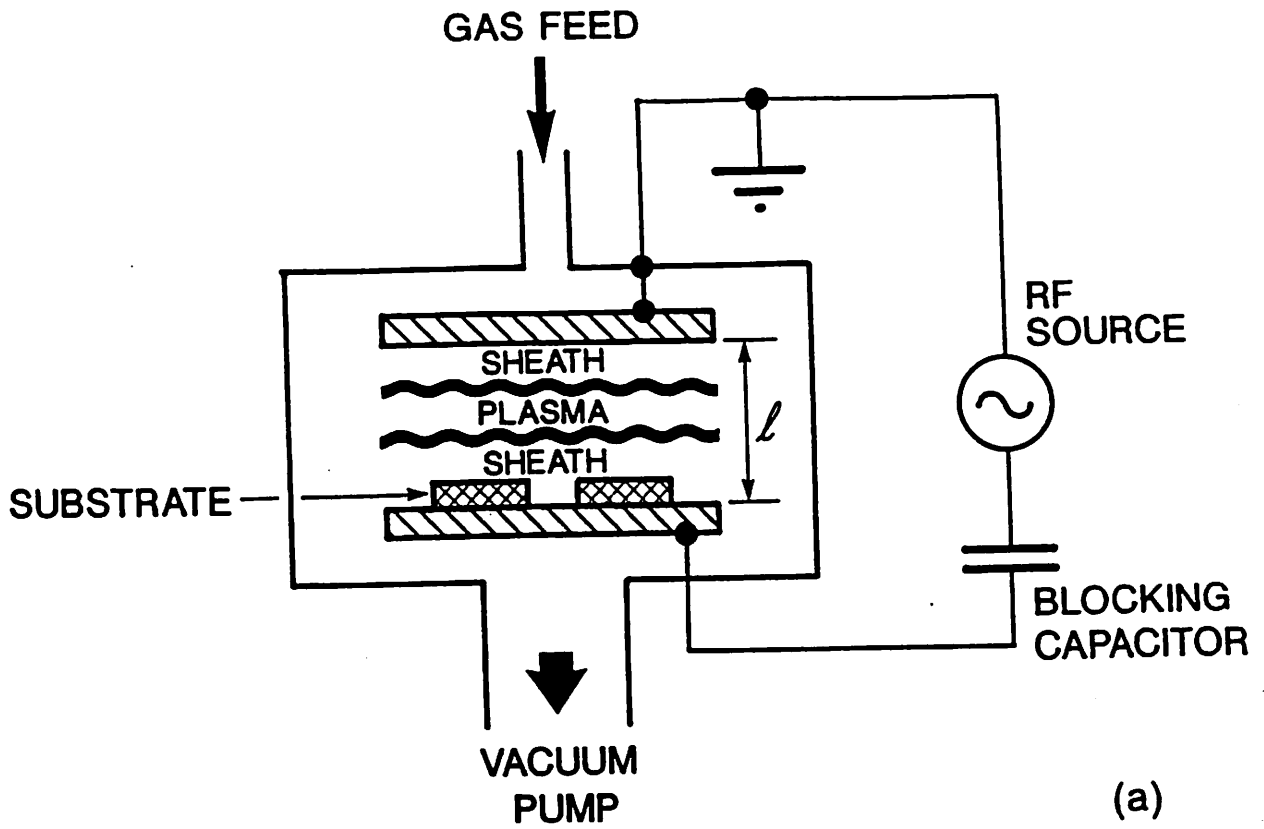


Fig. 1

# RF DIODE PHYSICAL MODEL

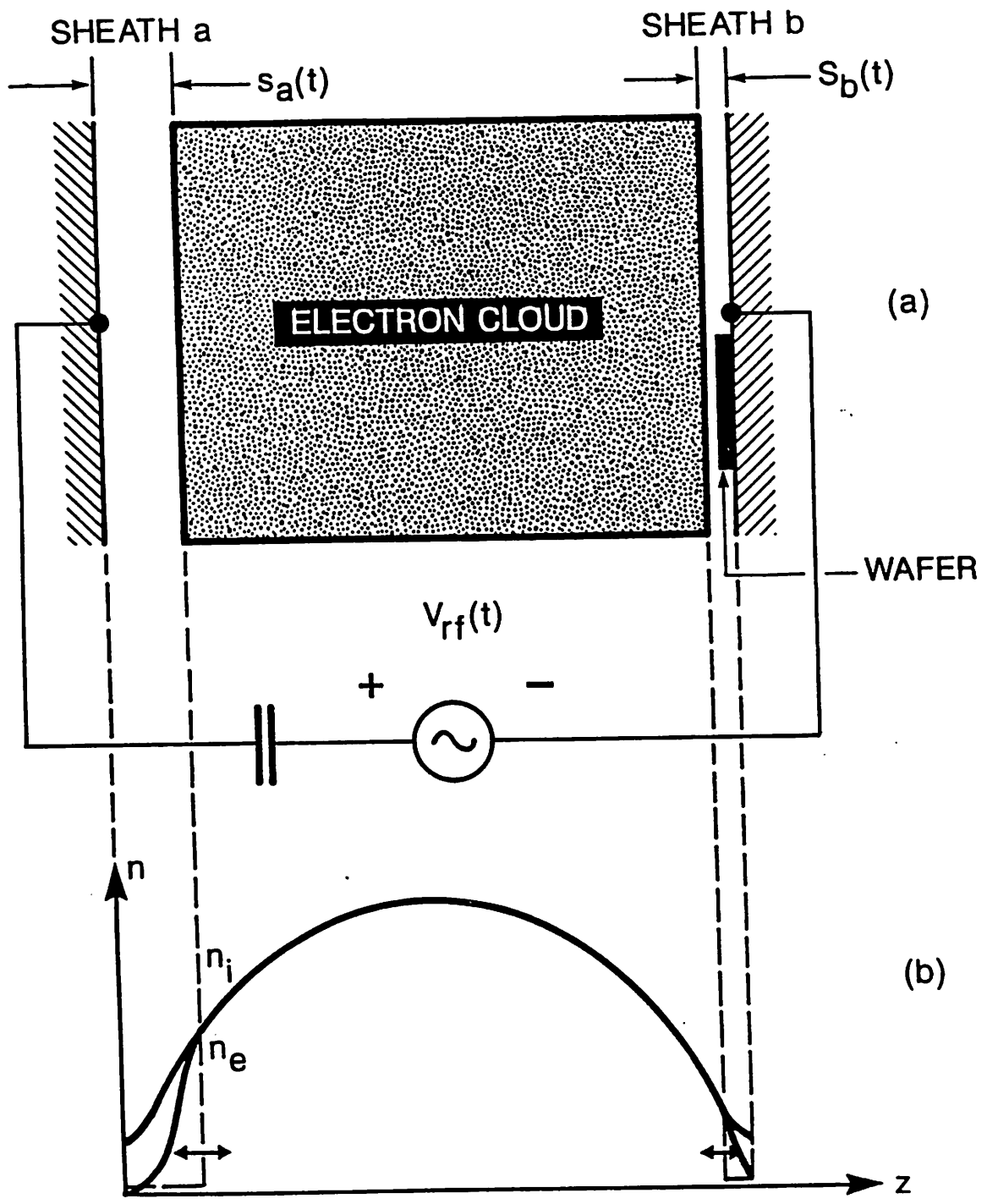


Fig. 2

# HIGH DENSITY REMOTE SOURCES

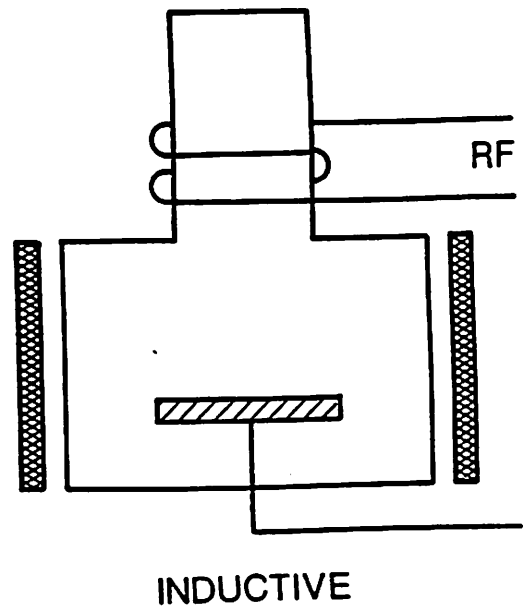
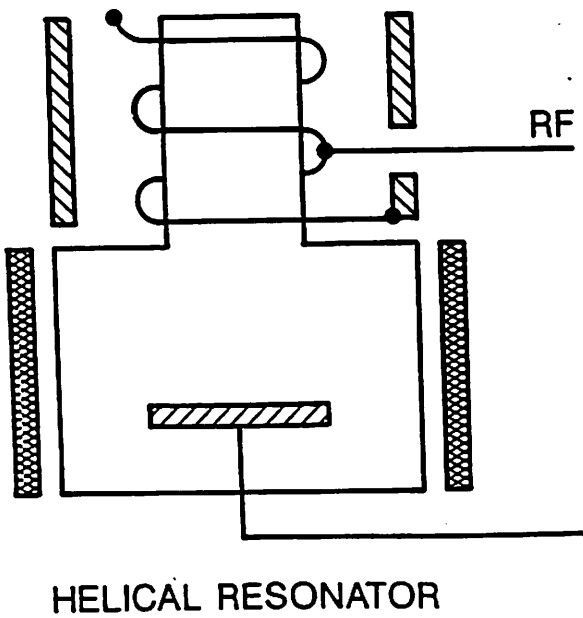
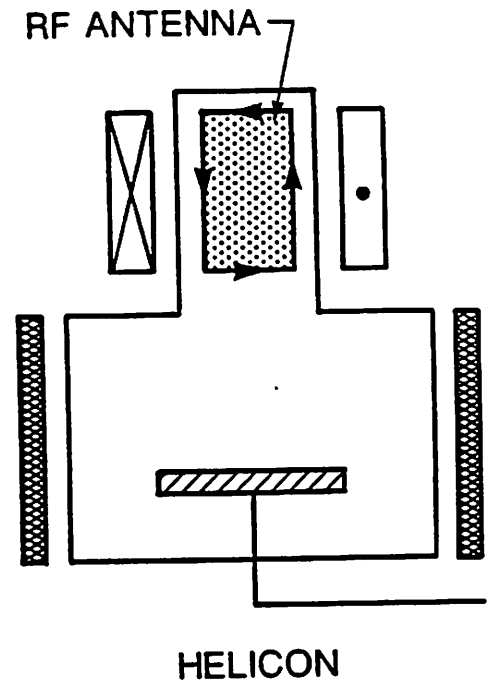
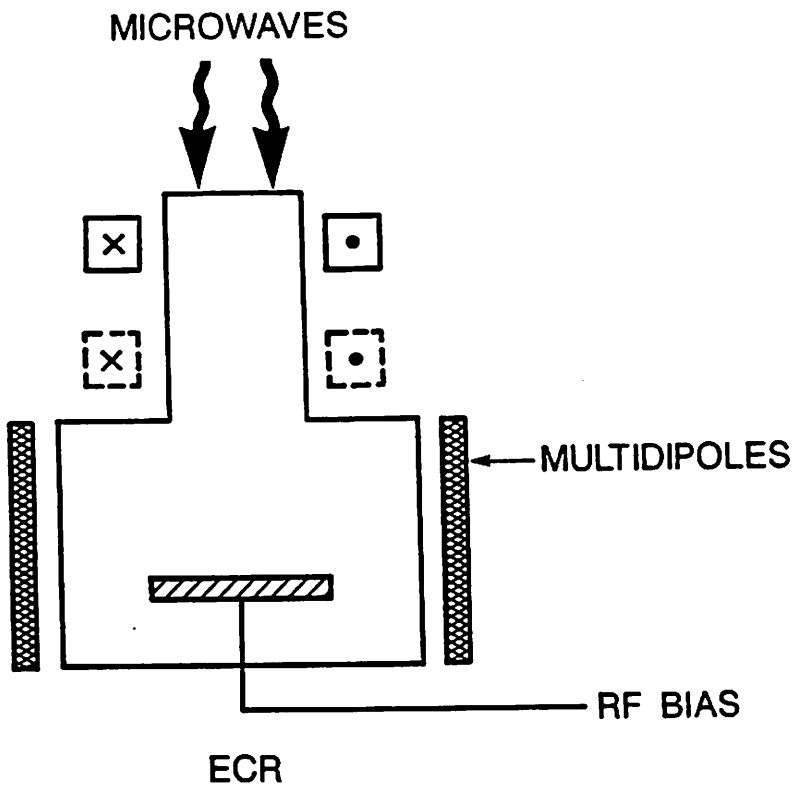


Fig. 3

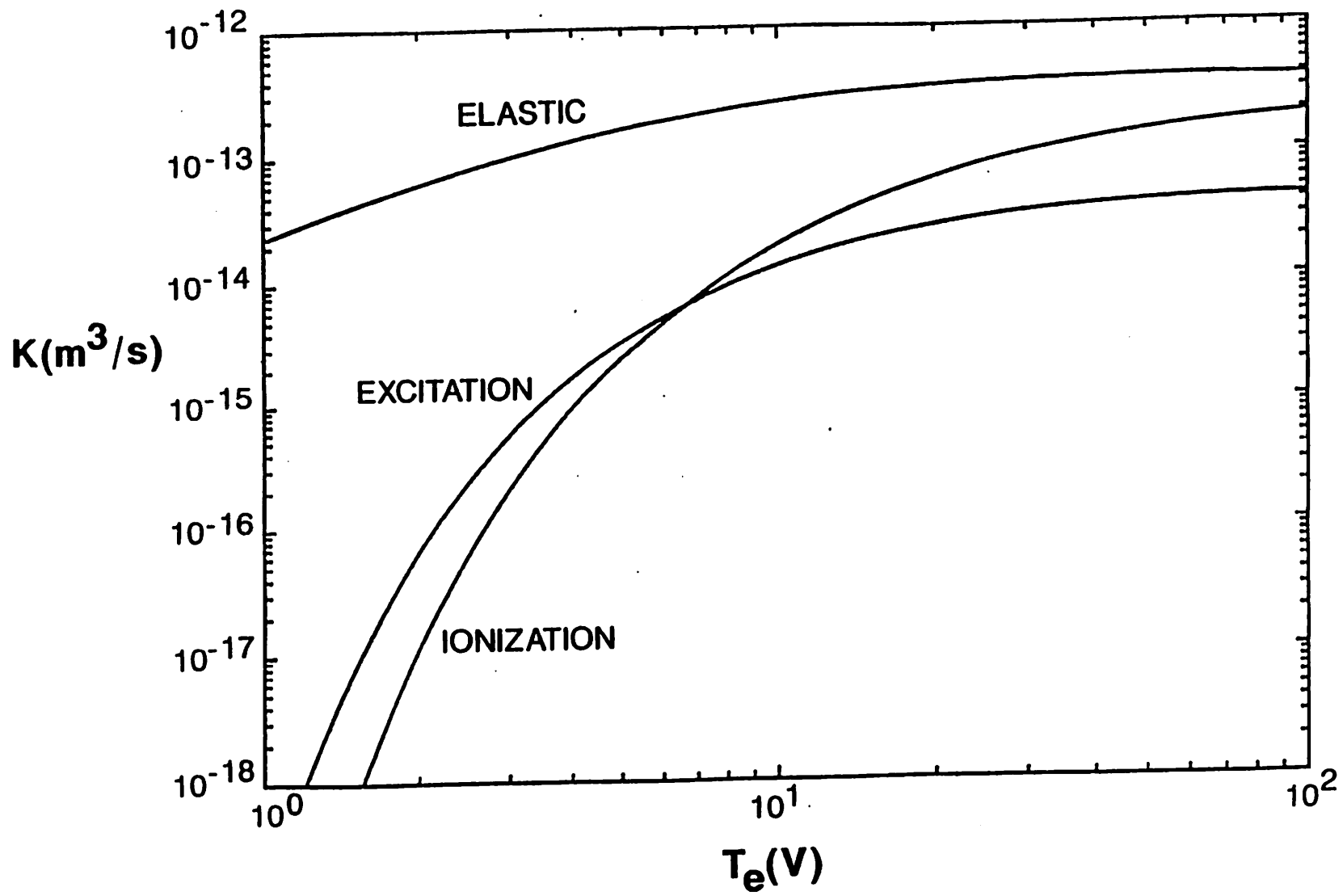


Fig. 4

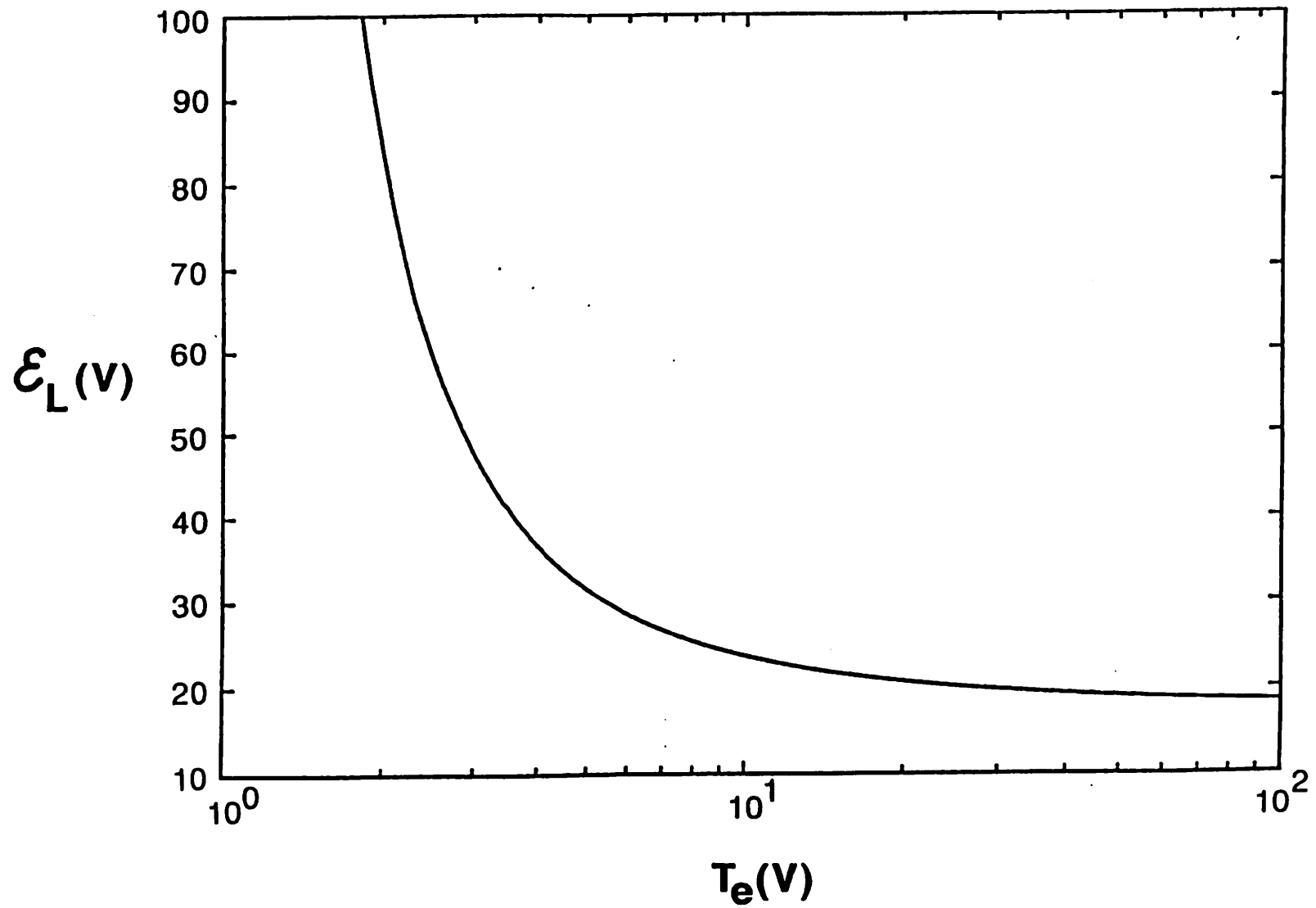


Fig. 5

## SIMPLE DISCHARGE MODEL

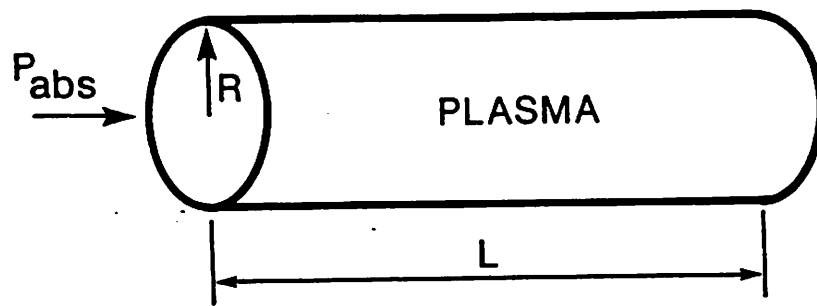


Fig. 6

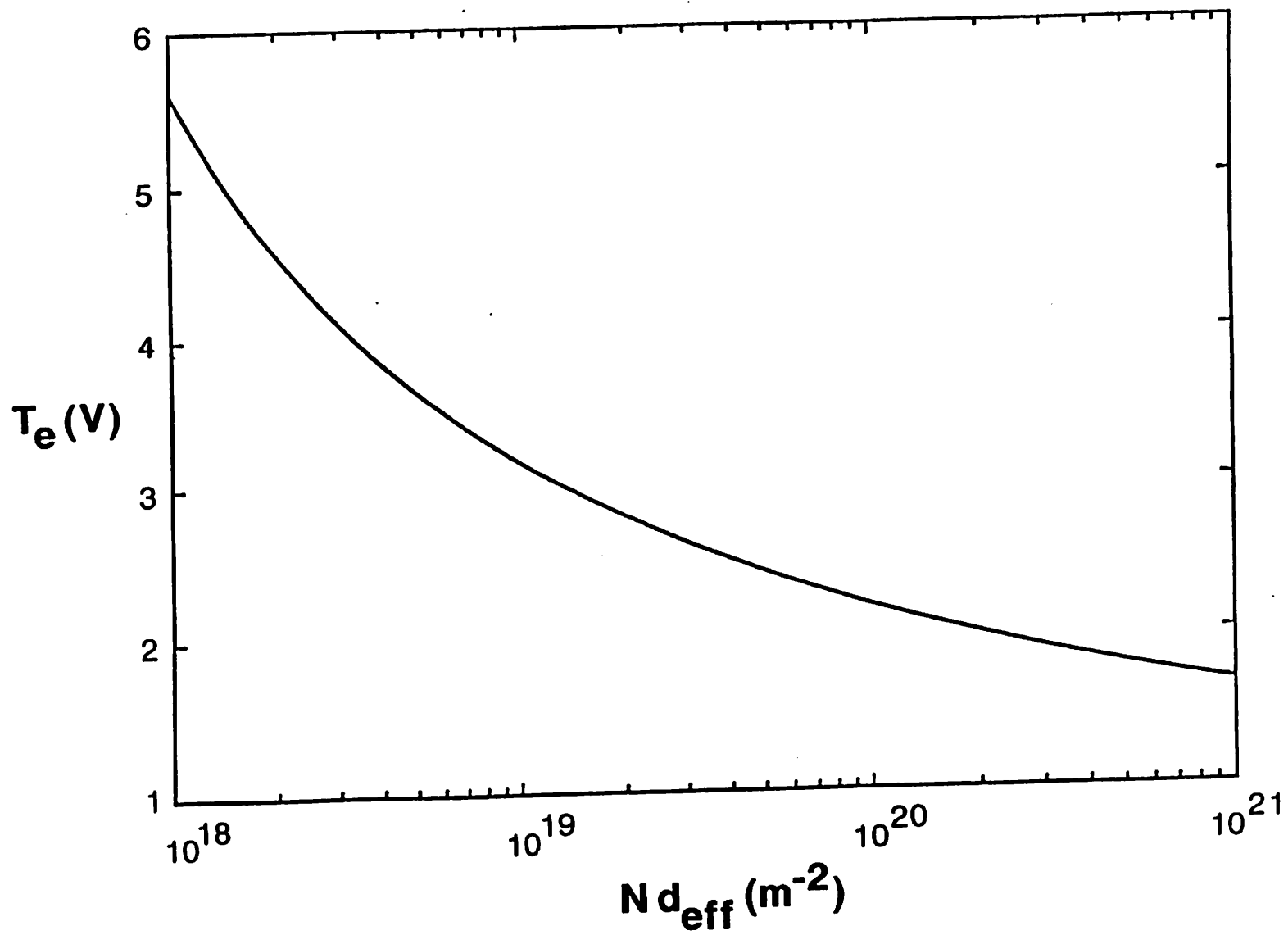


Fig. 7

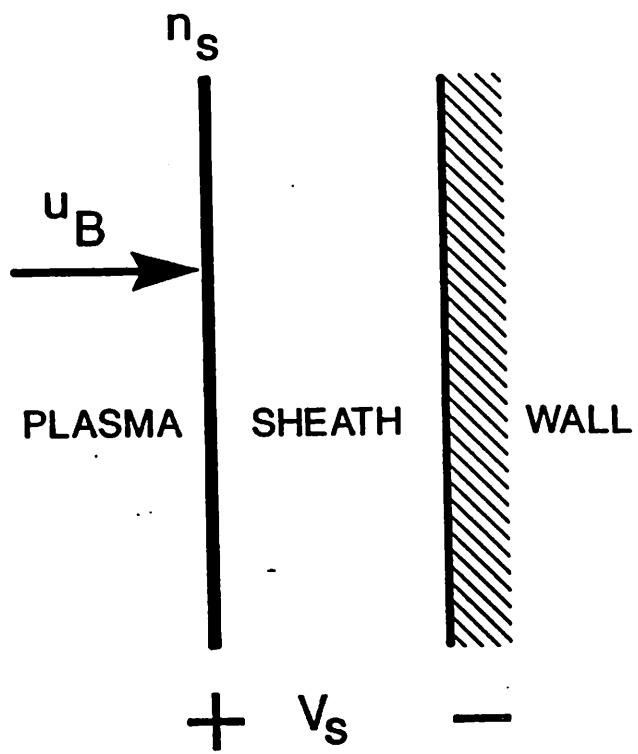


Fig. 8

# TYPICAL ECR SYSTEM

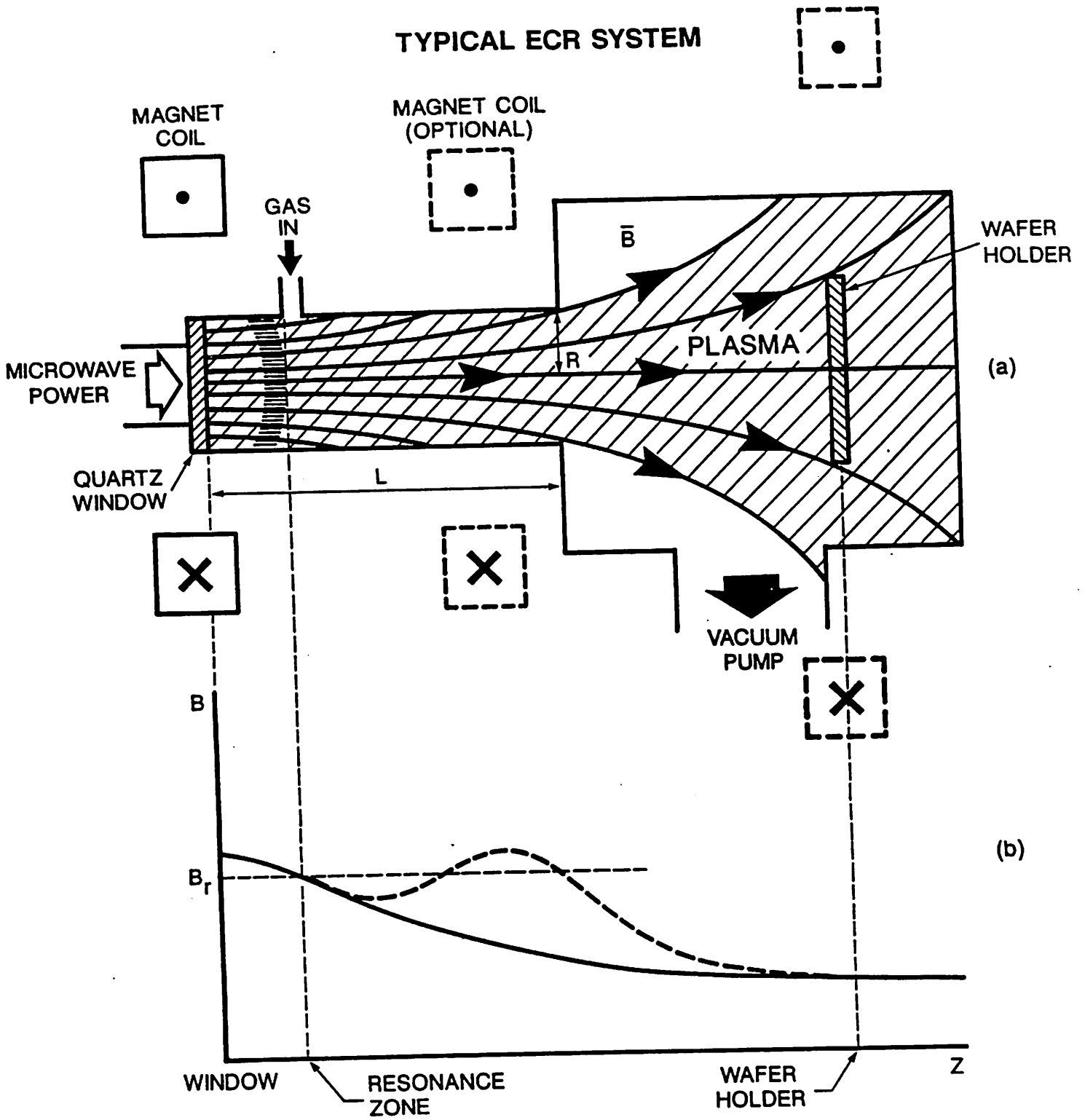


Fig. 9

# ECR MICROWAVE SYSTEM

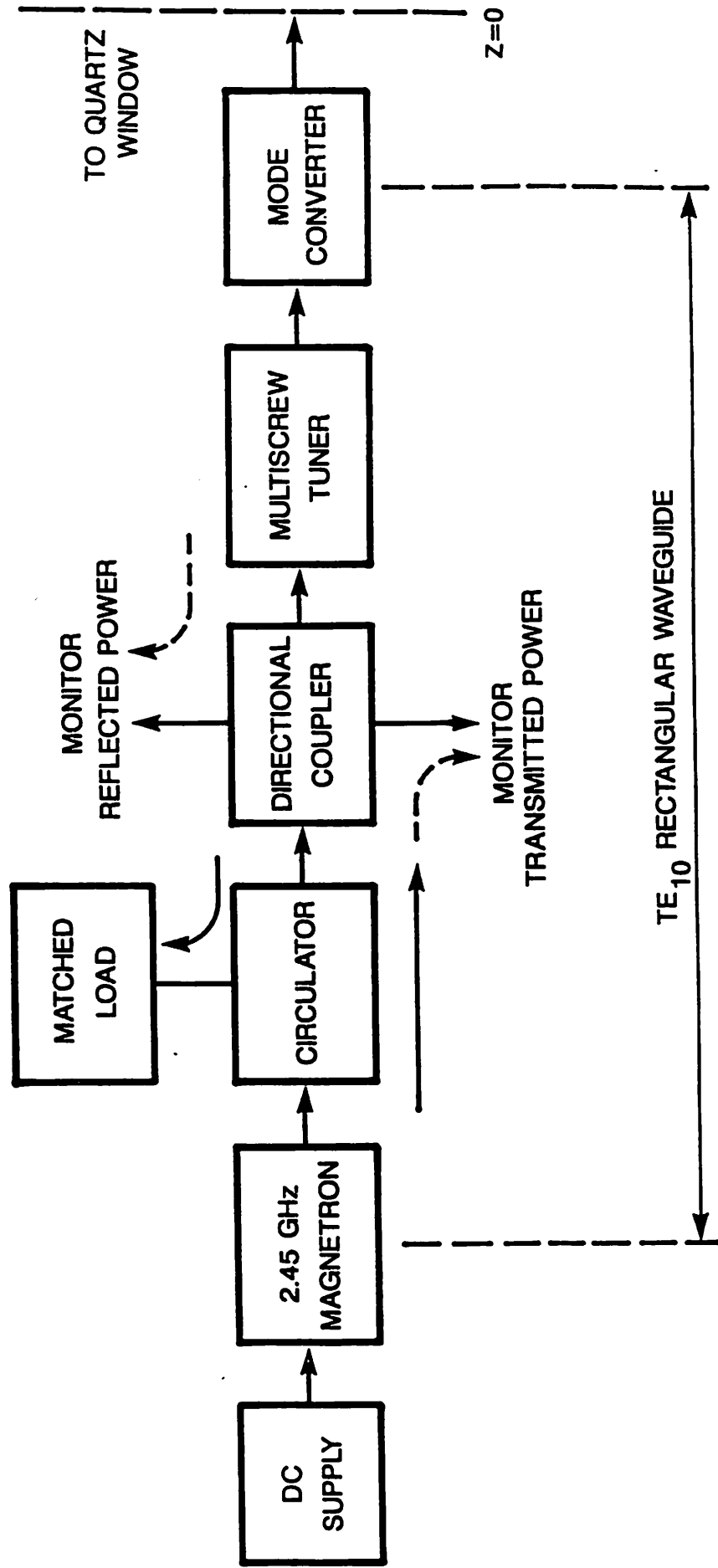


Fig. 10

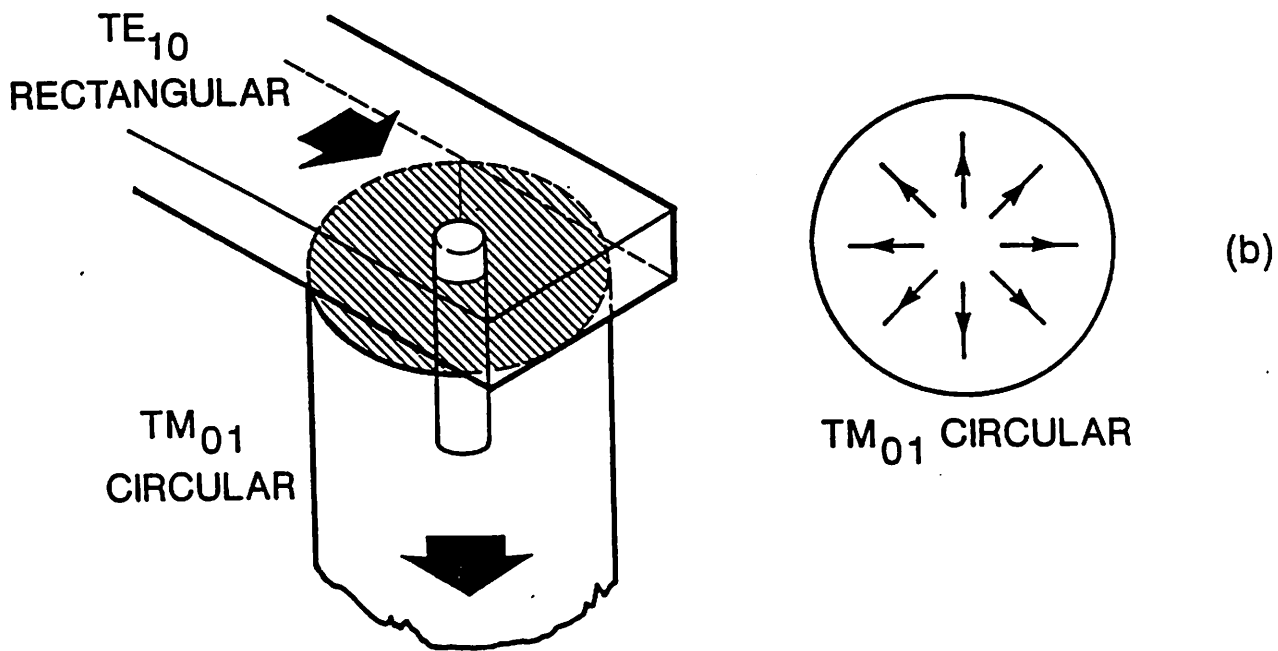
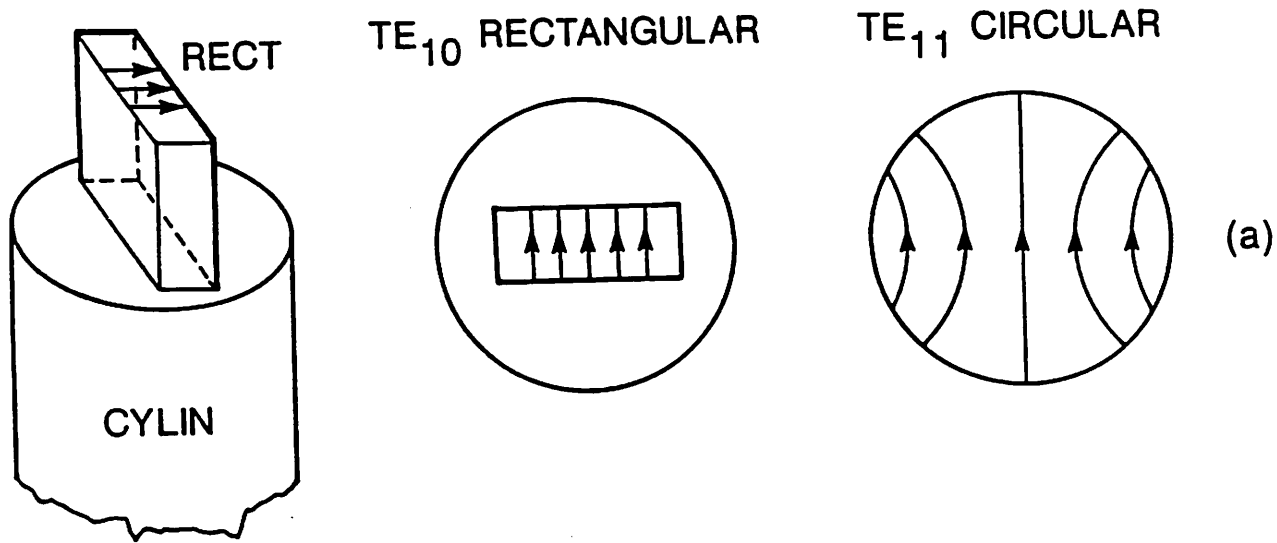
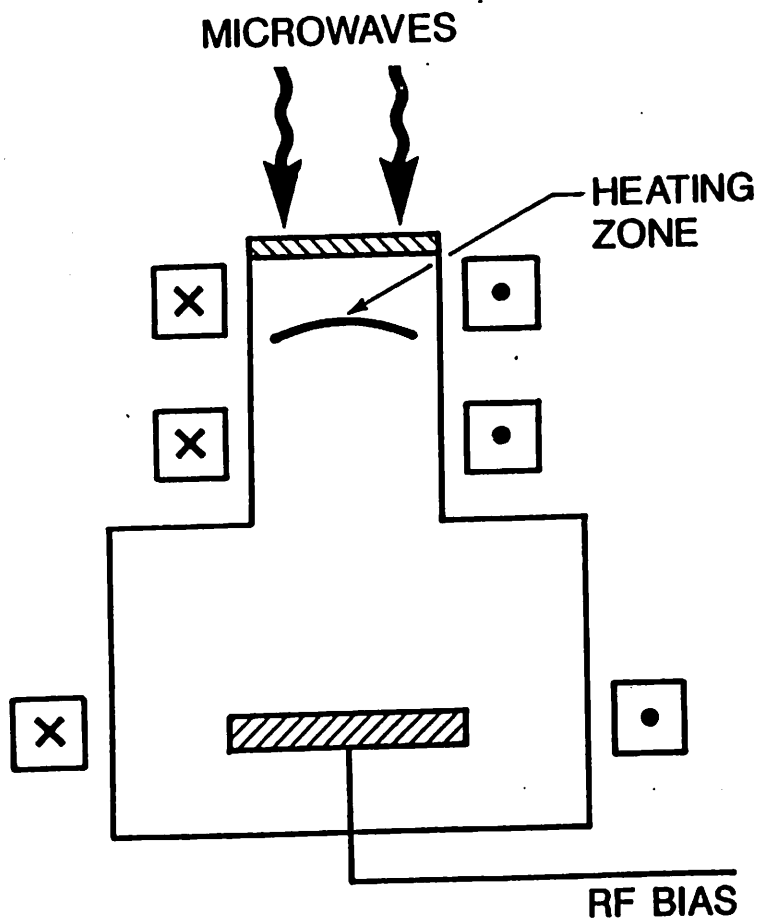
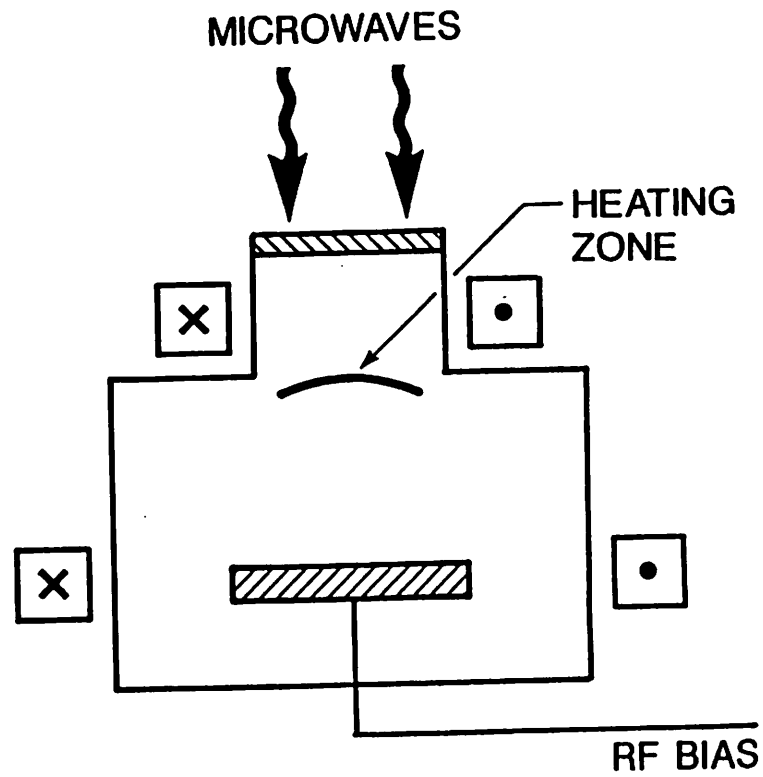


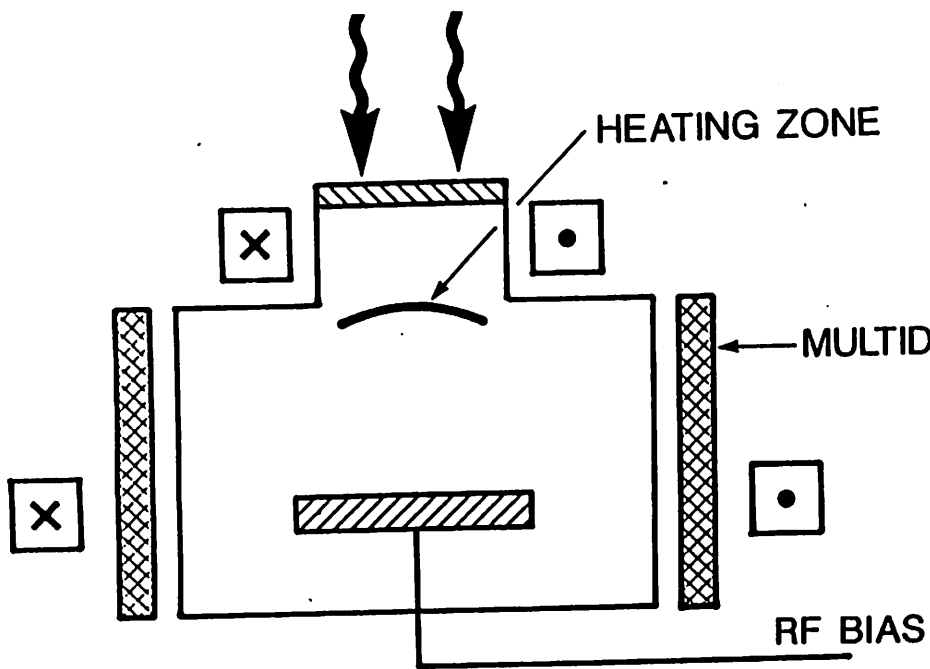
Fig. 11



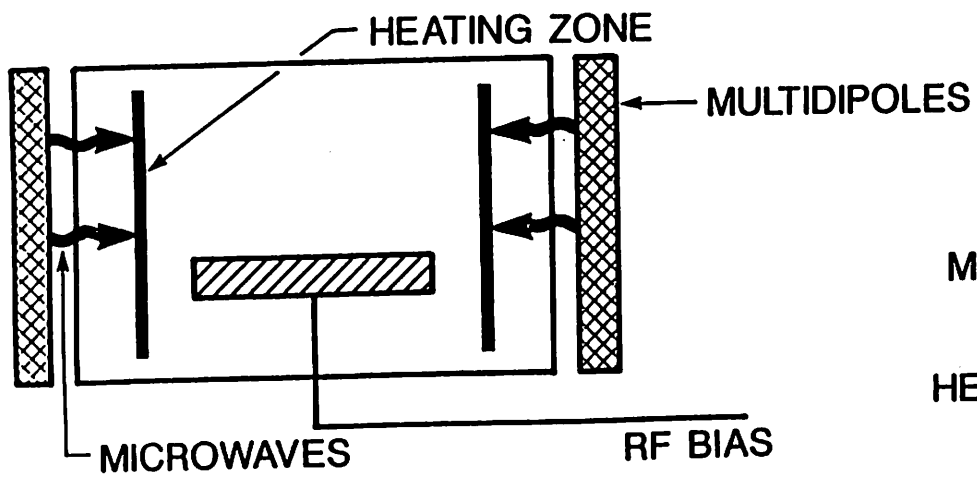
(a) HIGH PROFILE



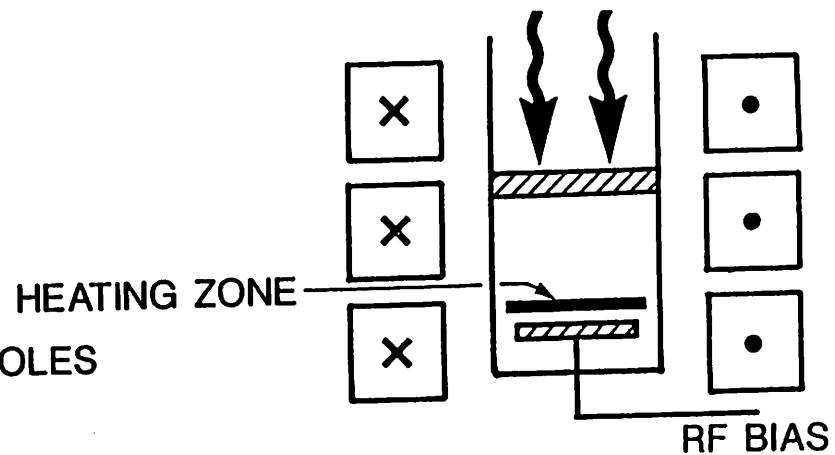
(b) LOW PROFILE



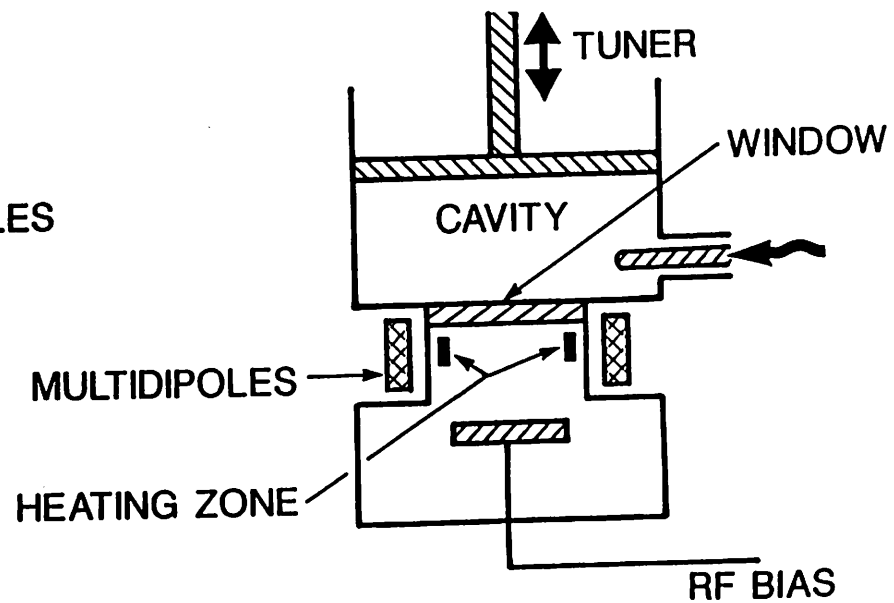
(c) LOW PROFILE WITH MULTIDIPOLES



(e) DISTRIBUTED (DECR)



(d) CLOSE-COUPLED TUNER



(f) MICROWAVE CAVITY

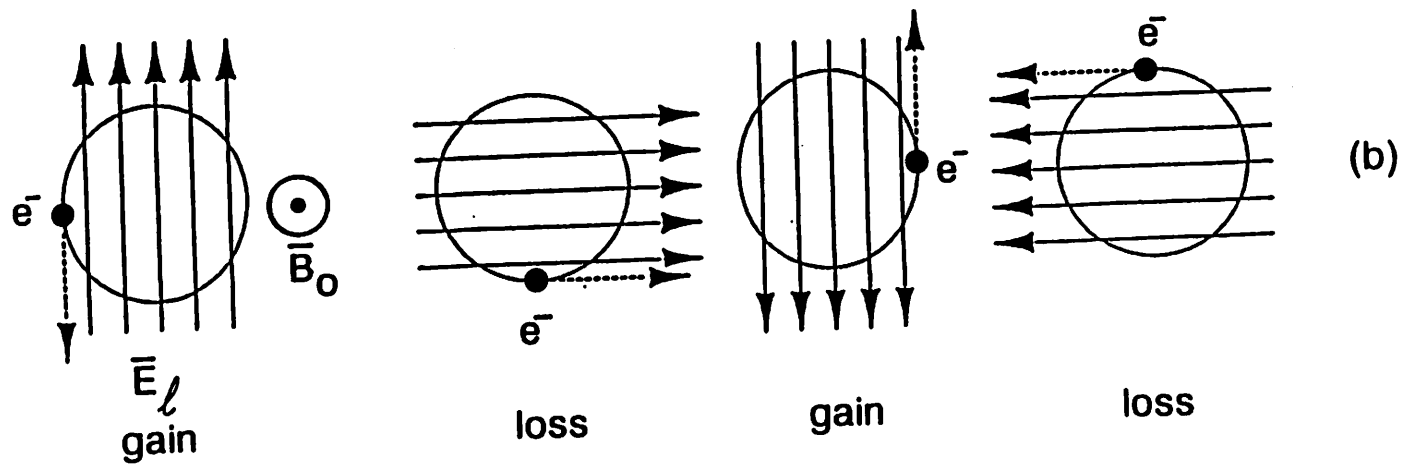
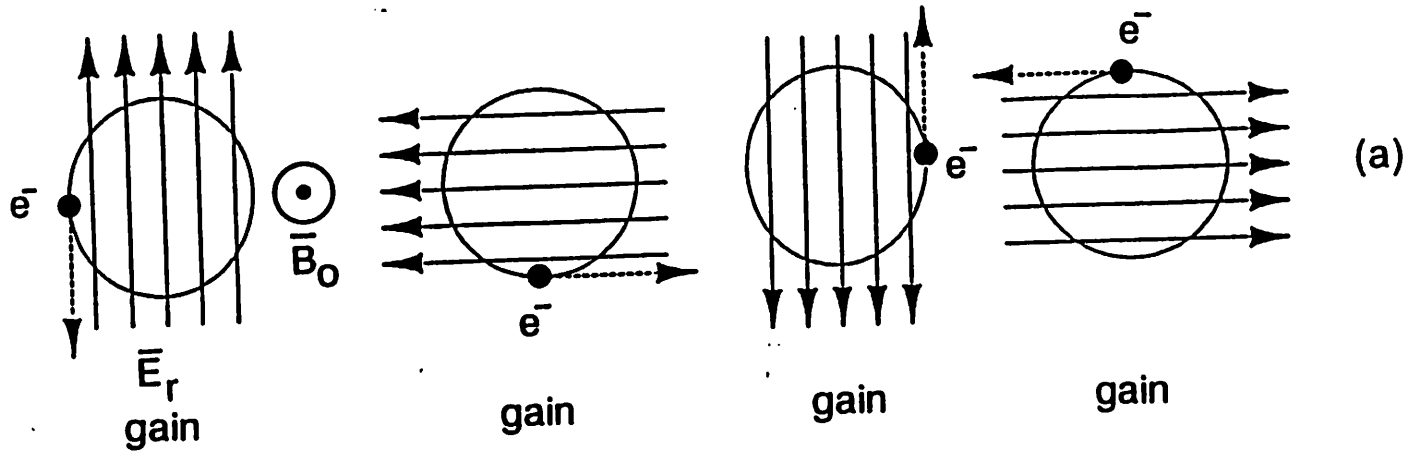


Fig. 13 (a), (b)

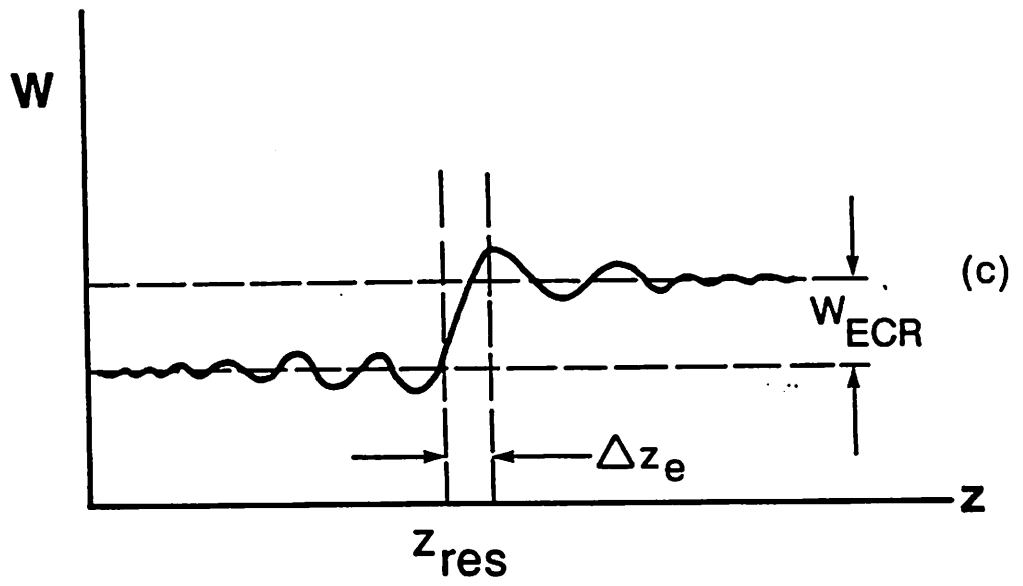


Fig. 13(c)

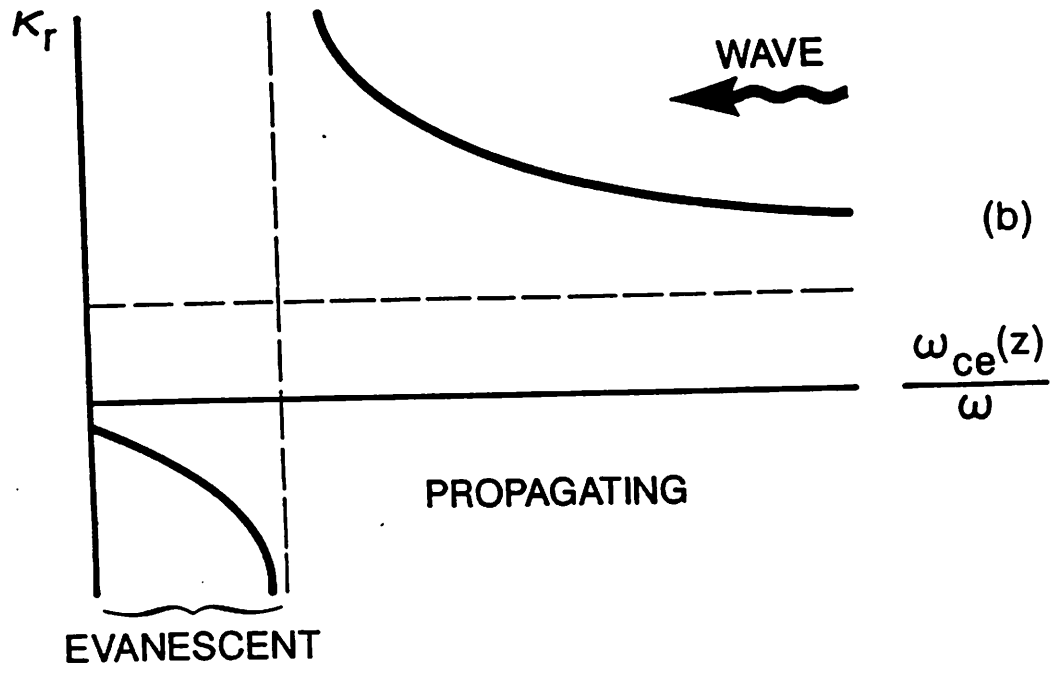
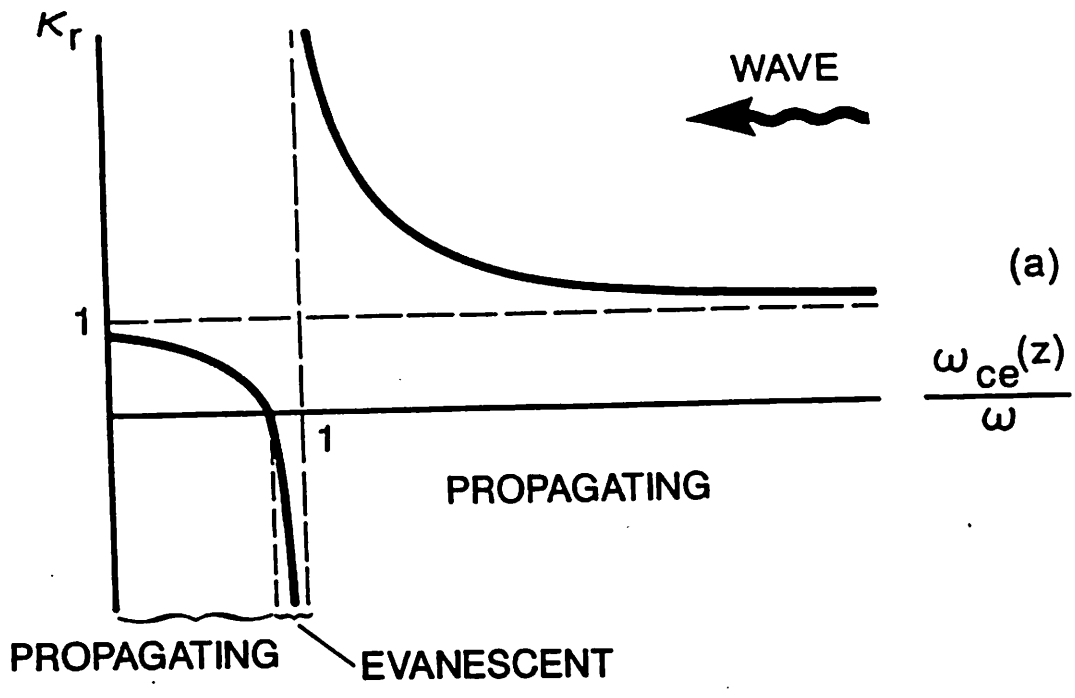
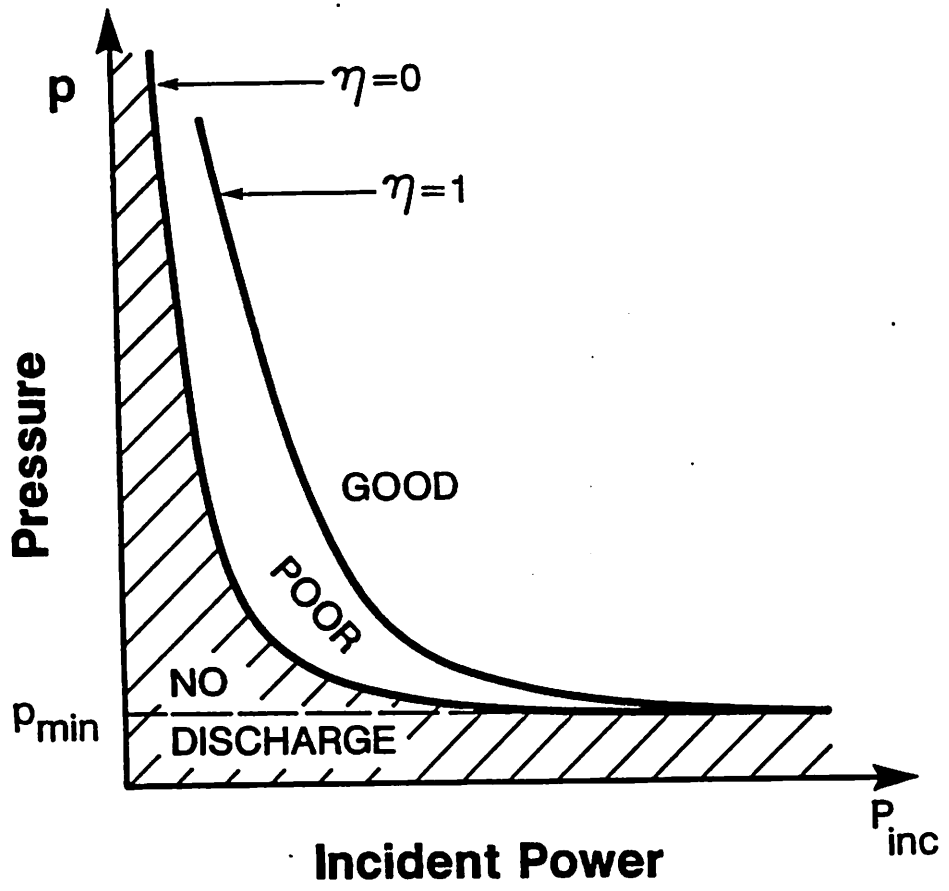
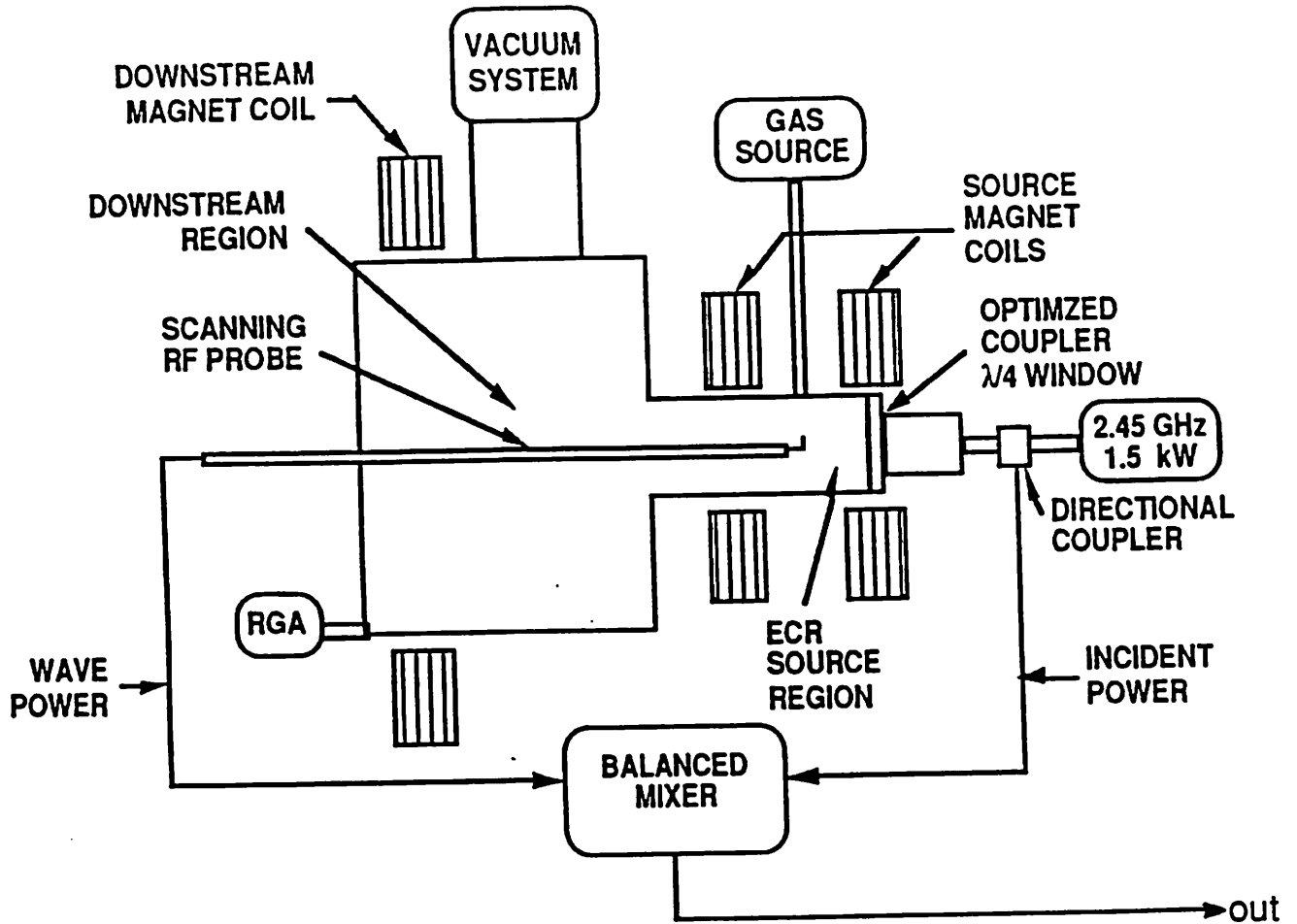
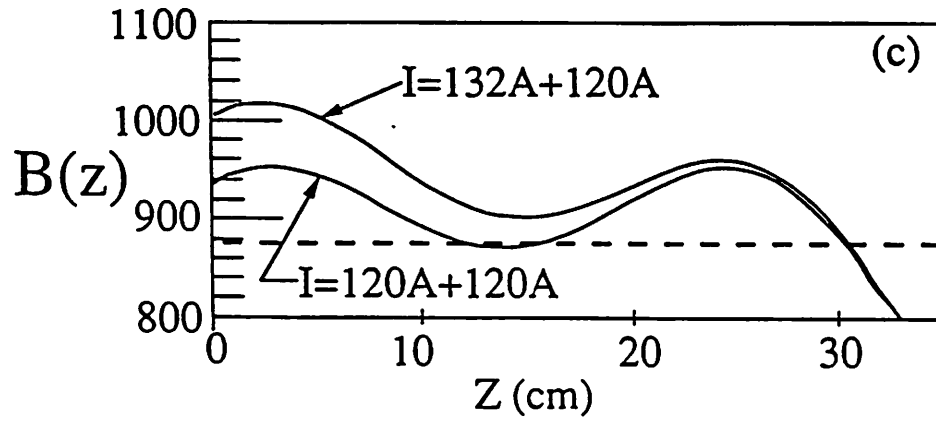
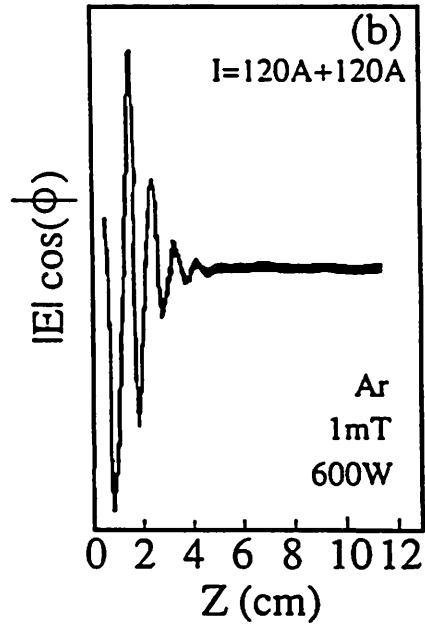
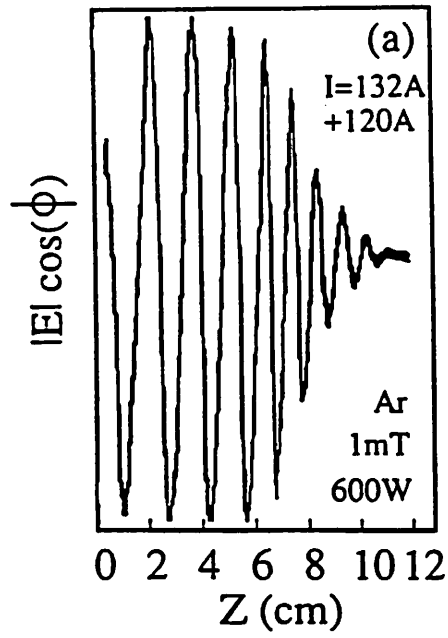


Fig. 14







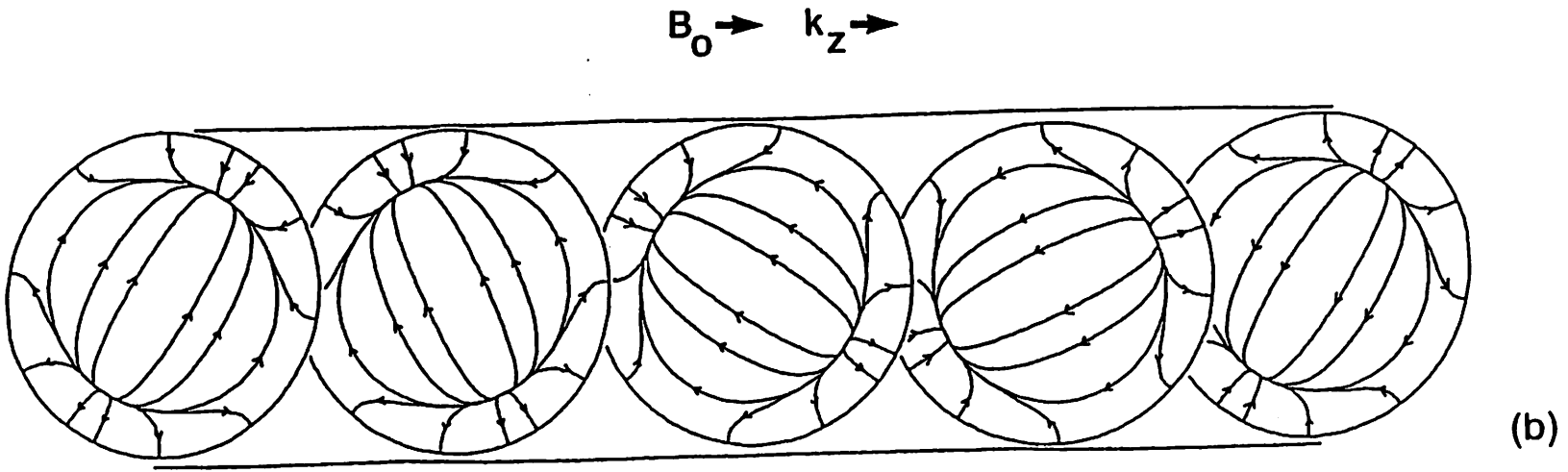
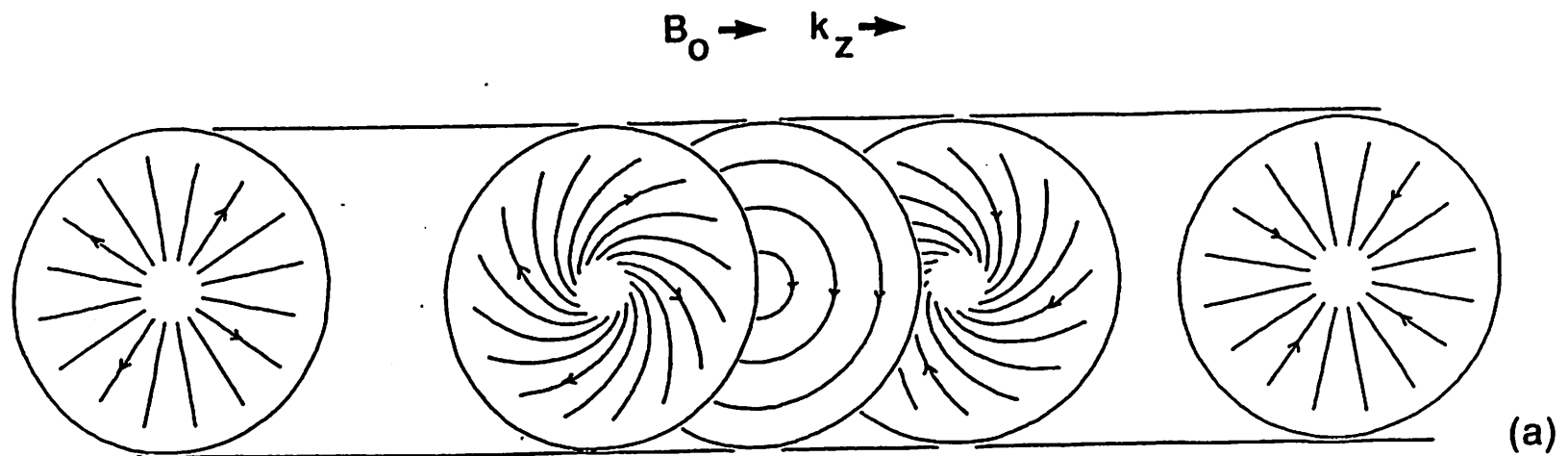


Fig. 18

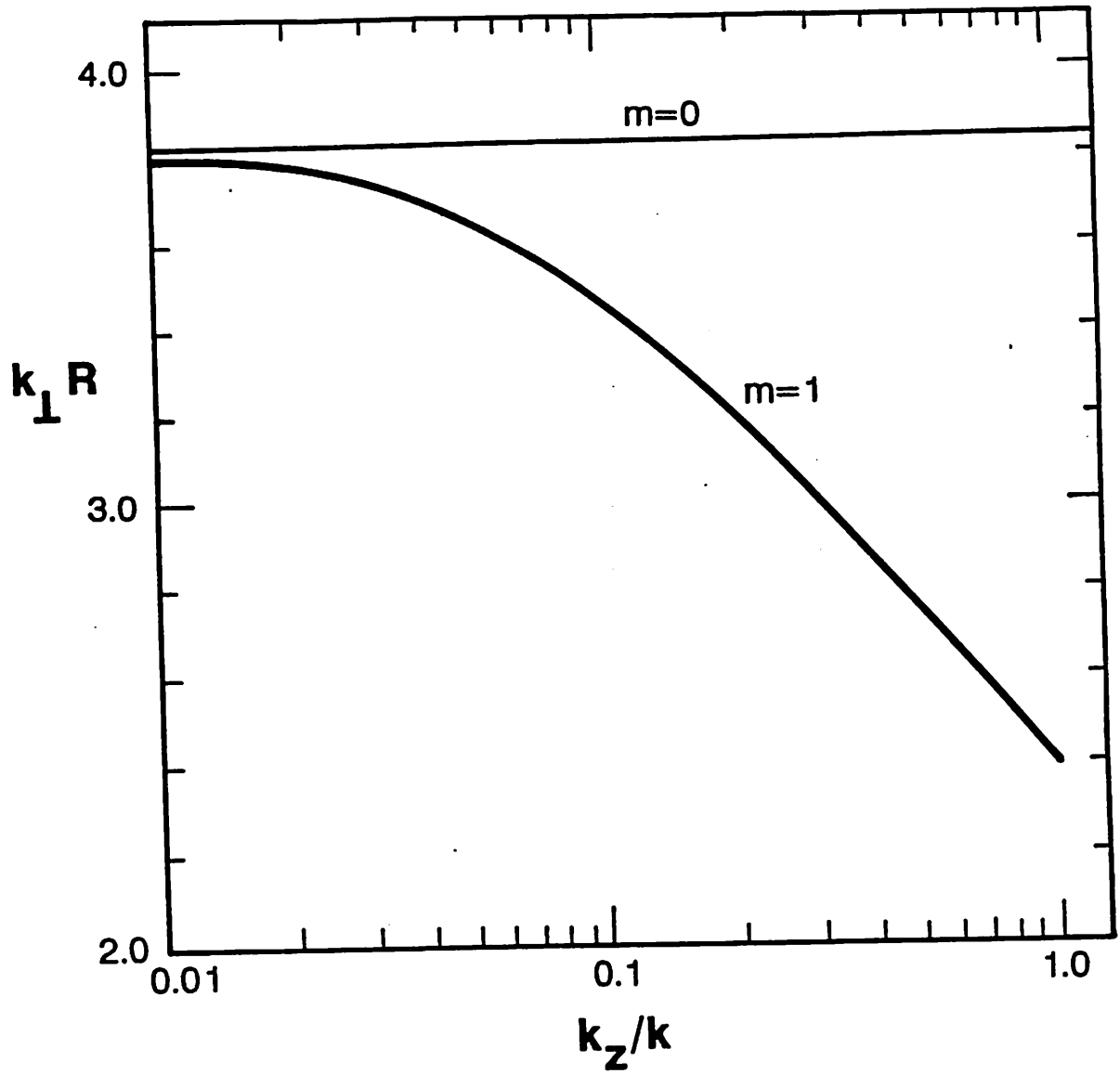
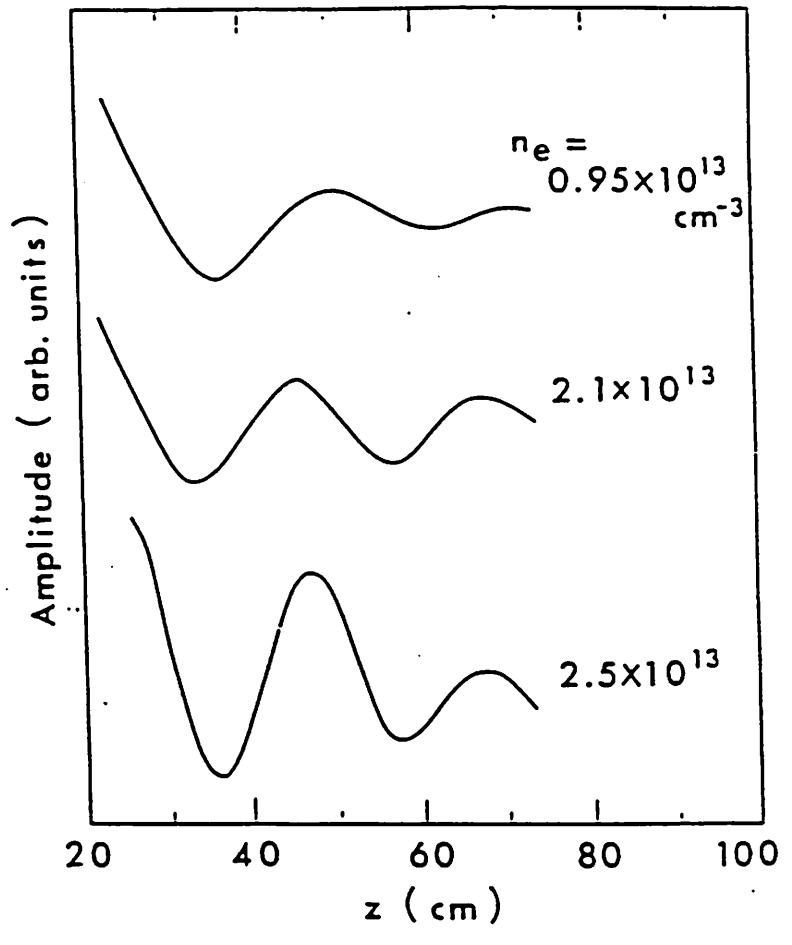


Fig. 19



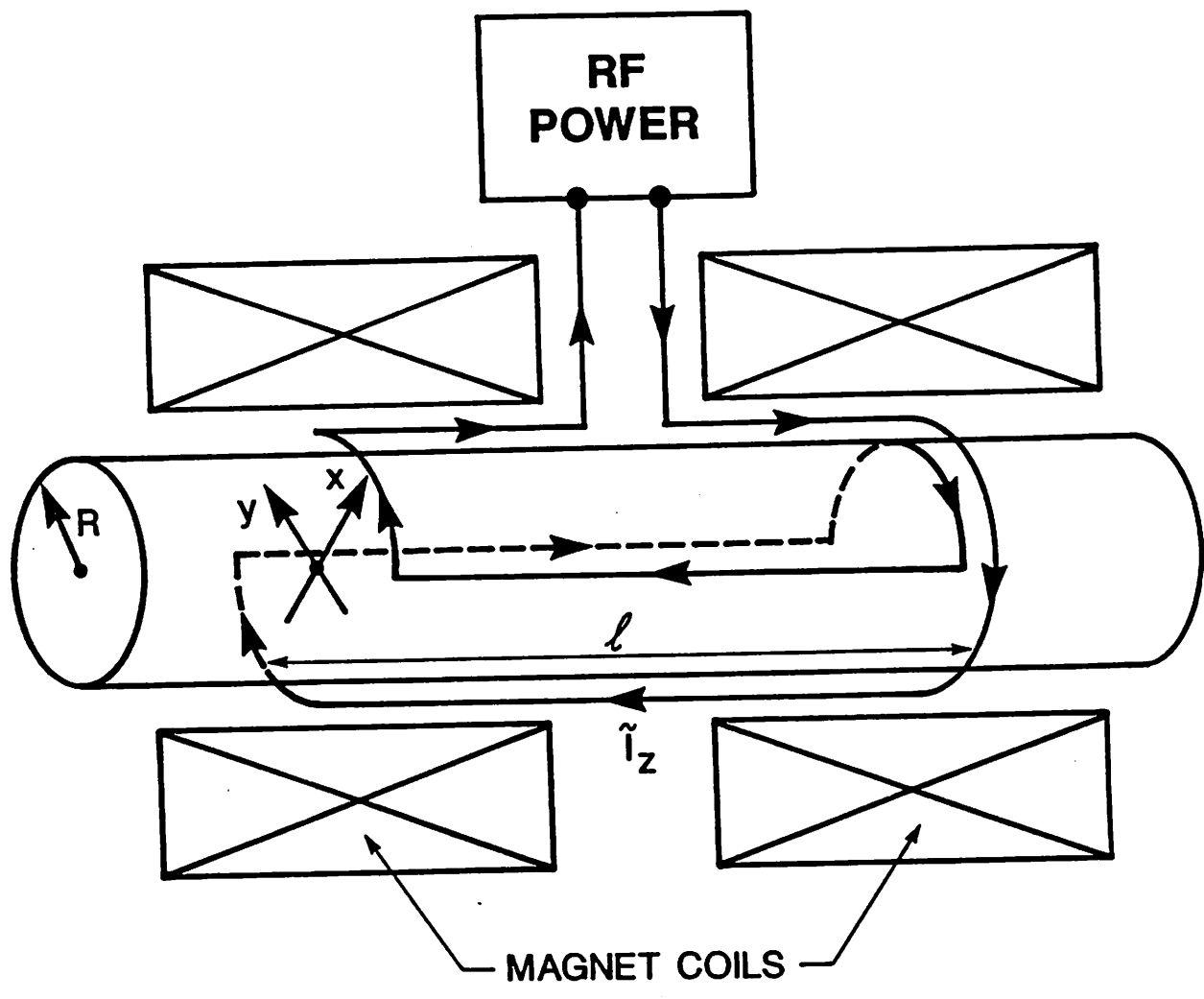


Fig. 21

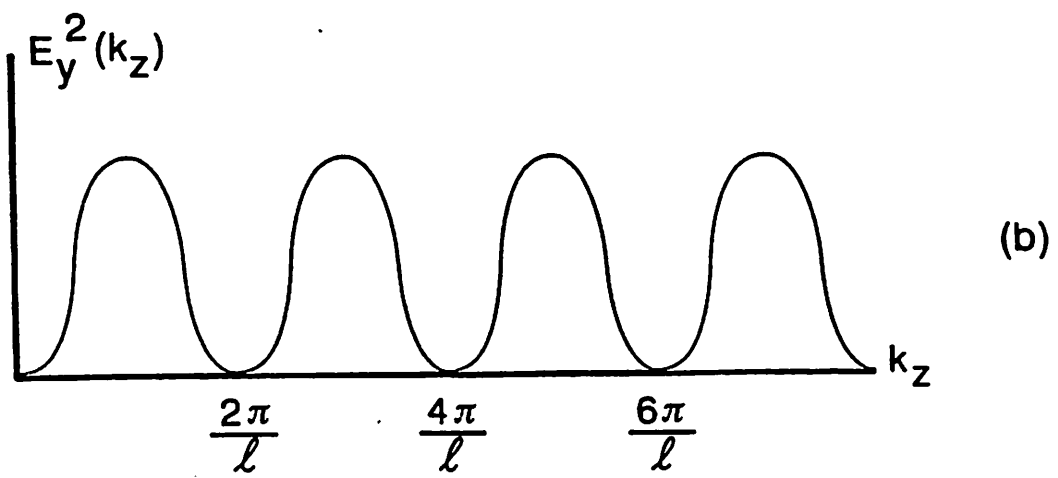
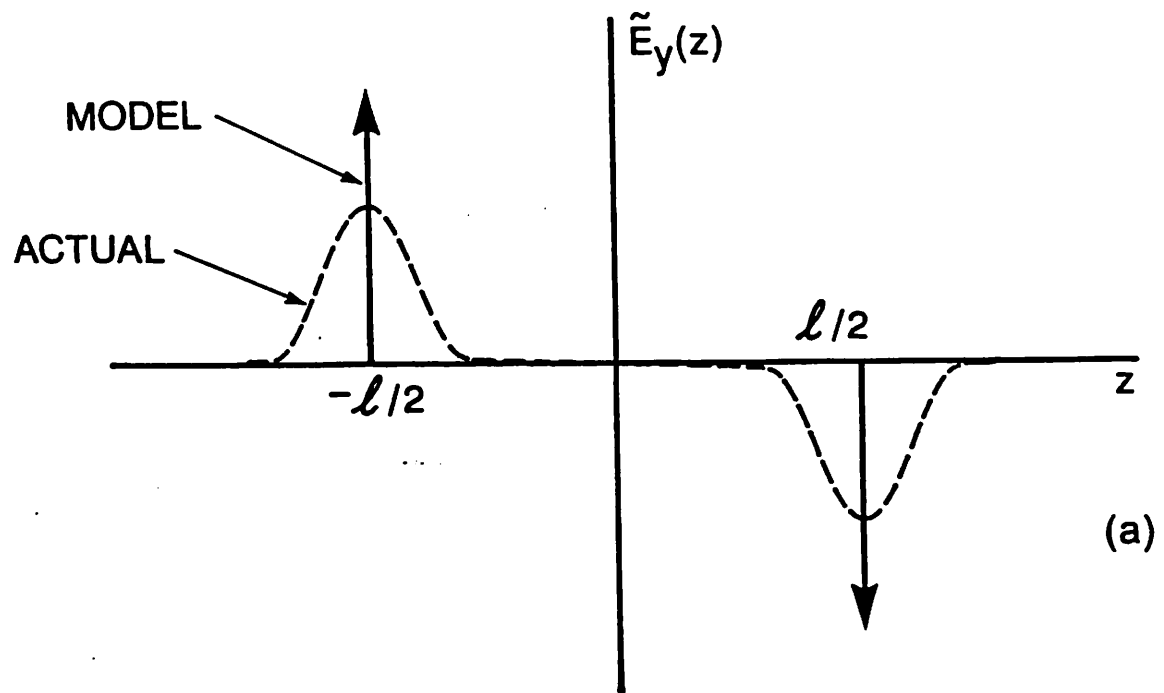


Fig. 22

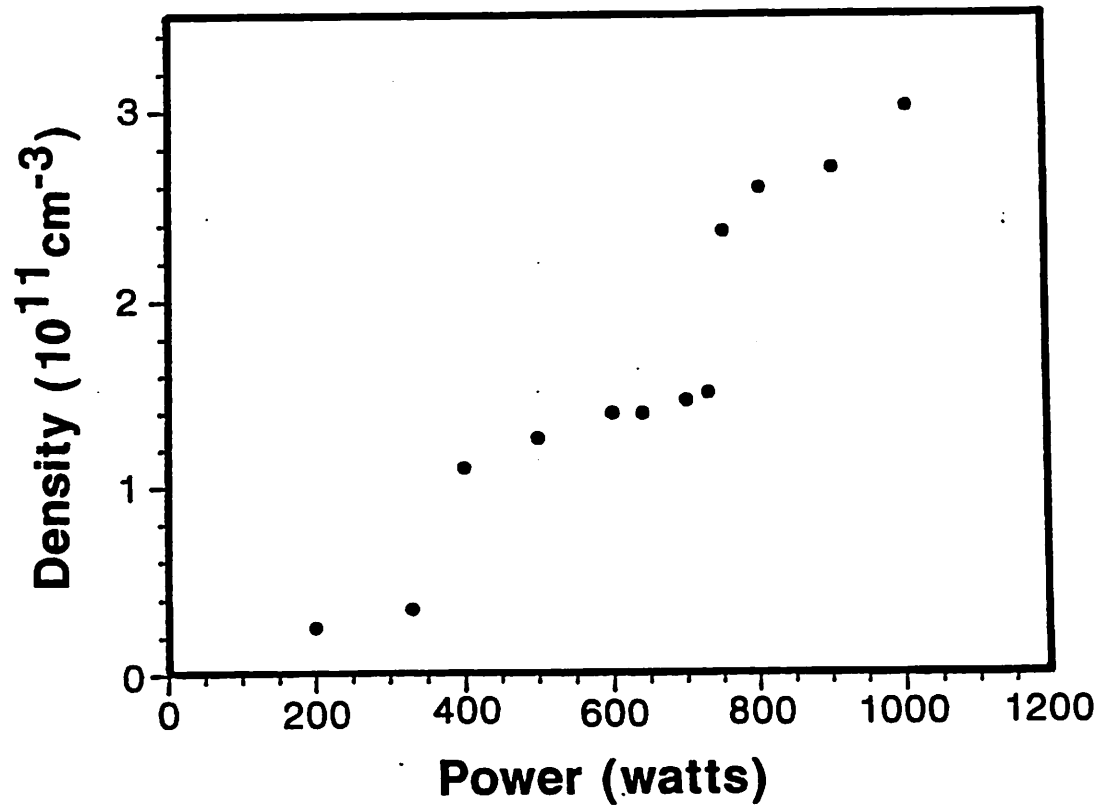


Fig. 23

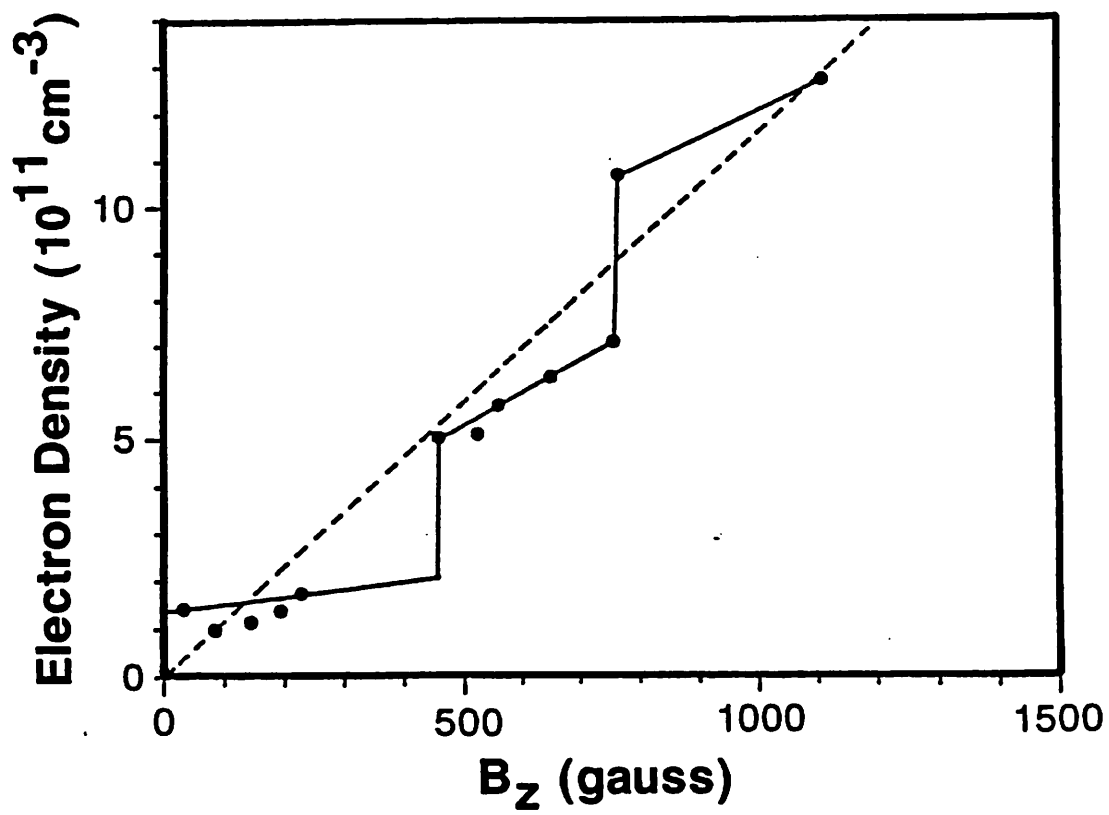
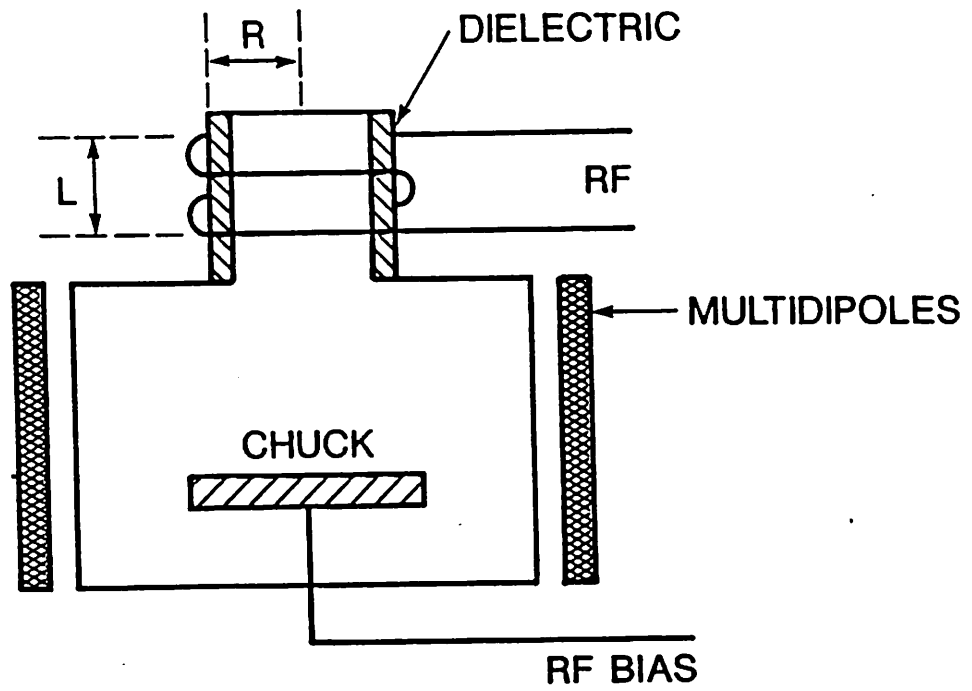
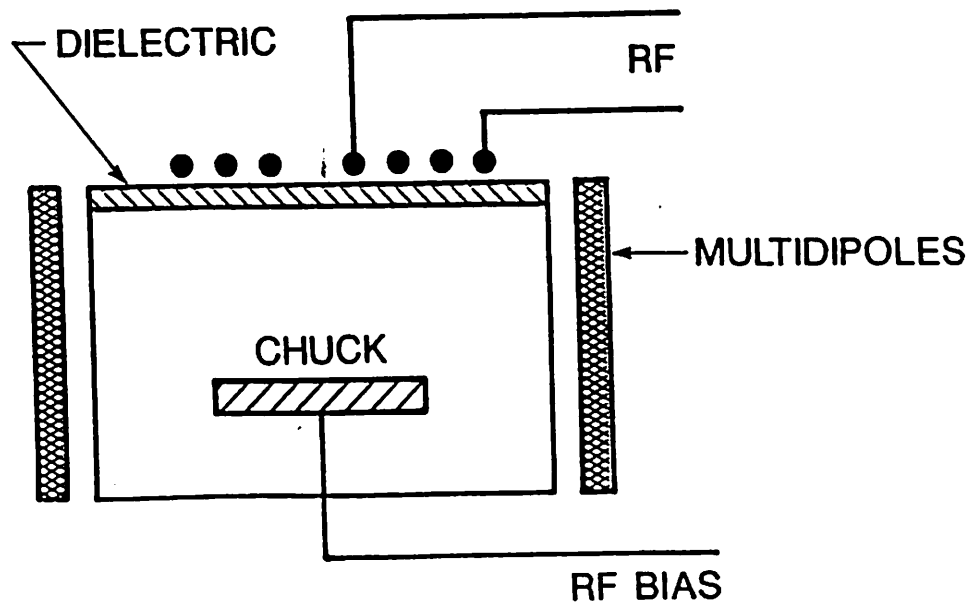


Fig. 24



(a)



(b)

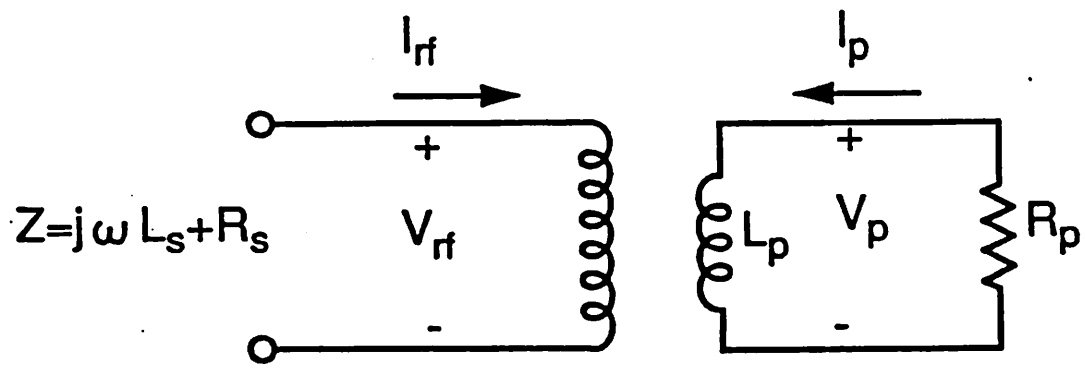


Fig. 26

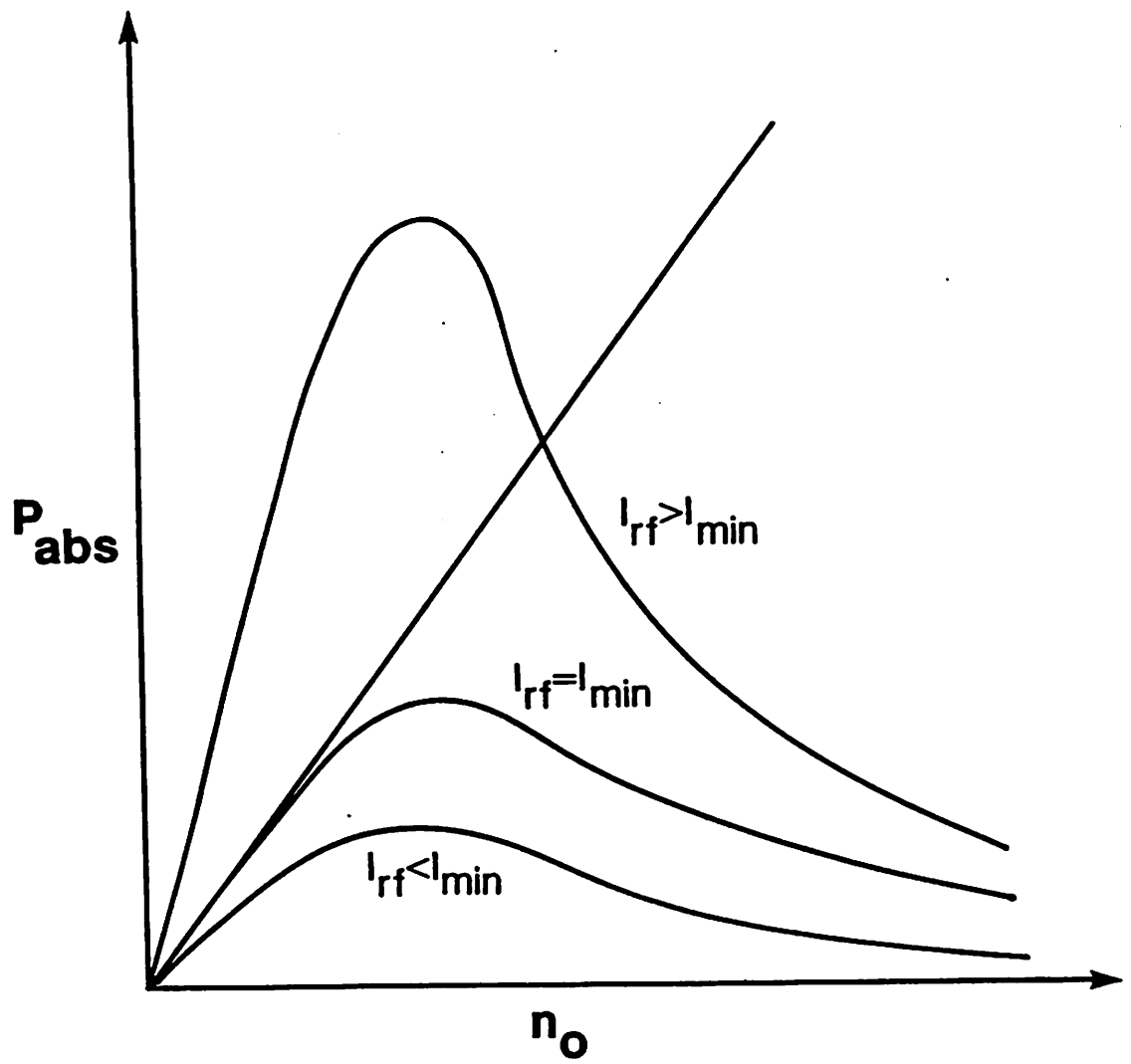


Fig. 27

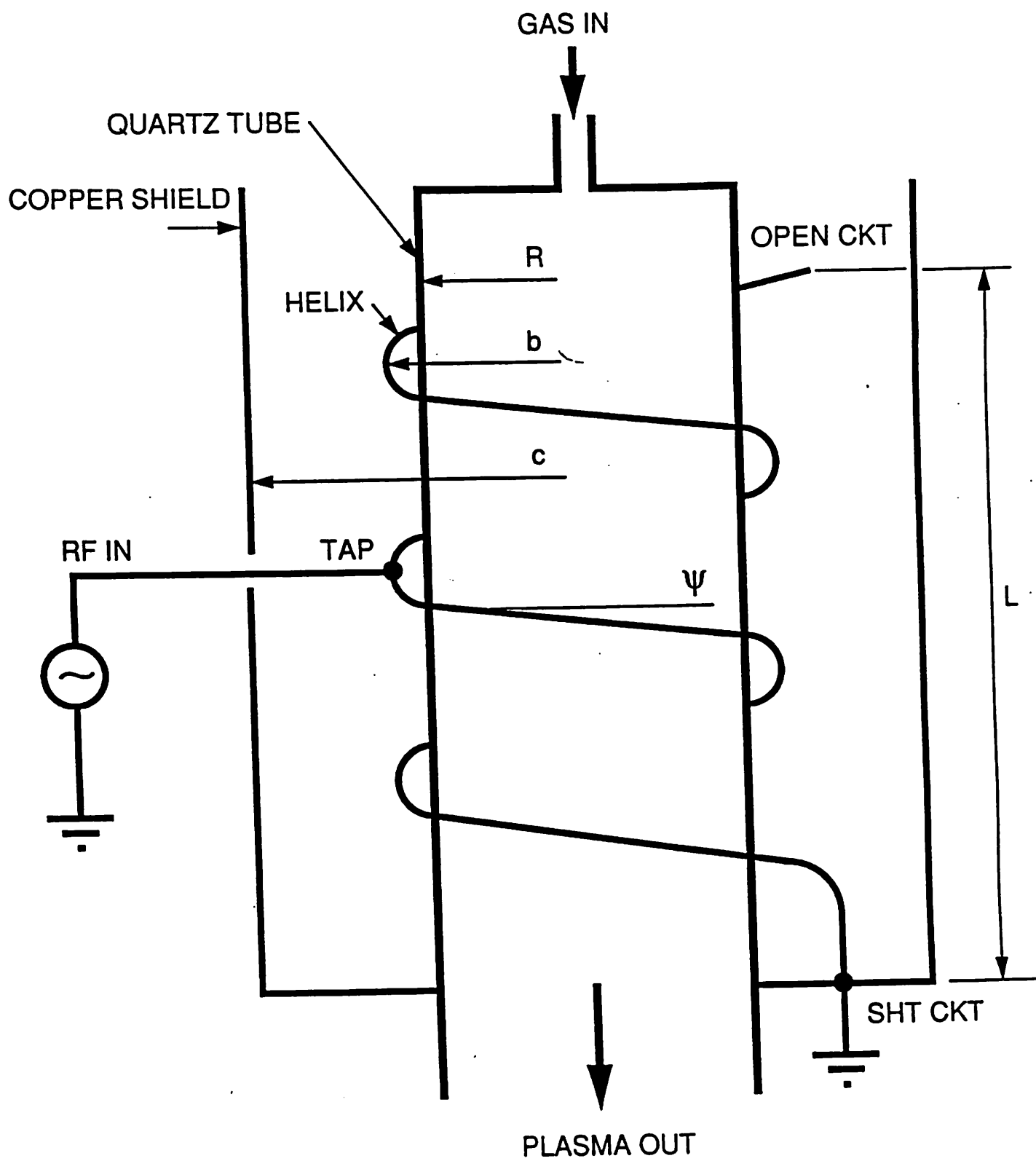


Fig. 28

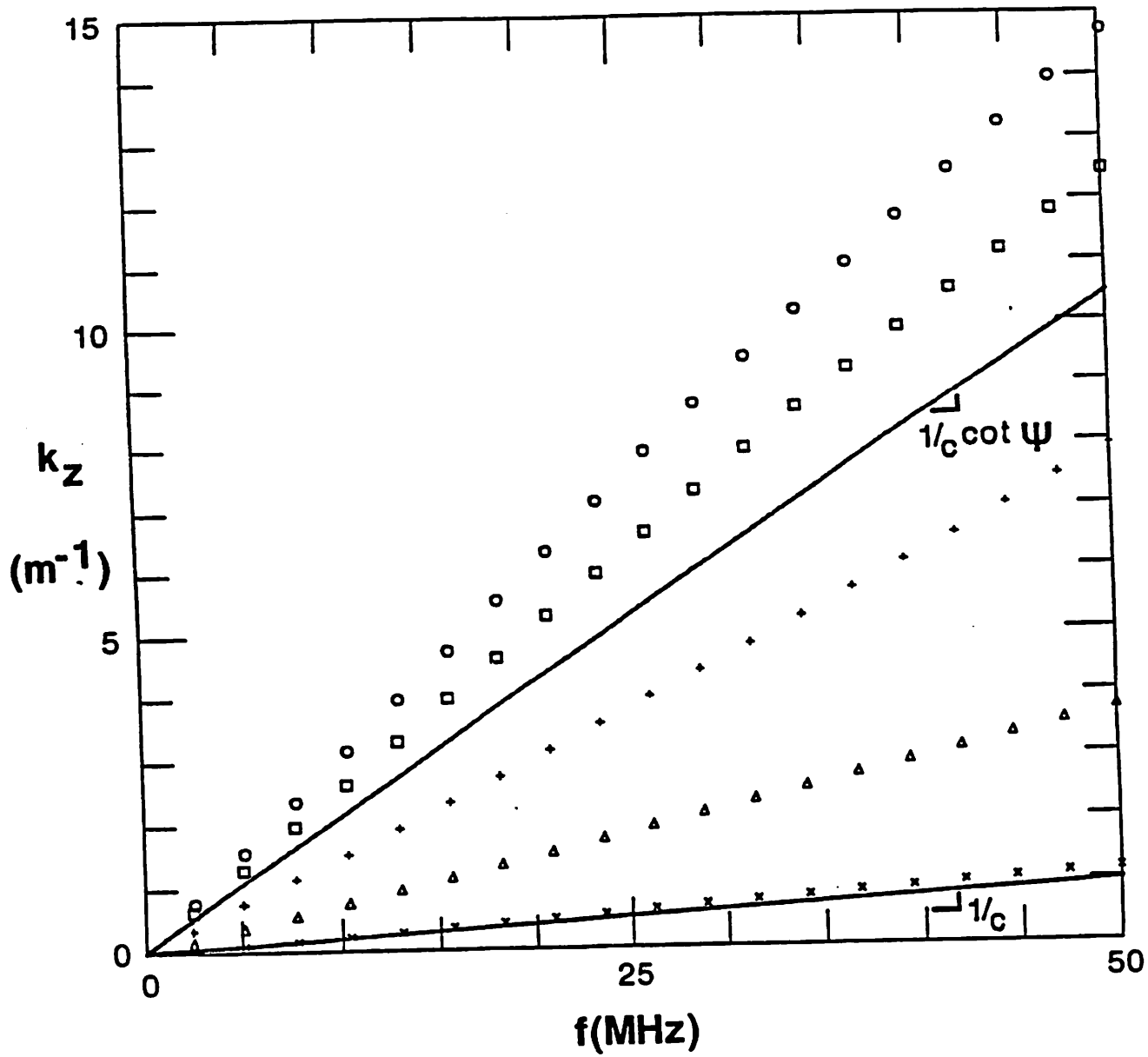


Fig. 29

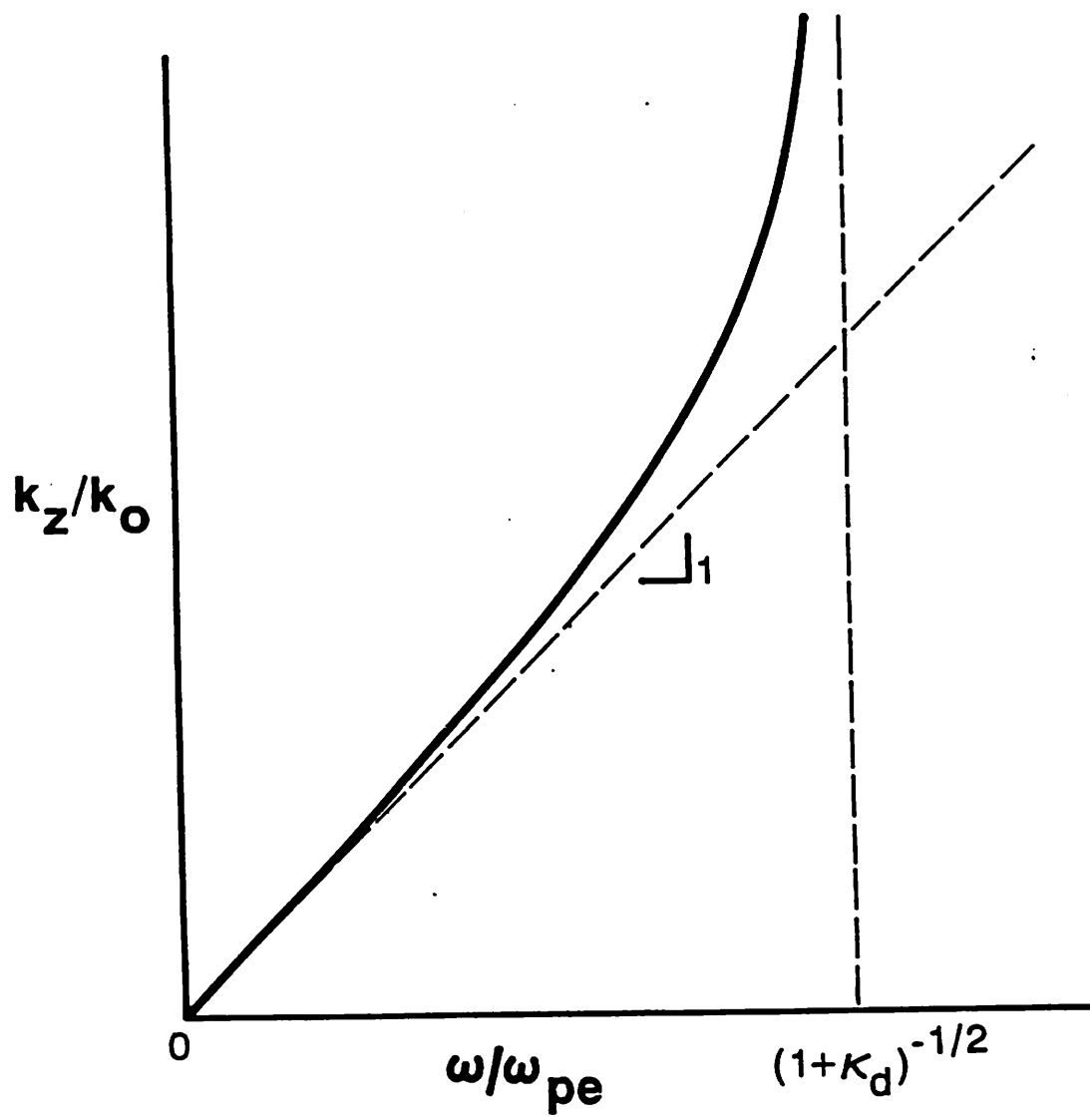


Fig. 30

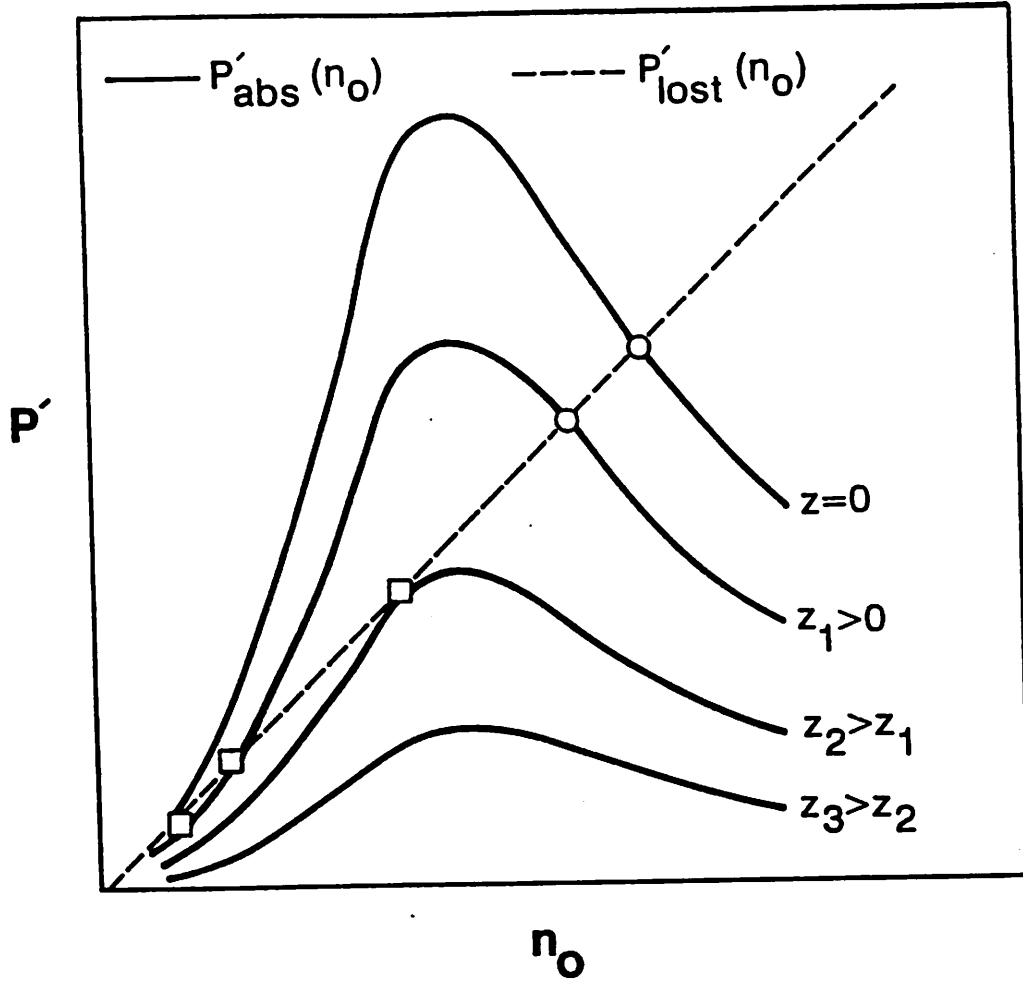


Fig. 31

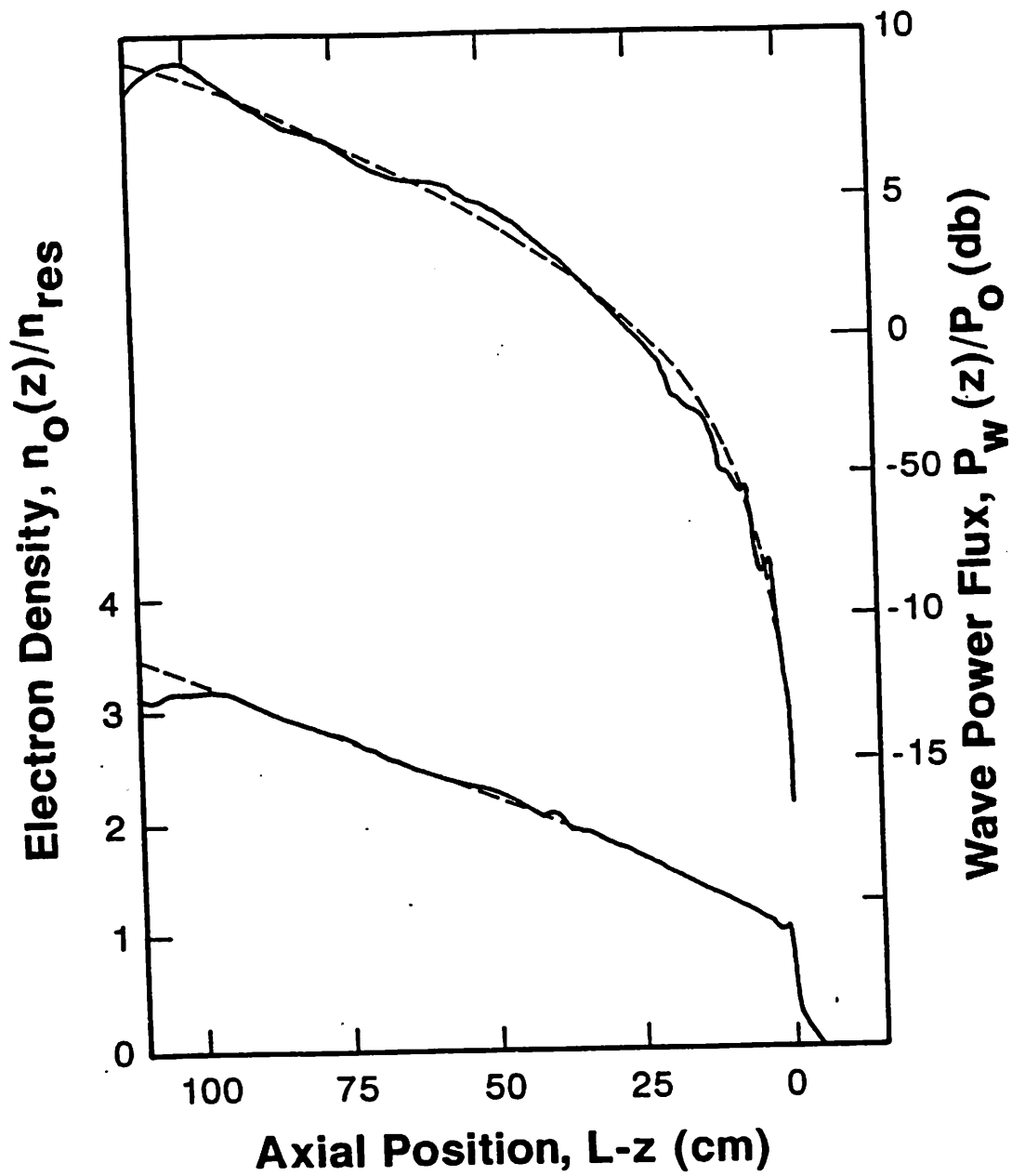


Fig. 32

